



**HAL**  
open science

# Study of Self-Biased Magnetoelectric Materials for Future Micro Energy Sources

Tianwen Huang

► **To cite this version:**

Tianwen Huang. Study of Self-Biased Magnetoelectric Materials for Future Micro Energy Sources. Micro and nanotechnologies/Microelectronics. Sorbonne Université, 2024. English. NNT : 2024SORUS224 . tel-04785710

**HAL Id: tel-04785710**

**<https://theses.hal.science/tel-04785710v1>**

Submitted on 15 Nov 2024

**HAL** is a multi-disciplinary open access archive for the deposit and dissemination of scientific research documents, whether they are published or not. The documents may come from teaching and research institutions in France or abroad, or from public or private research centers.

L'archive ouverte pluridisciplinaire **HAL**, est destinée au dépôt et à la diffusion de documents scientifiques de niveau recherche, publiés ou non, émanant des établissements d'enseignement et de recherche français ou étrangers, des laboratoires publics ou privés.

# Sorbonne Université

Ecole Doctorale Science Mécanique Acoustique Electronique et Robotique

*Laboratoire de Génie Electrique et Electronique de Paris (GeePs)*

## **Study of Self-Biased Magnetoelectric Materials for Future Micro Energy Sources**

Par Tianwen Huang

Thèse de doctorat de Sciences de l'ingénierie

Dirigée par Zhuoxiang Ren et Hakeim Talleb

Présentée et soutenue publiquement le 05/07/2024

Devant un jury composé de:

M. Abdelkader Benabou	Professeur à l'université de Lille	Rapporteur
M. Olivier Hubert	Professeur à l'ENS Paris-Saclay	Rapporteur
M. Stéphane Holé	Professeur à Sorbonne Université	Examinateur
M. Nicolas Galopin	Maître de Conférences à l'Université Grenoble Alpes	Examinateur
Mme. Aurélie Gensbittel	Maître de Conférences à Sorbonne Université	Examinateur
M. Hakeim Talleb	Maître de Conférences, HDR à Sorbonne Université	Directeur de thèse
M Zhuoxiang Ren	Professeur à Sorbonne Université	Directeur de thèse



# Contents

Contents.....	i
Acknowledgement.....	I
Abstract .....	II
Résumé.....	III
General introduction.....	IV
Chapter1. State of art.....	1
1.1 Magnetostriction.....	1
1.1.1 General applications of magnetostriction.....	2
1.2 Piezoelectricity .....	3
1.2.1 General applications of piezoelectricity .....	5
1.3 Magnetoelectric materials .....	6
1.3.1 Recent Applications of Magnetoelectric Materials .....	8
1.3.2 Laminate ME composites.....	8
1.3.3 Working principle of ME transducer .....	9
1.3.4 Studied Regimes for ME response .....	10
1.3.5 Advances in Research on ME Materials and ME Transducers .....	11
1.4 Biomedical implantable applications .....	13
1.4.1 Wireless Power Transfer .....	13
1.4.2 Tissue Engineering .....	15
1.4.3 Brain Stimulation .....	15
1.4.4 Cancer Treatment .....	15
1.4.5 Drug Delivery.....	15
1.5 Self-biased ME materials .....	15
1.5.1 Magnetic Behavior of Magnetostrictive Materials and Self-Biasing in ME Composites.....	16
1.6 Previous contributions and objectives of this thesis work .....	18
1.6.1 Experimental contributions .....	18
1.6.2 FEM modeling contributions .....	21
1.7 Conclusion.....	24
Chapter2. Study of self-biased ME behaviors.....	26
2.1 Fabrication of ME transducers .....	26
2.2 Magnetostrictive Polycrystalline Nickel .....	27
2.3 Piezoelectric monocrystalline LiNbO <sub>3</sub> .....	27
2.3.1 Comparison of the piezoelectric performance .....	30
2.4 Characterization of ME transducers .....	32
2.4.1 Measurement in quasi-static regime.....	33
2.4.2 Measurement in dynamic regime .....	35
2.4.3 Prediction of deliverable electric power.....	36
2.5 Characterization of RF sputtered nickel.....	37
2.5.1 XRD measurement .....	38
2.5.2 Magnetization measurement .....	42
2.6 Initial study for Ni/LiNbO <sub>3</sub> /Ni transducers.....	43
2.7 Full study for 36 Y-cut and 163 Y-cut based ME transducers.....	51
2.8 Magnetostriction measurement for two bilayer ME transducer sample .....	58
2.9 Comparative study of Ni/LiNbO <sub>3</sub> /Ni ME transducers .....	61
2.9.1 Selection of LiNbO <sub>3</sub> cuts.....	61

2.9.2 Comparison of different cuts of LiNbO <sub>3</sub> .....	63
2.9.3 Study with Z-cut LiNbO <sub>3</sub> .....	66
2.9.4 Comparison between Ni/LiNbO <sub>3</sub> /Ni and Ni/PZT-5H/Ni.....	67
2.10 Tests for Optimization of self-biased ME behavior .....	68
2.10.1 Study of transducers on black-LiNbO <sub>3</sub> substrates.....	70
2.10.2 Study of Annealing for Ni/LiNbO <sub>3</sub> /Ni sample.....	72
2.11 Comparaision of ME coefficient of self-biased Ni/LiNbO <sub>3</sub> /Ni samples with others self-biased ME materials .....	73
2.12 Comparaision of maximum deliverable electric power with Terfenol-D/PZT .....	74
2.13 Conclusion.....	75
Chapter3. FE modeling for ME materials .....	77
3.1 Schematic illustrations of ME transducer in FE modeling .....	77
3.2 Governing equations for ME problem .....	78
3.2.1 Constitute laws .....	78
3.2.2 Equilibrium equations .....	81
3.3 FE modelling in 2D .....	82
3.3.1 Equations for ME problem in quasi-static regime .....	82
3.3.2 2D approximations for the field problems .....	83
3.3.3 FE weak formulations .....	85
3.3.4 FEM discretization .....	86
3.3.5 ME problem in quasi-static regime .....	87
3.3.6 Boundary conditions .....	89
3.3.7 Nonlinear problem in quasi-static regime .....	91
3.3.8 ME problem in Harmonic regime .....	94
3.3.9 Prediction of deliverable electric power.....	95
3.3.10 Shell element formulation for thin film structure.....	95
3.4 Simulation of RF sputtered ME transducers .....	98
3.4.1 Properties of nonlinear magnetostrictive coupling.....	98
3.4.2 Properties of linear piezoelectric coupling.....	99
3.5 Simualtion using 2D FEM.....	101
3.6 Conclusion.....	107
Conclusion and perspective.....	108
Annex .....	110
References .....	111

## Acknowledgement

First, I would like to express my deepest gratitude to my family for their unconditional support, both emotionally and financially. It is their encouragement that has given me the freedom to pursue my passion for electrical engineering and successfully complete my undergraduate and master's studies. They have consistently encouraged me to continue with my doctoral research and to delve deeper into my areas of interest.

Next, I would like to sincerely thank my PhD supervisory team: Aurélie, Hakeim, and Zhuoxiang. Their tremendous guidance and support throughout my doctoral journey have been invaluable, not only in terms of academic and research matters but also in their care for my well-being. Their support has helped me remain positive and motivated in the face of research challenges, and to maintain a healthy balance in life. I also want to extend special thanks to my follow-up committee members, Stéphane and Xavier, who have continuously monitored my research progress in annual meetings and provided me with invaluable advice and support. I am also deeply grateful to my colleagues at the INSP laboratory—Massimiliano, Yunlin, David, Loïc, Alireza, and Jean-Eudefor their important guidance and support in the physical property measurements of the materials in my research.

Furthermore, I am immensely grateful to all my colleagues at the GeePs Laboratory at Sorbonne University: Samy, Sheno, Oussama, Rania, Ahmed, Aboubaker, Iheb, Iraklis, Yuanhuan, Josephine, Ambroise, Antoine, Boris, Cheng, Tianyu, Fouzi, Rudy, Alicia, Loris, Cholé, Mohamed, Siqi, Pascal, Yves, Muriel, Massimiliano, Frédérique, Hélène, Nadine, Hamid, Gérard, and Guido, as well as my colleagues at the GeePs Laboratory in Paris-Saclay: Sandrine, Yao, Qihao, Yiyu, Jie, Jianwen, Haiteng, and Chuanyong. If I have inadvertently omitted anyone, I sincerely apologize, but please know that you are also a part of my heartfelt thanks.

Lastly, I would like to give special thanks to my girlfriend, Hongting. We met and fell in love in 2016, and throughout the years, we have supported and encouraged each other. I am truly grateful for her constant support and companionship.

## Abstract

This thesis conducts an in-depth study of self-biased magnetoelectric (ME) composites fabricated by RF sputtering technology: these composites could meet the energy needs of Internet of Things (IoT) applications and be used for biomedical implant applications thanks to wireless energy transfer via a magnetic field. This feature not only reduces the use of batteries, but also reduces the need for implant maintenance. With the widespread deployment of IoT devices, there is a growing demand for efficient, miniaturized energy solutions that require minimal maintenance. Self-biased ME composites enable ME effects to be achieved without the need for a static magnetic field.

The Ni/LiNbO<sub>3</sub>/Ni ME composites were chosen as the main ME material for this research. Complete experimental studies including X-ray diffraction measurements to study the quality of the nickel films, measurements of the magnetization of the nickel to study its magnetic behavior, and electrical measurements to characterize the ME coefficient of the composites were carried out. These measurements, together with finite element simulations, enabled an in-depth study of the self-biased behavior and its origins. It was found that residual stresses generated during the growth of nickel by RF sputtering on the LiNbO<sub>3</sub> substrate were the main causes. In addition, the finite element model developed in this study, which incorporates a shell element formulation and a non-linear magnetoelastic model, successfully simulated the magnetoelectric behavior of these materials. The accuracy and reliability of the simulations were validated by comparison with experimental results.

The Ni/LiNbO<sub>3</sub>/Ni composites are particularly well suited to biomedical implant applications because of their biocompatibility and ability to maintain energy transmission efficiency at minimal sizes, without a static excitation field.

## Résumé

Cette thèse mène une étude approfondie sur les composites magnétoélectriques (ME) auto-polarisés fabriqués par la technologie de pulvérisation RF. Ces composites pourraient répondre aux besoins d'énergie dans les applications de l'Internet des objets (IoT) et être utilisés pour des applications d'implants biomédicaux grâce au transfert d'énergie sans contact via un champ magnétique. Cette caractéristique permet non seulement de réduire l'utilisation de piles et de batteries, mais aussi de diminuer les besoins de maintenance des implants. Avec le déploiement généralisé des appareils IoT, il existe une demande croissante de solutions énergétiques efficaces et miniaturisées qui nécessitent une maintenance minimale. Les composites ME auto-polarisés permettent d'obtenir des effets magnéto-électriques sans avoir besoin d'un champ magnétique statique.

Les composites ME Ni/LiNbO<sub>3</sub>/Ni ont été choisis comme matériau ME principal pour cette recherche. Des études expérimentales complètes incluant des mesures par la diffraction des rayons X pour étudier la qualité des films de nickel, des mesures de la magnétisation du nickel pour étudier son comportement magnétique, et des mesures électriques pour caractériser le coefficient ME des composites ont été menées. Ces mesures ainsi que des simulations par éléments finis ont permis d'étudier en profondeur le comportement d'auto-polarisation et ses origines. Il a été constaté que les contraintes résiduelles générées au cours de la croissance du nickel par pulvérisation RF sur le substrat de LiNbO<sub>3</sub>, en sont les principales causes. En outre, le modèle d'éléments finis développé dans cette étude, qui incorpore une formulation d'éléments en coquille et un modèle magnétoélastique non linéaire, a permis de simuler avec succès le comportement magnétoélectrique de ces matériaux. La précision et la fiabilité des simulations ont été validées par comparaison avec les résultats expérimentaux.

Les composites Ni/LiNbO<sub>3</sub>/Ni sont particulièrement adaptés aux applications d'implants biomédicaux en raison de leur biocompatibilité et de leur capacité à maintenir une efficacité de transmission d'énergie pour des tailles minimales, sans un champ d'excitation statique.

## General introduction

Magnetoelectric (ME) composites are fascinating materials that exhibit a coupling between their magnetic and electric properties, offering a wide range of potential applications, including the biomedical field and the Internet of Things (IoT). The IoT is rapidly expanding, connecting billions of devices to collect and exchange data, which necessitates efficient power solutions for the numerous interconnected sensors and devices. ME composites are especially promising for wireless power transfer applications in implantable medical devices due to their small size, high efficiency, and ability to operate at low frequencies. This allows them to deliver power efficiently and safely through tissue, making them ideal for powering devices like temperature sensors or therapeutic implants.

Self-biased ME materials represent a novel class of these materials, distinct from traditional ME materials. Unlike traditional ME materials that require an external static magnetic field for optimal ME response, self-biased ME materials can exhibit a magnetoelectric response without external biasing, thanks to internal stress or other intrinsic factors. This makes them particularly suitable for applications like wireless power transfer in biomedical implantable devices, as they eliminate the need for permanent magnets or external coils, which are often bulky and impractical in biomedical applications.

In this thesis, our focus is on the study of the impact of the fabrication process of ferromagnetic nickel films on various cuts of lithium niobate ( $\text{LiNbO}_3$ ) and different piezoelectric materials, such as PZT-5H, using RF sputtering. We chose nickel (Ni) as the magnetostrictive material because research on self-biased ME materials often involves Ni, which can be grown on the piezoelectric substrate using the sputtering technique, thus avoiding the use of glue. Moreover, Ni exhibits strong magnetostrictive properties, which makes it suitable for biomedical applications. As for the choice of piezoelectric material, we opted for  $\text{LiNbO}_3$  because of its excellent piezoelectric properties and biocompatibility. This choice makes it a safer alternative to conventional materials like PZT and PMN-PT, which contain lead and could pose health risks if the encapsulation of implant becomes damaged and encounters the human body. While nickel can cause allergic reactions in some individuals, it is relatively safer compared to conventional magnetostrictive materials like Terfenol-D or Galfenol, which contain rare earth elements and could be more harmful to the human body.

The research work in this thesis is mainly based on the previous works of the former PhD students Kévin Malleron on ME behavior characterization, Gang Yang and Tuan Anh Do on the simulation using the 2D and 3D finite element (FE) modeling of the ME problem, and the initial investigation of Ni/ $\text{LiNbO}_3$ /Ni trilayer transducers by post-doctoral researcher Ulises Acevedo-Salas in GeePs laboratory. This thesis is divided into 3 chapters as follows:

Chapter 1 provides an overview of ME materials, including their fundamental concepts, historical background, and applications. The chapter categorizes ME materials into intrinsic and extrinsic types, highlighting the advantages of extrinsic materials, especially for wireless power transmission in biomedical applications. It also introduces the concept of self-biased ME materials and their potential for implantable devices.

Chapter 2 details the experimental investigations on Ni/ $\text{LiNbO}_3$ /Ni samples, including measurements of ME behavior, texture analysis, and magnetic properties. We observed the self-biased ME behavior in these samples, and through our experimental results, we analyzed how this behavior is related to an external stress affecting the nickel material in our samples. The

origin and nature of this external stress have been clarified in this chapter. This chapter also discusses the challenges faced in enhancing the ME response, such as electrodeposition and annealing, and concludes with a comparison between theoretical and experimental results using the FE model.

Chapter 3 focuses on the FE Modeling of laminate ME materials, primarily the nickel films on piezoelectric substrates in a sandwich structure. The chapter discusses the ME L-T (longitudinal – transverse) operation mode and presents the numerical formulation of the coupling problem which links the mechanical and electromagnetic properties. It also introduces a shell element formulation to handle thin-film structures and discusses the prediction of nickel properties from a nonlinear magnetoelastic model.

The manuscript is ended by a short conclusion of this work and the perspective of the future work.

# Chapter 1. State of art

Magnetolectric (ME) composites are an intriguing subclass of multiferroic materials that exhibit a unique coupling between their electric and magnetic phases. The origin of this coupling is the interaction of two intrinsic effects: magnetostriction and piezoelectricity. In this chapter, we will review the state of the art in magnetolectric materials by exploring their historical background, fundamental concepts, and recent advances. We begin by discussing the relative evolution of two key phenomena: magnetostriction and piezoelectricity. Understanding the origins of these phenomena provides a solid foundation for comprehending the complexities of magnetolectric materials.

## 1.1 Magnetostriction

The initial observation of magnetostriction can be attributed to James Joule in 1842 [1], when he discovered that a sample of **ferromagnetic material undergoes dimensional changes in response to an applied magnetic field**. As a result, this **direct magnetostrictive effect** came to be known as the Joule effect. Subsequently, in 1864, Emilio Villari discovered the **converse magnetostrictive effect** [2], which was known as the Villari effect. This effect revealed that **mechanical stress in a material can induce a change in its magnetization**.

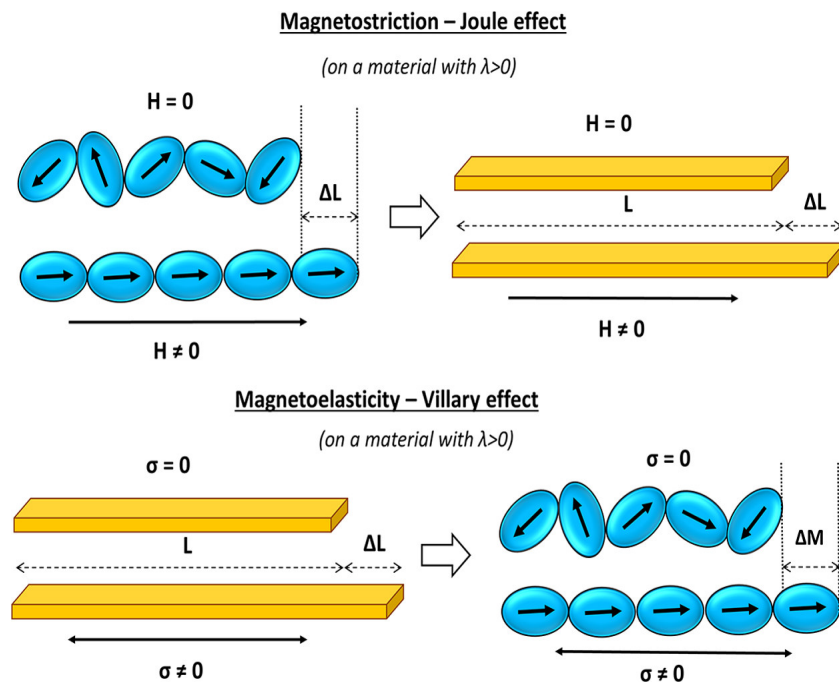


Figure 1.1. Illustration of magnetoelastic coupling effects on a material with a positive magnetostriction ( $\lambda > 0$ ) [3].

As shown in Figure 1.1, the origin of magnetostriction lies in the spin-orbit coupling, the movement of magnetic moments in response to an applied magnetic field induces a reorientation of the crystal lattice, thereby causing a macroscopic alteration in shape or size. In engineering contexts, the primary concern is the linear change in length due to magnetostriction. This magnetostrictive property is commonly characterized by the magnetostrictive strain, denoted as  $\lambda$ . It is a dimensionless quantity defined as the ratio of the change in length ( $\Delta L$ ) to

the original length ( $L$ ) of the material, represented as  $\Delta L/L$ , and this value is typically expressed in the unit of ppm (parts per million). The sign of  $\lambda$  indicates the direction of deformation: positive  $\lambda$  indicates elongation, and negative  $\lambda$  signifies contraction. Moreover, as shown in Figure 1.2,  $\lambda$  increases with an increasing magnetic field until reaching a saturation value  $\lambda_s$ , signifying the maximum potential of the material's magnetostrictive properties under given conditions.

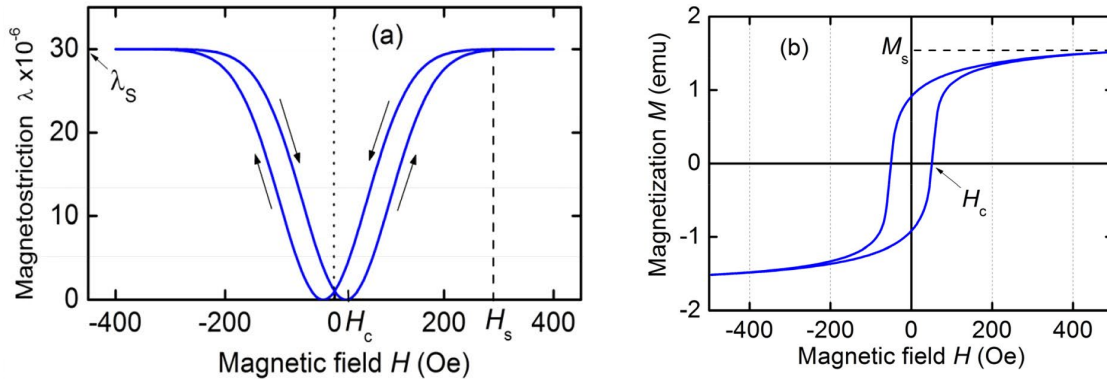


Figure 1.2. Nonlinear behaviors of a ferromagnets (a) positive magnetostriction  $\lambda$  as a function of  $H$  (b) Magnetization  $M$  as a function of  $H$  [4].

Historically foundational in the study of magnetostrictive properties are the traditional ferromagnetic metals, such as nickel and iron. Progressing from elemental metals, we encounter the remarkable Terfenol-D [5], [6], an intermetallic compound predominantly of terbium, iron, and dysprosium. Its exceptionally high magnetostrictive coefficients have found indispensable roles in high precision devices. Further advancements in the field have given rise to Galfenol [7], an alloy melding iron and gallium. This material stands out, combining mechanical durability with significant magnetostrictive properties, offering robust performance where traditional materials might be challenged.

### 1.1.1 General applications of magnetostriction

The unique property of magnetostriction has found applications across a spectrum of technologies:

- **Sensors:** Magnetostrictive materials can be used to detect magnetic fields or stresses. This is particularly useful in precision measurements.

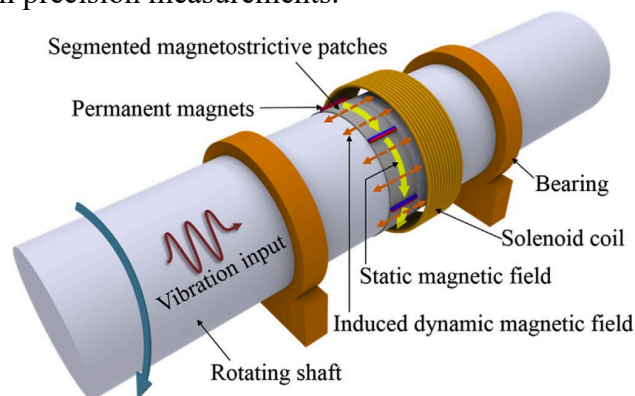


Figure 1.3. A magnetostrictive sensor application [8].

- **Actuators:** These are used in devices where precision movement is controlled by varying magnetic fields.

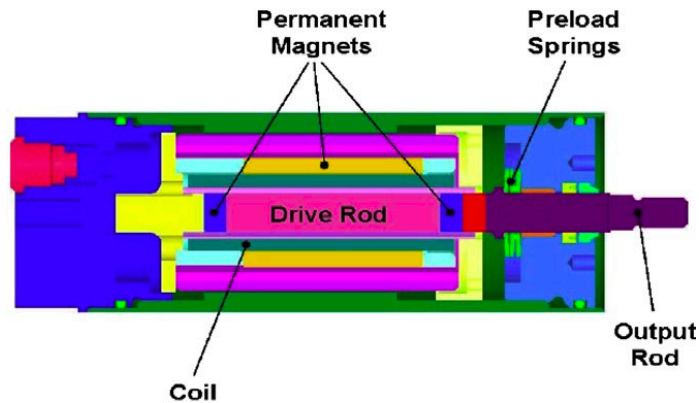


Figure 1.4. A magnetostrictive actuator case [9].

- **Ultrasound Generation:** By rapidly varying the magnetic field in a magnetostrictive material, it's possible to produce sound waves in the ultrasonic range, useful in cleaning and imaging applications.

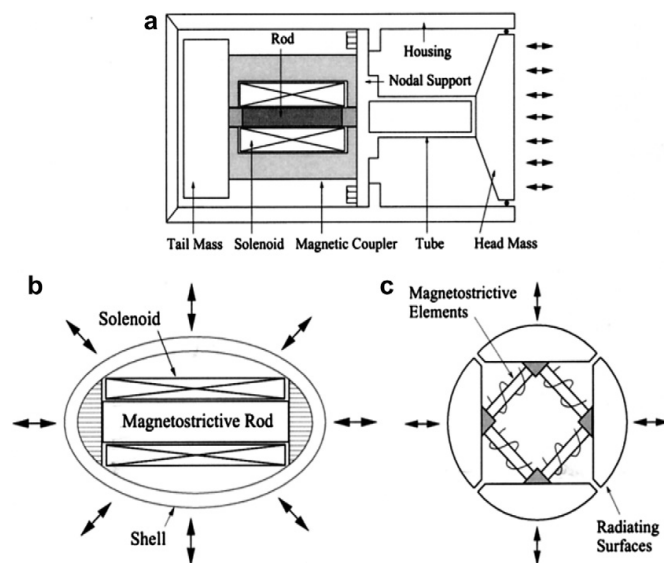


Figure 1.5. A sonar transducer [9].

## 1.2 Piezoelectricity

The phenomenon of piezoelectricity was first discovered by brothers Jacques and Pierre Curie in 1880, through experiments with crystals such as quartz, Rochelle salt, and tourmaline [10]. Later, Gabriel Lippmann predicted the converse piezoelectric effect in 1881 [11]. As shown in Figure 1.6, the **direct piezoelectric effect** is the generation of electricity in response to applied mechanical stress. Conversely, the **converse piezoelectric effect** is the mechanical deformation of a material in response to an applied electric field (electrostriction). As shown in Figure 1.7, the piezoelectric coupling also exhibits nonlinearity. However, as demonstrated in Figure 1.7a, when the strain is near zero, the curve of the electric field as a function of strain can be considered linear.

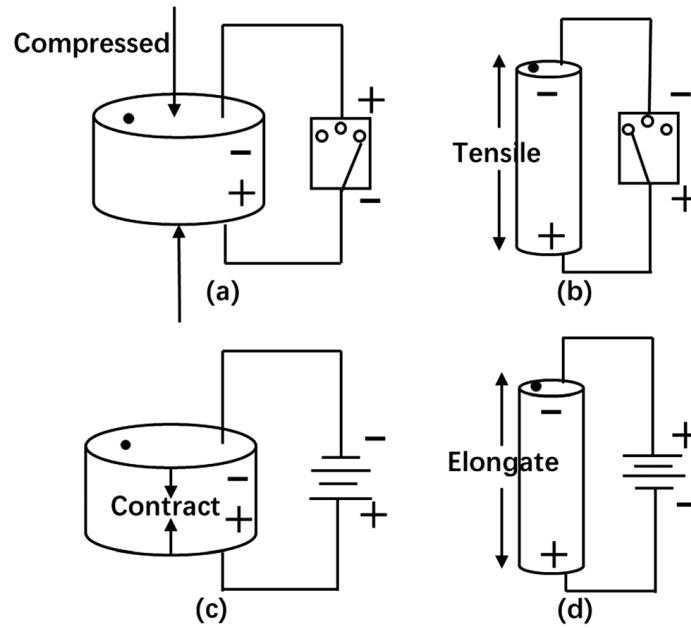


Figure 1.6. Illustration of (a) (b) direct and (c) (d) reverse piezoelectric effects [12].

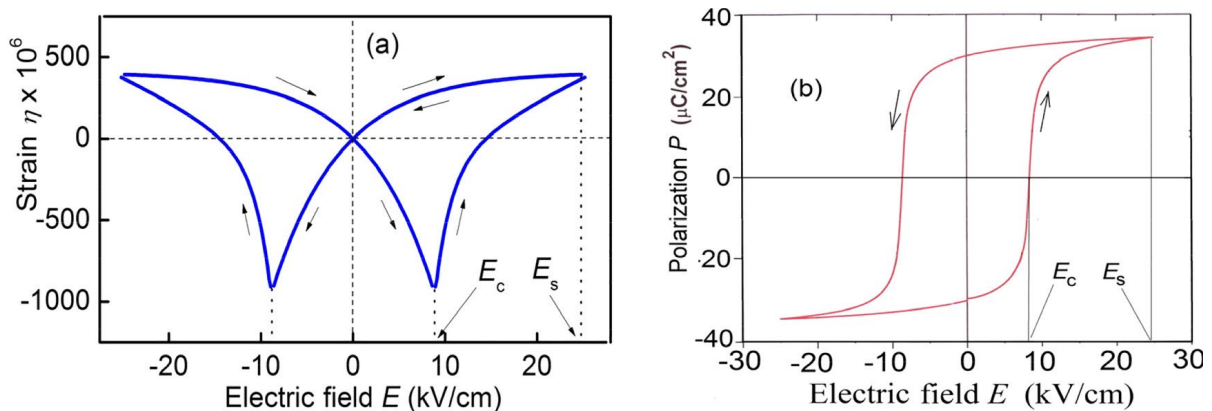


Figure 1.7. Nonlinear behaviors of a piezoelectric (a) Induced Strain as a function of  $E$  (b) polarization  $P$  as a function of  $E$  [4].

Historically foundational in the exploration of piezoelectric properties are traditional crystals like quartz and Rochelle salt. Quartz, due to its inherent stability and pronounced piezoelectric effect, has been a cornerstone in both research and practical applications, such as oscillators and timekeeping devices [13]. Progressing beyond natural crystals, the engineered ceramic materials like Barium Titanate ( $\text{BaTiO}_3$ ) and Lead Zirconate Titanate (PZT) emerge. These synthetic materials, designed for specific applications, are celebrated for their high piezoelectric coefficients and adaptability in modern devices. However, it's essential to note that both PZT and PMN-PT contain lead, a toxic element. The increasing environmental and health concerns about the use of lead have prompted research into lead-free alternatives [12], [14]. Some potential lead-free alternatives being researched include bismuth ferrite ( $\text{BiFeO}_3$ ), and lithium niobate ( $\text{LiNbO}_3$ ). These materials exhibit promising piezoelectric properties in the class lead-free piezoelectric materials.

## 1.2.1 General applications of piezoelectricity

Piezoelectricity has been harnessed in a multitude of technological applications:

- **Sensors:** Piezoelectric materials can detect changes in pressure, making them invaluable in microphones and ultrasound equipment.

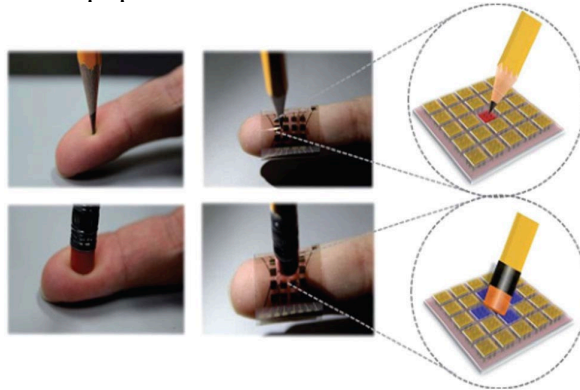


Figure 1.8. A piezoelectric tactile sensor [12].

- **Actuators:** The converse effect is used in precision movement applications, like in some autofocus camera lenses or inkjet printer nozzles.

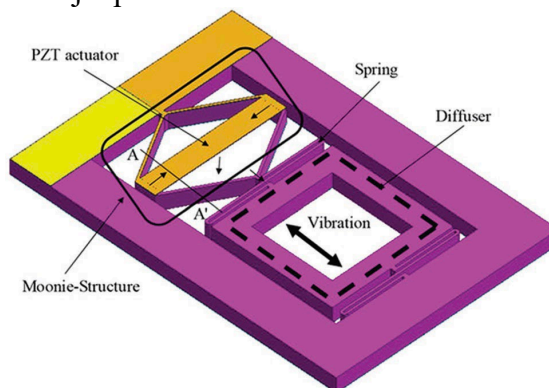


Figure 1.9. A piezoelectric bridge-structured actuator [15].

- **Energy Harvesting:** Capturing and converting ambient mechanical energy (like vibrations) into usable electrical energy.

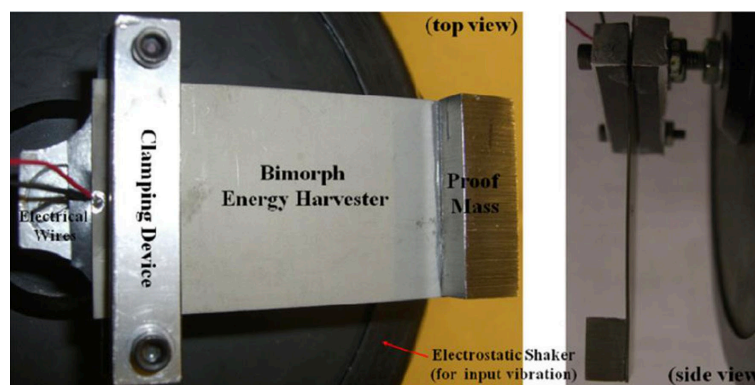


Figure 1.10. A Bimorph piezoelectric energy harvester with proof mass [16].

- **Quartz Clocks:** Utilizing the consistent oscillation of quartz under an electric field to maintain precise timekeeping.

A recent promising advancement in piezoelectric research centers around energy harvesting. Piezoelectric generators, which transform ambient mechanical energy into electrical power, are under exploration for their potential to power small electronic devices within the Internet of Things (IoT) framework [17], [18]. This innovation has the potential to transform power generation and storage in small-scale, distributed systems, possibly obviating the need for conventional batteries in certain applications. Wearable technology also stands to benefit greatly from advances in piezoelectric materials. Devices that can harness the mechanical energy of human motion to generate power can offer new capabilities in health monitoring, communication, and user interface technology [19]. Biocompatible piezoelectric materials are being researched for medical applications, from sensors that monitor physiological signals to drug delivery systems, to power sources for implanted devices.

### 1.3 Magnetolectric materials

Magnetolectric (ME) materials are renowned for their unique magnetolectric coupling effect, which enables **control of electric polarization through a magnetic field (direct ME effect)** and **manipulation of magnetization via an electric field (reverse ME effect)**, as illustrated in Figure 1.11.

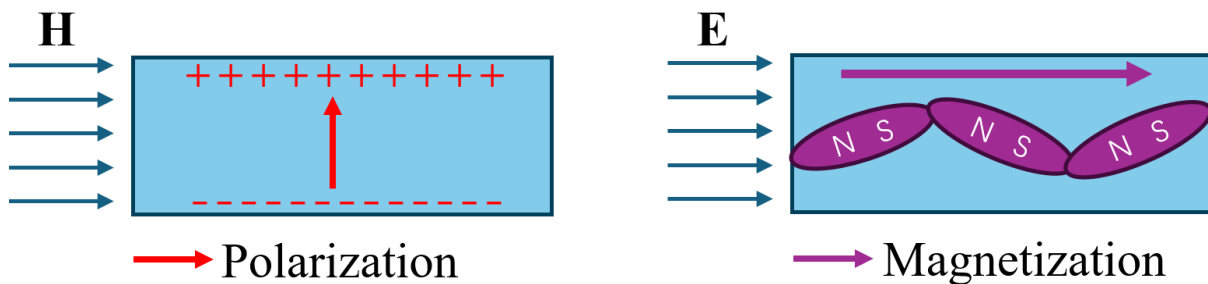


Figure 1.11. (a) Direct ME effect and (b) Inverse ME effect.

The study of ME materials and their effects can be traced back to 1894 when Curie predicted their existence. It wasn't until 1958 that Landau and Lifshitz theoretically demonstrated the feasibility of the ME effect, based on the crystal symmetry of the single-phase multiferroic material  $\text{Cr}_2\text{O}_3$  [20]. This theory was experimentally confirmed by Dzyaloshinskii in 1960 with a  $\text{Cr}_2\text{O}_3$  sample, initiating comprehensive studies on the coexistence of ferroelectric and magnetic orders in single-phase materials [21].

Despite their combined ferroelectric and magnetic properties, nearly all single-phase ME materials like  $\text{Cr}_2\text{O}_3$ ,  $\text{BiFeO}_3$ , and  $\text{BiMnO}_3$  face challenges in practical applications due to their low Curie temperatures and weak ME coupling coefficients at room temperature. To address these challenges, researchers have shifted their focus to two-phase ME composites, which combine ferroelectric and magnetostrictive phases through strain, as illustrated in Figure 1.12. This concept was first introduced by Van Suchtelen in 1972 [22], this innovative concept not only overcomes the limitations associated with single-phase materials but also provides enhanced design flexibility and broader operating temperature ranges. These advantages make ME composites highly promising for practical ME technology deployment. Recent

advancements have seen significant progress in devices based on magnetolectric composite thin films, such as highly sensitive magnetic field sensors and ME antennas [23], [24], [25].

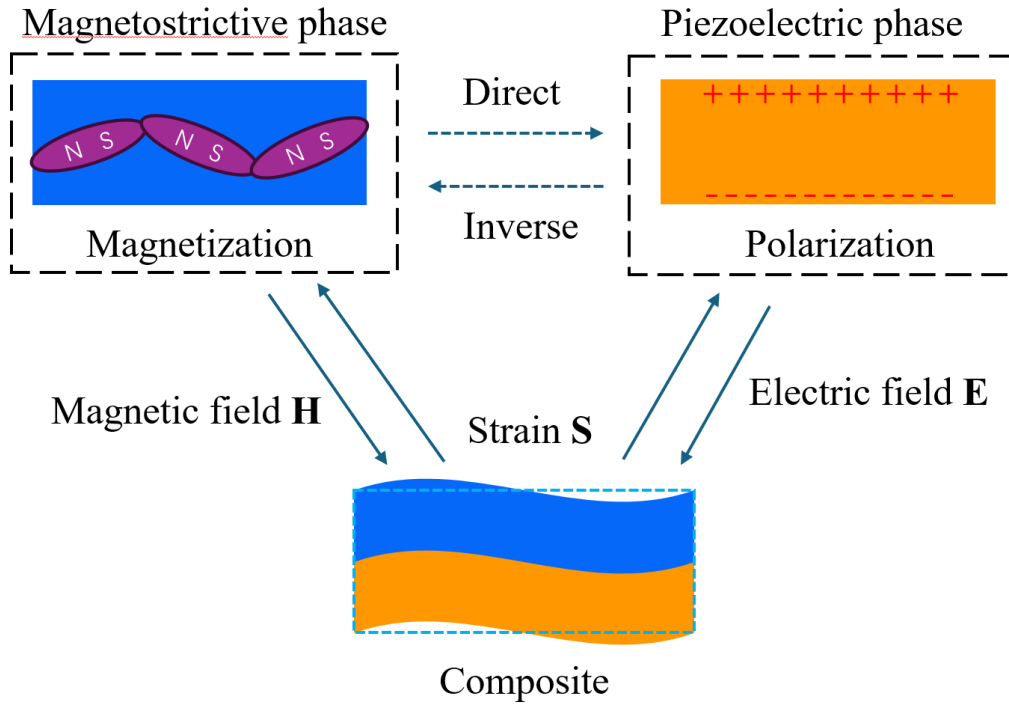


Figure 1.12. Inverse and direct ME effects in ME composite materials.

A critical method of exploration involves creating magnetolectric composites by combining different materials. This approach aims to enhance the magnetolectric response by carefully selecting and arranging constituent materials in various dimensional combinations as depicted in Figure 1.13. and based on the properties of both materials, the fabrication process, the interfacial coupling, and the phase connectivity.

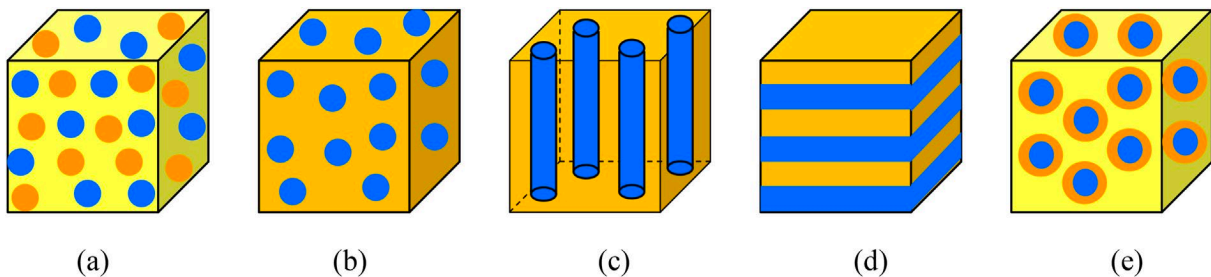


Figure 1.13. Different types of ME composite materials with the first and second number denote the dimension of magnetostrictive and piezoelectric materials, respectively (yellow - dielectric material; orange -piezoelectric phase; blue – magnetostrictive phase.): (a) 0–0; (b) 0–3; (c) 1–3; (d) 2–2; (e) core-shell nanocomposite [26].

The composites most studied in the literature are laminate composites (see Figure 1.13d). This is the type of composite used in our study with a piezoelectric substrate and magnetostrictive materials bonded or deposited in thin layers on one or both sides.

### 1.3.1 Recent Applications of Magnetoelectric Materials

Some notable applications using ME materials include [27], [28], [29], [30], [31]:

- **Magnetic Field Sensors:** ME materials offer the possibility of highly sensitive and compact magnetic field sensors. By exploiting the magnetoelectric coupling, these sensors can detect and measure magnetic fields with high precision. Potential applications include non-destructive testing, biomedical imaging, and magnetic navigation systems.
- **Spintronics:** Spintronics, which involves the manipulation of electron spins for information storage and processing, is an emerging field that can benefit from magnetoelectric materials. Multiferroic materials can provide a pathway for efficient coupling between magnetic and electric properties, enabling the development of novel spintronic devices with lower power consumption and enhanced functionality.
- **Energy Harvesting and Conversion:** ME materials offer possibilities for energy harvesting and conversion. By utilizing the strain induced by a magnetic field, these materials can convert mechanical energy into electrical energy, opening opportunities for self-powered sensors, wearable devices, and energy-efficient systems [32], [33], [34].
- **Memory Devices:** The coupling between magnetic and electric properties in multiferroic materials can be harnessed for advanced memory devices. Magnetoelectric memories have the potential to combine the benefits of both magnetic and ferroelectric memories, offering high-density storage, low power consumption, and non-volatility.

### 1.3.2 Laminate ME composites

As depicted in Figure 1.14, trilayer laminate ME composites operate in four distinct modes: longitudinally magnetized and longitudinally poled (L-L), transversely magnetized and transversely poled (T-T), transversely magnetized and longitudinally poled (T-L), and longitudinally magnetized and transversely poled (L-T). Among these, the L-T mode stands out for its advantageous blend of high ME coupling efficiency and ease of manufacturing. This makes the L-T configuration a preferred choice for in-depth study and practical application [35]. Therefore, in this thesis work, our primary study focuses on investigating the ME behaviors of trilayer ME composites in the ME L-T mode.

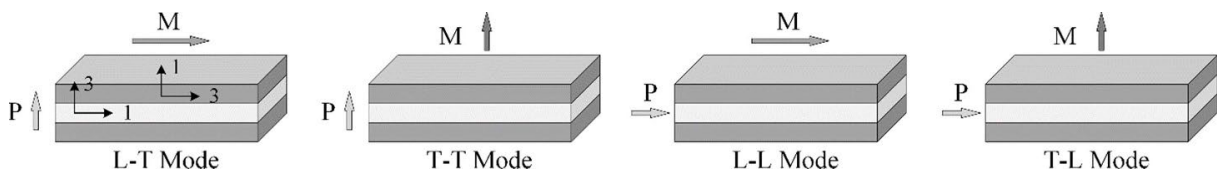


Figure 1.14. Four operating modes of trilayer ME composites

### 1.3.3 Working principle of ME transducer

A diagram of a laminate magnetolectric composite is shown in Figure 1.15. The piezoelectric substrate is shown in yellow and labelled P. The magnetostrictive material, bonded or deposited on both sides of the piezoelectric, is shown in blue and labelled M. The piezoelectric is polarized in the direction of thickness. In the magnetostrictive material, the magnetization is in the plane of the faces. (L-T operated mode as shown in Figure 1.14).

The working conditions of ME transducer according to its direct magnetolectric effect, as illustrated in Figure 1.15, involves applying an external magnetic excitation composed of both a static (DC) magnetic field  $H_{dc}$  and a small dynamic (AC) magnetic harmonic field  $\delta H_{ac}$  to the material. The magnetostrictive material deforms under the influence of the magnetic field, and the resulting stresses applied to the piezoelectric material induce polarization. This results in the generation of an alternating voltage  $\delta V$  across the piezoelectric layer through electrodes. The electrical energy can then be used to power a load ( $Z$  in Figure 1.15) representing the input impedance of an electrical device that we aim to power.

The ME composite operates in resonant mode, and its resonant frequency is of the form [36]:

$$f_r = \frac{1}{2l} \sqrt{\frac{1}{\bar{\rho} s_{11}}} \quad 1.1$$

where  $l$  is the length of the ME composite,  $\bar{\rho}$  is the average density, and  $\overline{s_{11}}$  is the equivalent elastic compliance in length direction in global coordinate of ME material. These coefficients will be detailed in chapter 3.

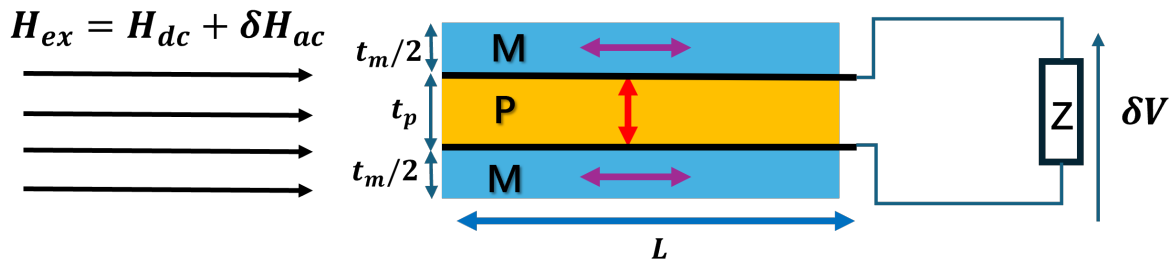


Figure 1.15. Working conditions of direct magnetolectric effect in ME energy transducer.

The working principle of the ME transducer is shown in Figure 1.16. To maximize the ME effect, it is crucial to set an optimal bias using the DC magnetic field  $H_{dc}$ . This bias point is typically selected in the region where the magnetostrictive response curve shows the highest sensitivity to changes in the applied magnetic field, and we denote as  $H_{dc,opt}$ . It is worth noting that, at this optimal bias point, we can assume that both the magnetostrictive and piezoelectric effects behave linearly, allowing for a more straightforward analysis of the magnetolectric coupling. The purpose of this biasing is to ensure that the small dynamic field  $\delta H_{ac}$ , can induce significant mechanical strain in the magnetostrictive layer, which is then efficiently transferred to the piezoelectric layer, resulting in an electrical output  $\delta V$ . By maintaining the system at this optimal  $H_{dc,opt}$ , the linear response of both material layers ensures that the ME transducer operates at its maximum efficiency.

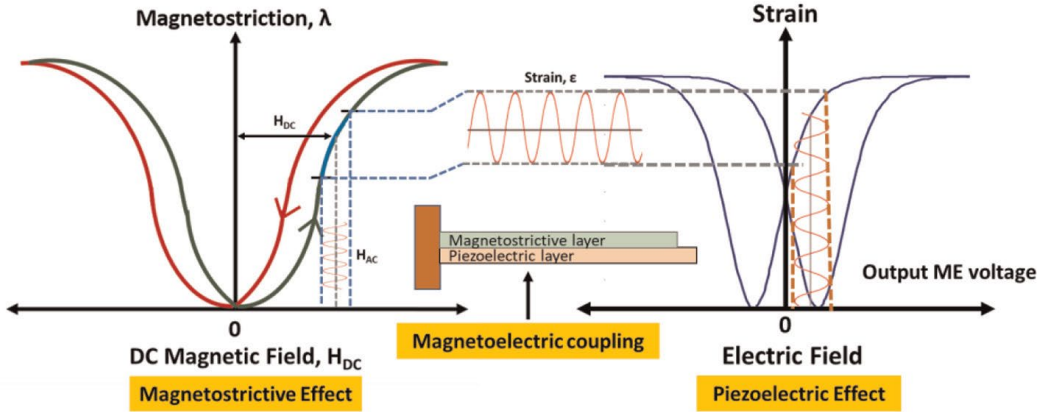


Figure 1.16. Working principle of direct magnetolectric effect in ME energy transducer [37].

As shown in Figure 1.15, the efficiency of the direct ME coupling effect in laminate ME materials is typically compared using the direct magnetolectric coefficient  $\alpha_E$ , defined as:

$$\alpha_{ME} = \alpha_E = \frac{\delta E}{\delta H_{ac}} = \frac{\delta V}{t_p \cdot \delta H_{ac}} \quad 1.2$$

Where  $t_p$  is the thickness of the piezoelectric layer.

The coefficient  $\alpha_E$  quantifies the strength of the ME coupling, with its conventional unit being V/cm·Oe. A higher value of  $\alpha_E$  indicates more efficient conversion of magnetic energy into electrical energy, which is crucial for practical applications such as sensors and energy transducers.

When ME materials are used as energy transducers, the electric power they can deliver is another critical parameter for evaluating energy conversion and the amount of energy that can be supplied to a load. The optimal deliverable electric power from the ME transducer is obtained when the internal resistance of the transducer matches the load resistance. This optimal power can be expressed as follows:

$$P_{opt} = \frac{(V_{oc} / 2\sqrt{2})^2}{Z_{internal}} \quad 1.3$$

Where  $V_{oc}$  is the magnitude of the output voltage from the ME transducer under open-circuit condition, and  $Z_{internal}$  is the internal impedance.

### 1.3.4 Studied Regimes for ME response

The study of the magnetolectric response in ME materials can be divided into two distinct regimes based on the characteristics of the applied magnetic field: quasi-static and dynamic.

#### 1.3.4.a. Quasi-Static Regime

In the quasi-static regime, the focus is on how the static magnetic field  $H_{dc}$  affects the ME coupling, while the dynamic magnetic field  $\delta H_{ac}$  remains fixed in strength. This regime is

crucial for understanding how the biasing affects the overall ME response of the material. By adjusting  $H_{dc}$ , one can identify the optimal bias point where the material's ME response is maximized.

### 1.3.4.b. Dynamic Regime

In contrast, the dynamic regime explores the response of the ME material when the amplitude or frequency of the dynamic magnetic field  $\delta H_{ac}$  varies. In this regime, the frequency of  $\delta H_{ac}$  plays a pivotal role in determining the material's response, especially near its resonance frequency. The ME effect is significantly enhanced at the resonance frequency, where mechanical oscillations within the material synchronize with the applied magnetic field, leading to maximum energy transfer.

In the dynamic regime, the system often operates at the first longitudinal resonance frequency  $f_{r1,L}$  for 2-2 layered structures to achieve optimal magnetoelectric coupling. At this resonance frequency, the mechanical strain in the magnetostrictive layer reaches its peak, which is then efficiently transferred to the piezoelectric layer, resulting in a higher electrical output  $\delta V$ . As shown in Figure 1.17, an equivalent circuit model with inductance  $L_m$ , capacitance  $C_m$ , and  $R_m$  elements representing the resonance behavior of the ME material. At resonance, the circuit impedance is minimized, optimizing the material's electrical response in the dynamic regime.

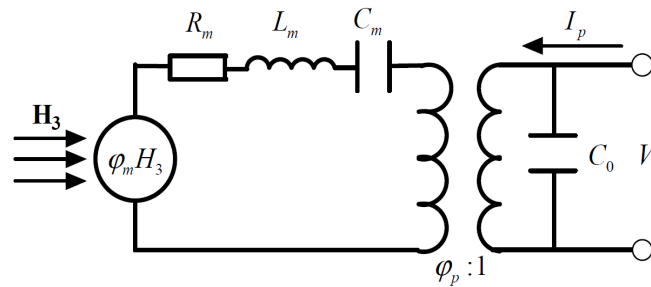


Figure 1.17. Equivalent electric circuit of ME material in dynamic regime [38].

### 1.3.5 Advances in Research on ME Materials and ME Transducers

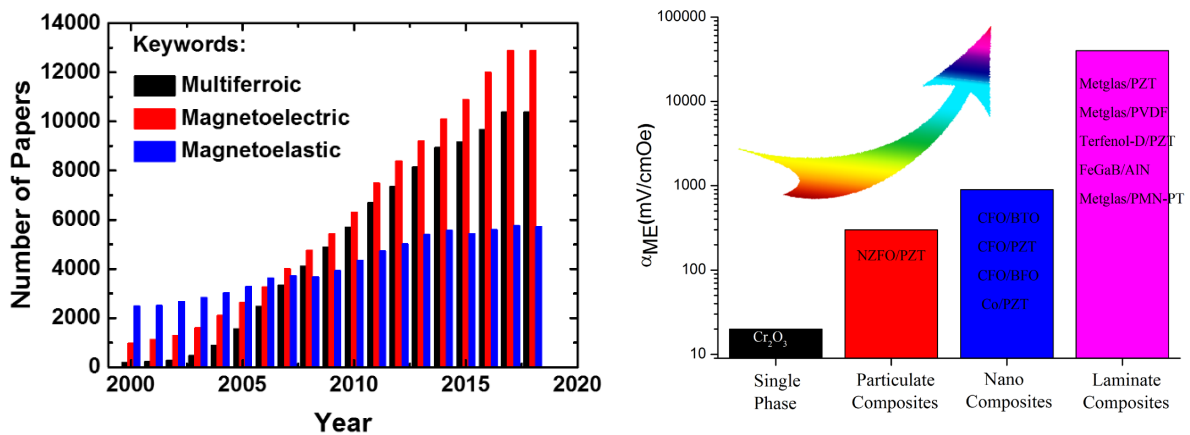
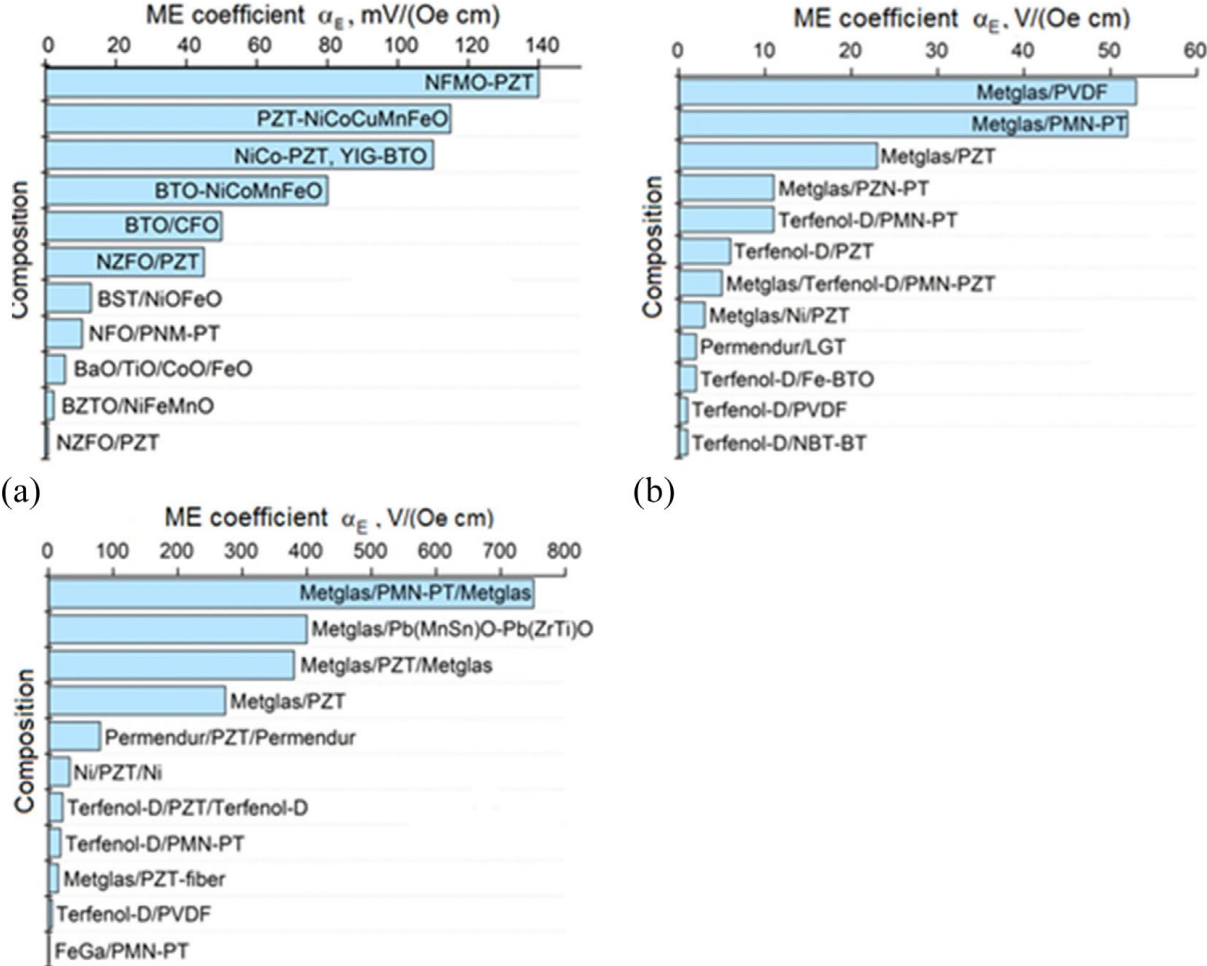


Figure 1.18. (a) Development trend of research on the magnetoelastic [25]. (b) Evolution of ME performance through different structures and composite combinations in recent research [39].

As illustrated in Figure 1.18a, there has been a growing interest among researchers in the ME phenomenon, primarily due to the coupling effects between the magnetic and electric phases, which make these materials versatile and promising for a broad range of device-level applications. ME materials display varying performance based on their structural configuration, which directly influences the efficiency of their coupling between magnetic and electric fields. As shown in Figure 1.18b, among the different geometries, laminate composites exhibit the highest ME coupling coefficients, often outperforming other structures such as particulate composites and core-shell nanoparticles. Additionally, as shown in Figure 1.19, in particulate composites, where magnetostrictive and piezoelectric phases are randomly distributed in a matrix, the coupling is less efficient, resulting in lower ME coefficients typically around 1–100 mV/(Oe cm). Core-shell structures improve mechanical coupling by enclosing the magnetostrictive core within a piezoelectric shell, enhancing strain transfer but still facing challenges in scalability. However, laminate composites, with their alternating layers of magnetostrictive and piezoelectric materials, such as Terfenol-D/PZT or Metglas/PZT, achieve superior coupling efficiency, with ME coefficients reaching hundreds of V/(Oe cm) under resonant conditions. This makes laminate composites particularly well-suited for high-performance applications in sensors, energy harvesters, and actuators.



(a) (b) (c) Figure 1.19. Comparison of ME coefficient in recent studies of ME materials: (a) particular ME materials, (b) laminate ME materials at conventional frequency 1kHz, (c) laminate ME materials under resonant condition [26].

## 1.4 Biomedical implantable applications

### 1.4.1 Wireless Power Transfer

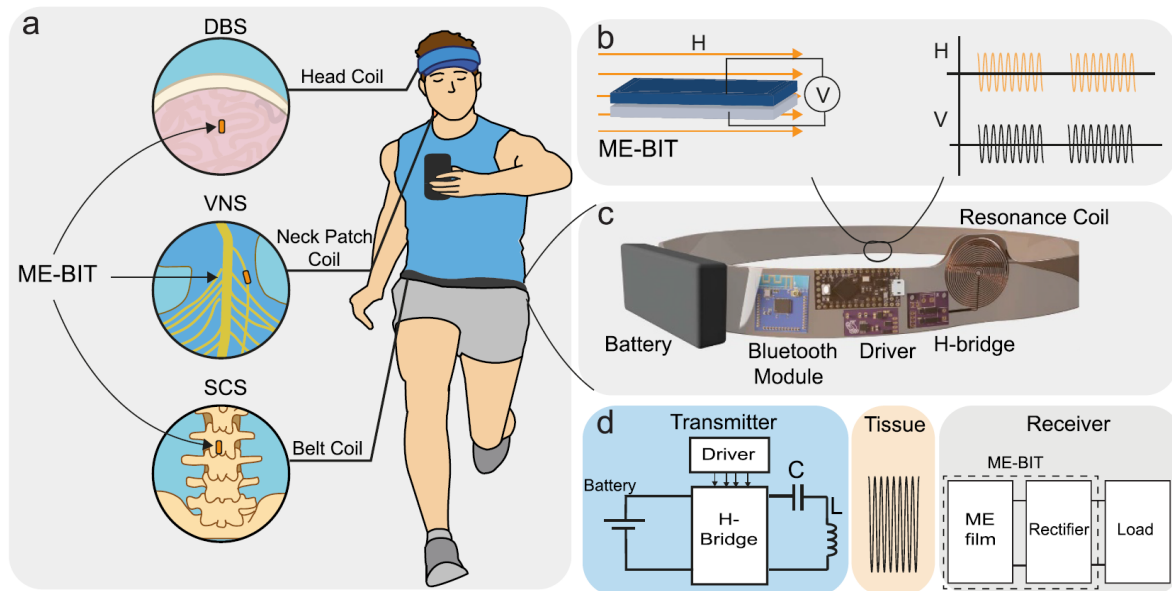


Figure 1.20. An illustration of the working principle of wireless energy transmission application for implantable devices [40].

### Unique Advantages of Magnetolectric Materials in biomedical applications

- **Efficient Transfer and Safety:** ME materials can achieve efficient power transfer under low-frequency (a few Hz to several hundred kHz) and low-intensity magnetic fields ( $< 1$  mT) [26], [32], [33], [39], making them highly suitable for implantable devices. Traditional WPT methods like RF transmission often suffer from signal attenuation in air and biological tissues, leading to lower transfer efficiency [40]. ME technology addresses this issue effectively, especially within short distances ranging from millimeters to centimeters.
- **Tolerance to Misalignment:** Compared to inductive power transfer (IPT), ME materials are more tolerant of misalignment between the transmitter and receiver. IPT typically requires precise alignment of coils to maintain efficient energy transfer, while ME materials can still achieve stable power transmission even under translational misalignment. This characteristic makes ME materials particularly suitable for dynamic environments, such as implantable medical devices, which may experience internal body movement or external transmitter shifts.
- **Low Impact on Biological Tissues:** ME materials operate under low-intensity magnetic fields, minimizing absorption and reflection in biological tissues and reducing potential biological safety risks [40], [41]. In contrast, RF and ultrasound-based methods can cause tissue heating or other side effects due to high-frequency signals. ME technology maintains efficient power transfer at low frequencies, ensuring the safety of biomedical implants over extended use.
- **Multifunctionality:** ME materials not only facilitate wireless power transfer but also offer additional functionalities, such as controlling stimulation waveforms. For example, E.wood

et al. showed that using the magnetoelectric effect can enable both power transmission and neural stimulation control, laying the foundation for next-generation smart implantable devices [41].

Table 1.1. Comparison with Other Wireless Power Transfer Technologies

Technology	Advantages	Disadvantages	Applications
Magnetoelectric	Efficient at low-frequency, low-intensity fields; Low impact on tissues; Tolerant to misalignment	Efficiency still improving; Complex fabrication process	Implantable medical devices, small IoT devices
Inductive power transfer	High efficiency for high-power transfer; Mature technology	Short transmission range; Sensitive to coil alignment	Electric vehicle charging, consumer electronics
Capacitive power transfer	Electric fields penetrate non-metal materials; Low cost	Low transmission efficiency; Highly affected by environment; Limited range	Low-power, short-distance applications
RF Transmission	Long transmission range; Can transmit data simultaneously	Low efficiency; Potential radiation impact on humans and environment	Long-distance, low-power sensor networks
Acoustic power transfer	High efficiency in soft tissues; Good biocompatibility	Sensitive to impedance mismatches; Limited to soft tissue applications	Medical implants, liquid environment applications

In summary, the use of magnetoelectric materials in wireless power transfer offers several key advantages, including high efficiency under low-frequency, low-intensity magnetic fields, minimal impact on biological tissues, and tolerance to device misalignment. These benefits make ME materials ideal for applications in implantable medical devices and small IoT devices. Additionally, the multifunctionality of ME materials opens up new possibilities for the development of next-generation smart implants. Compared to other wireless power transfer technologies, ME materials overcome many traditional limitations, pointing to a significant direction for future advancements in WPT.

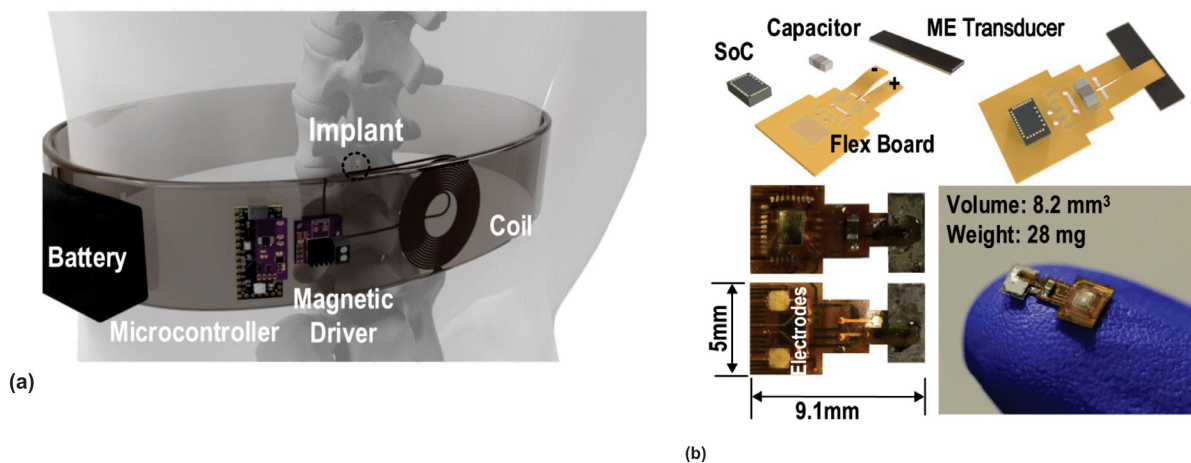


Figure 1.21. An illustration of the wireless energy transmission application for implantable devices [42].

### **1.4.2 Tissue Engineering**

ME materials can generate precise electric fields under the control of an external magnetic field. These electric fields can promote cell proliferation and differentiation, thus accelerating tissue repair and regeneration. For instance, in bone regeneration, the electric field generated by activating ME materials with a magnetic field can stimulate osteoblast activity, promoting bone tissue formation [26].

### **1.4.3 Brain Stimulation**

ME materials can achieve non-invasive stimulation of specific brain regions, used for treating neurodegenerative diseases such as Parkinson's disease. By activating ME nanoparticles with an external magnetic field to generate localized electrical stimulation, neuronal activity can be precisely modulated to restore normal functions [26].

### **1.4.4 Cancer Treatment**

Magnetoelectric materials can precisely target and release anticancer drugs to tumor cells under the control of an external magnetic field, minimizing damage to surrounding healthy tissues. This method can enhance the therapeutic efficacy of the drugs and reduce side effects [26].

### **1.4.5 Drug Delivery**

Magnetoelectric composites can act as smart drug delivery systems, regulating drug release through an external magnetic field. This system allows for continuous or pulsed precise control of drug release rates, achieving targeted therapy at specific times and locations [26].

## **1.5 Self-biased ME materials**

As shown in Figure 1.22, the primary distinction between self-biased ME materials and traditional ME materials lies in their ability to spontaneously exhibit the magnetoelectric effect without requiring an external DC magnetic field. This intrinsic property significantly enhances the usability and flexibility of ME materials, especially for applications where device miniaturization and operational stability are crucial. By eliminating the need for external magnetic bias, self-biased ME materials simplify device design, reduce overall size, and enhance energy efficiency, making them highly suitable for implantable biomedical devices and other emerging technologies.

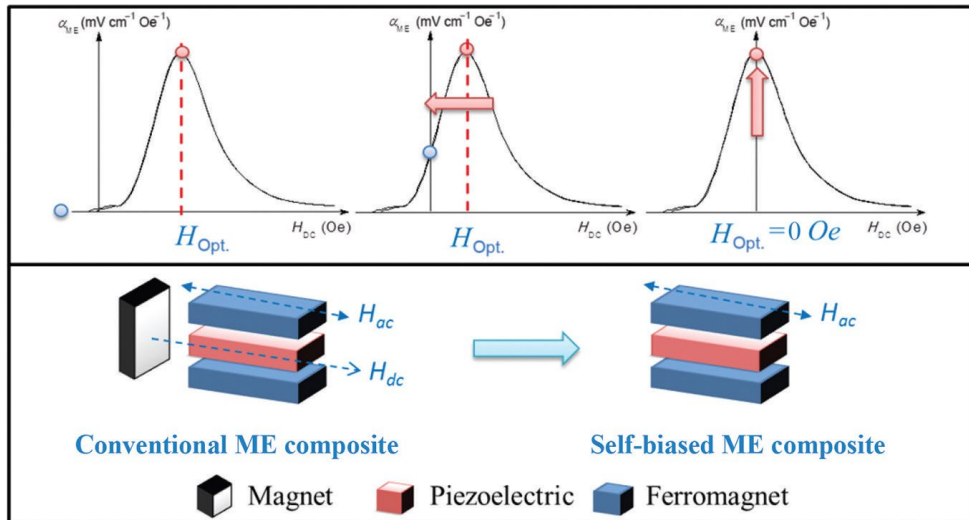


Figure 1.22. Comparison between conventional ME composite and self-biased ME composite [43].

Current research on self-biased ME materials focuses on exploring new material systems, optimizing structures, and expanding their application fields. Advanced synthesis techniques and nanotechnology have enabled researchers to develop materials with exceptional self-biased ME responses. Additionally, optimizing interfacial engineering and multi-field coupling effects have further improved the magnetoelectric conversion efficiency of these materials. The pursuit of optimizing self-biased ME materials has garnered significant attention in both scientific and industrial communities, highlighting their potential to revolutionize a new generation of smart devices.

### 1.5.1 Magnetic Behavior of Magnetostrictive Materials and Self-Biasing in ME

#### Composites

The self-biasing effect observed in magnetoelectric (ME) composites is intrinsically linked to the magnetic behavior of the magnetostrictive materials embedded within these structures. Magnetostrictive materials, play a pivotal role in generating the internal magnetic field necessary to activate the magnetoelectric effect, even in the absence of an external DC magnetic field. This self-generated internal bias is a result of the magnetostrictive phase's inherent magnetic characteristics, including its response to mechanical strain, magnetic hysteresis, and remanent magnetization.

There are five primary mechanisms by which magnetostrictive materials contribute to the self-biasing effect in ME composites:

1. **Functionally Graded Ferromagnetic Effect:** This effect is achieved by introducing a magnetization gradient within the magnetic phase, either through compositional variation or induced stress gradients. These gradients generate an internal magnetic bias field, which activates the ME coupling even without an external field. This mechanism is commonly observed in compositionally graded ferrite-PZT composites.
2. **Exchange Bias Effect:** In multilayer or fine-particle systems, the exchange bias effect arises from the interfacial interaction between ferromagnetic and antiferromagnetic phases. This interaction leads to a horizontal shift in the magnetization hysteresis loop, resulting in self-biasing of the ME composite.

3. **Magnetostriction Hysteresis:** Magnetostrictive materials exhibit hysteresis in their strain response to applied magnetic fields. In the low-field region, the remanent magnetization of the material can maintain the ME effect in the absence of an external bias field, as seen in Ni/PZT bilayers.
4. **Built-in Stress Effect:** Residual stress within the composite, introduced during fabrication (e.g., co-firing), can also act as an internal bias, driving the self-biasing behavior. This is observed in co-fired structures where internal stress alters the magnetostrictive properties of the material, enhancing the ME response.
5. **Non-linear Magnetoelectric Effect:** In the non-linear magnetic response region, materials can exhibit self-biased behavior. In this case, the ME coupling arises from non-linearities in the magnetostrictive phase, leading to self-biasing in the absence of external magnetic fields.

Based on their working mechanisms as mentioned before, self-biased ME composites can be categorized into five main types:

1. **Functionally Graded Ferromagnetic-Based Self-Biased ME Composites**
2. **Exchange Bias Mediated Self-Biased ME Composites**
3. **Magnetostriction Hysteresis-Based Self-Biased ME Composites**
4. **Built-In Stress Mediated Self-Biased ME Composites**
5. **Non-Linear Self-Biased ME Composites**

The self-biasing effect in magnetoelectric (ME) materials is intrinsically linked to the magnetic behavior of the magnetostrictive phase, specifically its hysteresis properties, remanent magnetization, coercivity, and strain response. As illustrated in Figure 1.23, the magnetostrictive phase generates an internal magnetic field that activates the ME coupling effect, even in the absence of an external DC magnetic field. This internal bias is largely due to the remanent magnetization retained after removing the external magnetic field, thereby enabling the composite to sustain the ME effect autonomously.

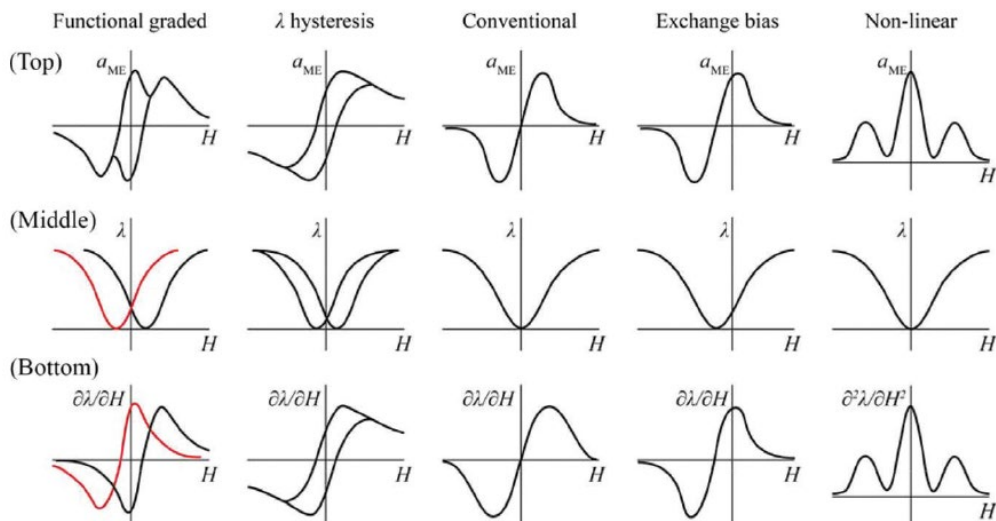


Figure 1.23. Illustration of the four types of self-biased ME composites with the referenced conventional ME composites, showing their corresponding ME coefficient-H (top row), magnetization-H (middle row), and strain-H (bottom row) curves [43].

The unique properties of self-biased ME materials make them highly promising for biomedical applications, particularly in wireless power transfer (WPT) systems for implantable medical devices. Their compact size, low operational frequencies, and ability to provide efficient energy transfer without the need for external biasing make them ideal for long-term implantable devices, such as pacemakers, neurostimulators, and drug delivery systems. The efficient coupling of magnetic fields to electric fields offers a more reliable and safer method of power transfer, ensuring the longevity and stability of the implants while minimizing risks associated with high-frequency electromagnetic exposure. The comparison of some existing self-biased materials is shown in Table 1.2.

Table 1.2. Comparison of the self-biased ME composites in different types.

Type	Combination	Synthesis	$\alpha_{H_{dc}=0}$ ( $\text{V cm}^{-1} \text{Oe}^{-1}$ )	$\alpha_{\max}$ ( $\text{V cm}^{-1} \text{Oe}^{-1}$ )	$f_{H_{ac}}$ (kHz)	References
Single phase	$\text{Sr}_3\text{Co}_2\text{Fe}_{24}\text{O}_{41}$	co-fired	$33 \times 10^{-3}$	$42 \times 10^{-3}$	1	[44]
	$\text{BiFeO}_3$	film	3	3.5	-	[45]
0-3 composite	$\text{CFO}/\text{Sr}_{1.9}\text{Ca}_{0.1}\text{NaNb}_5\text{O}_{15}$	co-fired	$5.7 \times 10^{-3}$	$6.7 \times 10^{-3}$	5	[46]
2-2 composite	$\text{CFO}/\text{PZT}$	film	0.4	0.55	1	[47]
	$\text{Ni}/\text{PZT}$	epoxy	$63.3 \times 10^{-3}$	$87.3 \times 10^{-3}$	1	[48]
	$\text{Ni}/\text{MFC}$	epoxy	1.25	1.38	1	[48]
	$\text{SmFe}_2/\text{PZT}$	epoxy	39.5	48	119.7	[49]
	$\text{PZT}/\text{Ni}/\text{FCNSB}$	epoxy	49.5	51.4	0.35	[50]
	$\text{PZT}/\text{Ni}/\text{FCNSB}$	epoxy	89.2	100	193.3	[50]
	$\text{Ni}/\text{PZT}/\text{Ni}$	epoxy	10	35	resonance	[51]

## 1.6 Previous contributions and objectives of this thesis work

### 1.6.1 Experimental contributions

Our research team at the GeePs laboratory has been investigating magnetoelectric (ME) materials for several years. The initial focus was on studying 2-2 type composite materials, which consisted of PZT piezoelectric plates bonded to Terfenol-D or Galfenol magnetostrictive plates using epoxy glue. Our research on these materials has been approached from both modeling simulations and experimental measurements. Experimentally, our study on Terfenol-D and PZT-based ME composites originated from the doctoral work of Kevin Malleron, who developed an automated measurement bench for characterizing ME materials. This bench allows for precise measurement of the electric response of ME materials under varying DC and AC magnetic fields, facilitating the analysis of magnetoelectric coupling effects, which will be detailed in chapter 2.

The materials were chosen for their exceptional performance: PZT is a commonly used piezoelectric material known for its high piezoelectric coefficients, while Terfenol-D exhibits the highest magnetostriction among commercially available materials. Figure 1.23 shows a Terfenol-D/PZT-5H/Terfenol-D composite sample bonded with epoxy glue. Malleron conducted measurements on this sample under varying DC and small-signal AC magnetic fields. Figure 1.24 presents the ME response of this sample under quasi-static and dynamic regimes. The results showed that the optimal DC magnetic bias field  $H_{dc,opt}$  in the quasi-static regime is approximately 500 Oe in the decreasing  $H_{dc}$  sweep, while the resonance frequency in the dynamic regime is around 66 kHz. The dimensions of the composites were chosen to obtain a

resonance frequency in the 50 to 100 kHz range. This frequency range is suitable for remote power supply applications for biomedical devices implanted in the human body.

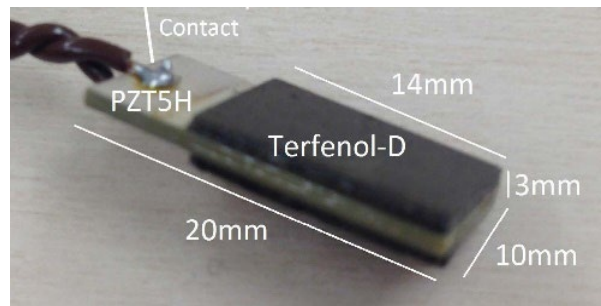


Figure 1.24. Picture of a Terfenol-D/PZT-5H/Terfenol-D composite sample produced using epoxy glue, with sample fabrication and characterization performed during Kevin Malleron's doctoral research.

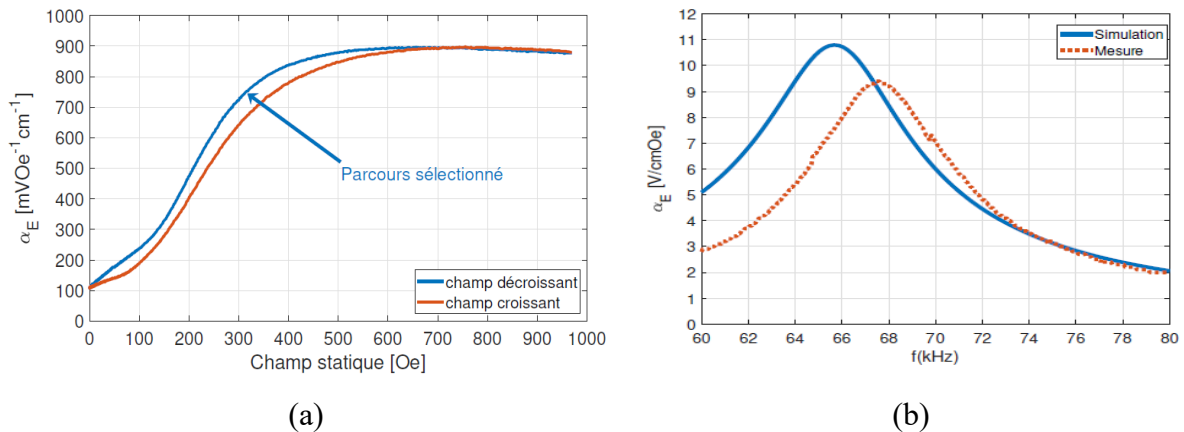


Figure 1.25. Characterization of the magnetolectric response of the Terfenol-D/PZT-5H/Terfenol-D composite: (a) Magnetolectric coefficient variation with static magnetic field in quasi-static conditions; (b) Magnetolectric coefficient variation with frequency in dynamic conditions.

In his doctoral research, Malleron also studied how to optimize the structure of ME composites to achieve the highest possible magnetolectric coefficient and power output. He primarily investigated bilayer (Terfenol-D/PZT) and trilayer (Terfenol-D/PZT/Terfenol) structures, analyzing the effect of dimensional ratios. Furthermore, as shown in Figure 2, he explored the addition of a Metglas magnetostrictive layer between the PZT and Terfenol-D layers, significantly enhancing the magnetolectric response. His work achieved magnetolectric coefficients ( $\alpha_E$ ) of around 200 V/cm·Oe, and power outputs reaching several hundred  $\mu$ W.

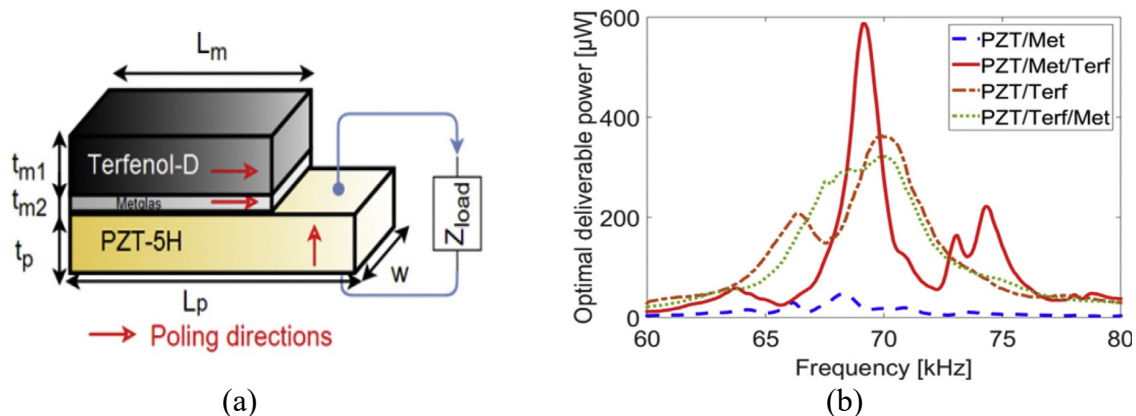


Figure 1.26. (a) Schematic illustration of the PZT-5H/Metglas/Terfenol-D sample. (b) Comparison of the optimal deliverable power across different designs, with or without the inclusion of Metglas [52].

Building upon this foundational work, our research team, in collaboration with the Institut des Nanosciences de Paris (INSP), further expanded the study of ME materials. The main goal of this extended research was to address the issues caused by the use of epoxy glue in the early transducers. Over time, the epoxy glue led to performance degradation and posed challenges in controlling its thickness, which negatively impacted the composite's overall performance. To overcome these challenges, we explored glue-free composite structures by using RF magnetron sputtering to directly deposit the magnetostrictive layers onto the piezoelectric substrate. This method not only improved the mechanical bonding but also avoided the use of toxic elements like lead, reducing the need for rare-earth materials, which addresses environmental concerns. Nickel (Ni) was selected as the magnetostrictive material, while monocryalline lithium niobate ( $\text{LiNbO}_3$ ) was used as the piezoelectric substrate, forming a combination that offered both high performance and sustainability.

The initial study of the Ni/ $\text{LiNbO}_3$  composite (see Figure 1.27) was conducted by postdoctoral researcher Ulisses Acevado. His experimental results demonstrated that the Ni/ $\text{LiNbO}_3$  ( $36^\circ$  Y-cut) composite exhibited self-biased ME behavior. This discovery was significant because it showed that the composite could achieve magnetization without the need for an external magnetic field.

As shown in Figure 1.28, while the ME coefficient at  $H_{dc} = 0$  Oe does not reach its maximum value, it displays a relatively large remanent ME coefficient. This indicates that the composite can maintain significant magnetoelectric response even without external magnetic field, confirming its self-biased characteristic. This self-biased effect is highly advantageous for low-power applications, particularly in implantable biomedical devices where applying an external magnetic field is difficult.

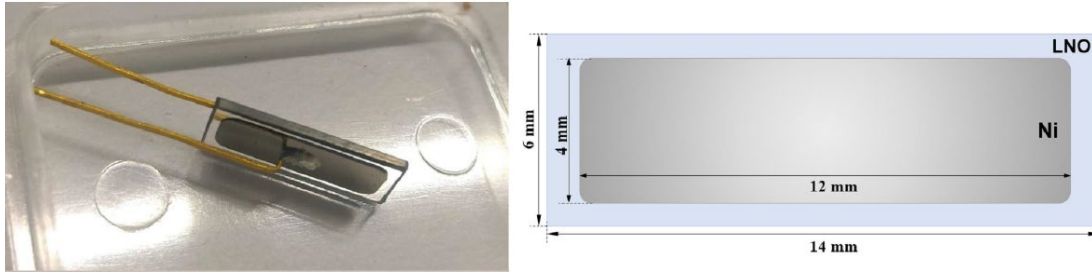


Figure 1.27. Picture of a ME Ni/LiNbO<sub>3</sub>/Ni ME composite sample and its dimensions.

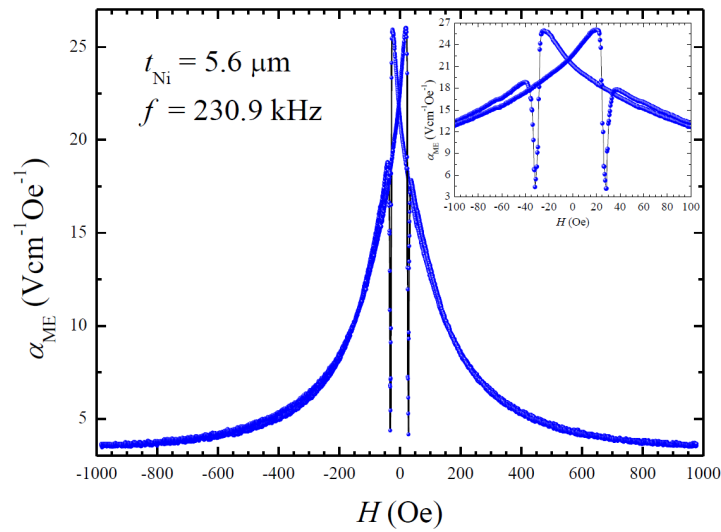


Figure 1.28. ME coefficient as a function of the static magnetic field applied to the Ni/LiNbO<sub>3</sub>/Ni composite.

## 1.6.2 FEM modeling contributions

The initial work on 2D modeling of magnetolectric (ME) composites in our research group was carried out by Gang Yang, who used MATLAB to develop models for traditional laminate rectangular ME composites. This foundational model enabled the study of magnetostrictive and piezoelectric interactions within the composite structure, providing valuable insights into the basic magnetolectric coupling effect. Building on this, Kevin Malleron extended Yang's code to perform simulations comparing various combinations of ME composites within the rectangular laminate structure. Malleron's work offered a deeper understanding of how different material compositions and configurations influence the overall ME properties, which was crucial for guiding further material design and selection.

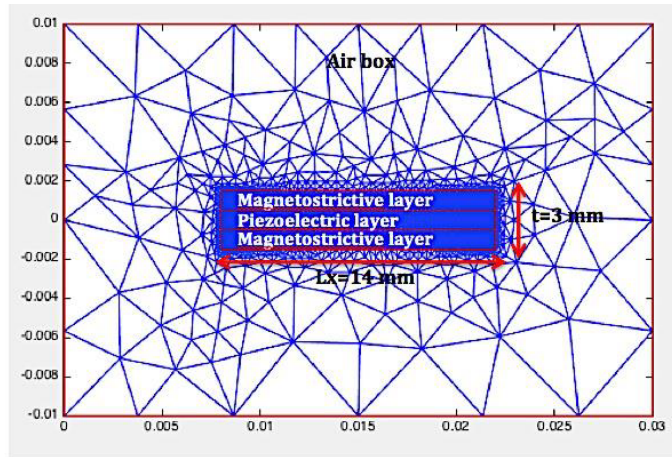


Figure 1.29. The studied trilayer ME composite in 2D FEM model.

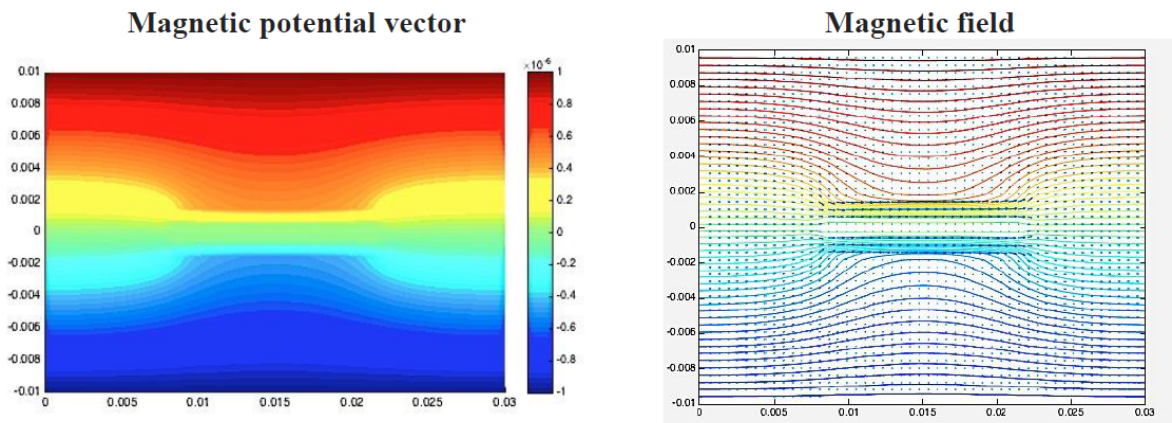


Figure 1.30. Display of magnetic results for a trilayer Terfenol-D/PZT-5A/Terfenol-D composite.

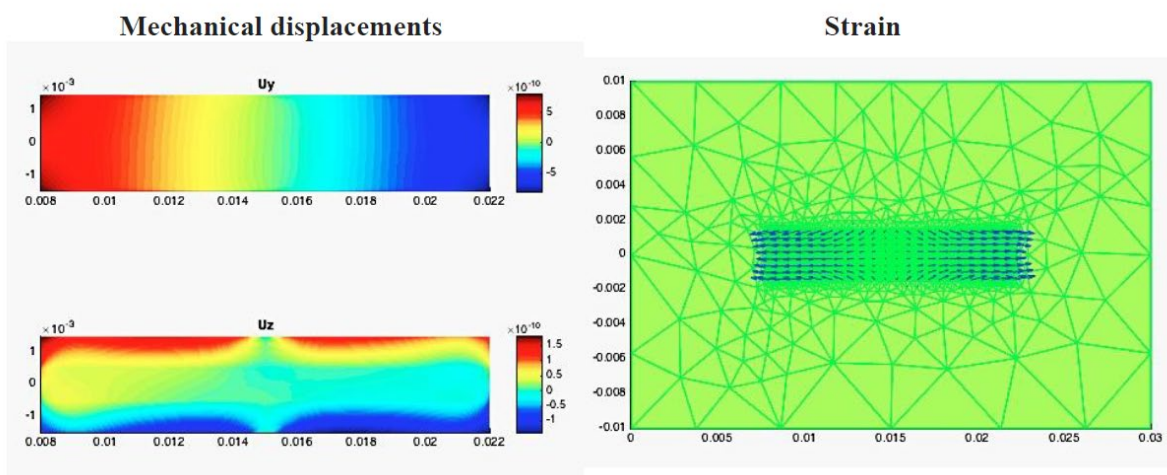


Figure 1.31. Display of mechanical results for a trilayer Terfenol-D/PZT-5A/Terfenol-D composite.

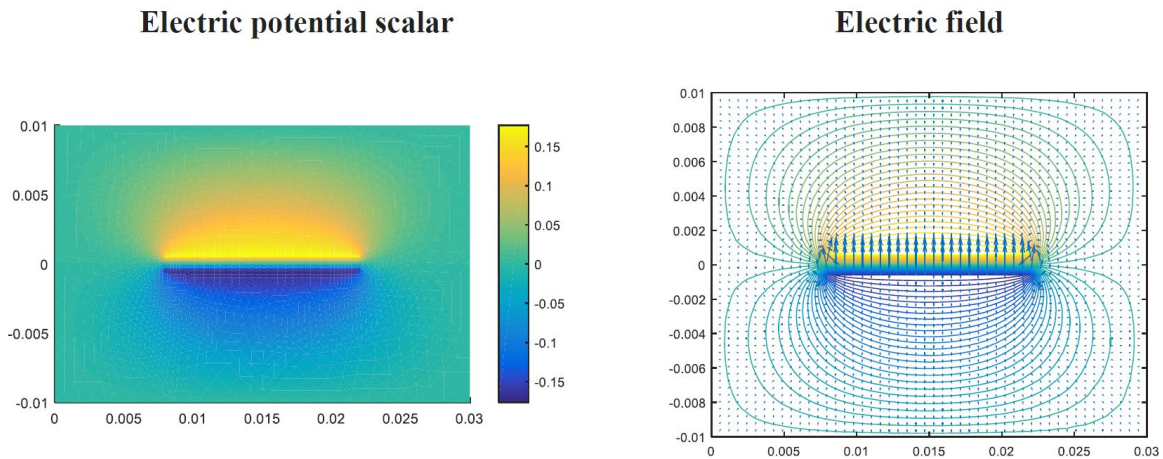


Figure 1.32. Display of electric results for a trilayer Terfenol-D/PZT-5A/Terfenol-D composite.

While 2D finite element modeling (FEM) is an effective tool for initial simulations, it faces limitations when dealing with complex geometries. In such cases, 2D models are unable to accurately capture changes in material properties, which restricts their ability to precisely describe asymmetric structures, edge stresses, or localized deformations. When the direction of the studied material is not included in the 2D modeling plane, we also cannot obtain accurate results in that direction. These factors can significantly impact the overall performance of ME devices. However, the key advantage of 2D FEM lies in its lower computational cost, making it ideal for preliminary analysis or simplified geometrical simulations, where it can quickly provide insights into the basic behavior of the system. In contrast, 3D FEM is capable of fully capturing anisotropies, edge effects, and three-dimensional stress distributions, which are critical for real-world applications. Therefore, although 2D models offer faster problem-solving for initial stages, they are more limited in scope compared to 3D FEM, which provides higher accuracy in simulating real device dimensions and more complex interactions.

Recognizing these limitations, our research group transitioned to 3D modeling. Zhi Qin's work initially focused on separately modeling the magnetostrictive and piezoelectric phases in 3D, providing a detailed analysis of each phase's behavior in a 3D context and capturing complex interactions that 2D models could not describe. Later, Tuan-An integrated these phase-specific models into a unified 3D framework, enabling simulation of the entire ME composite. His research extended beyond traditional rectangular laminate structures to include more complex geometries, such as laminate disk structures. This advancement greatly enhanced the accuracy of our ME composite modeling, allowing us to explore a wider range of materials and geometries for applications like wireless power transfer and energy harvesting.

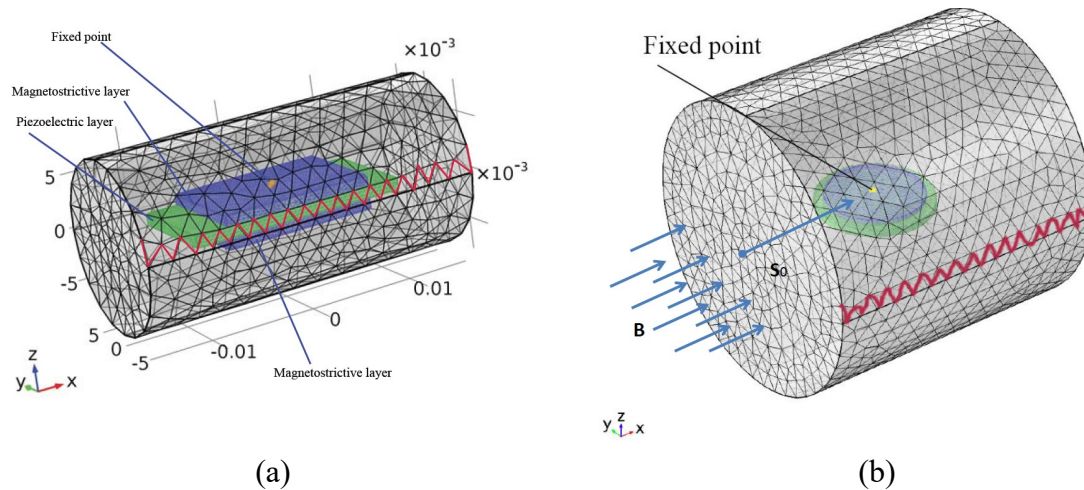


Figure 1.33. Different geometries modeled using 3D FEM simulations: (a) trilayer laminate in rectangular form, (b) trilayer laminate in disk form.

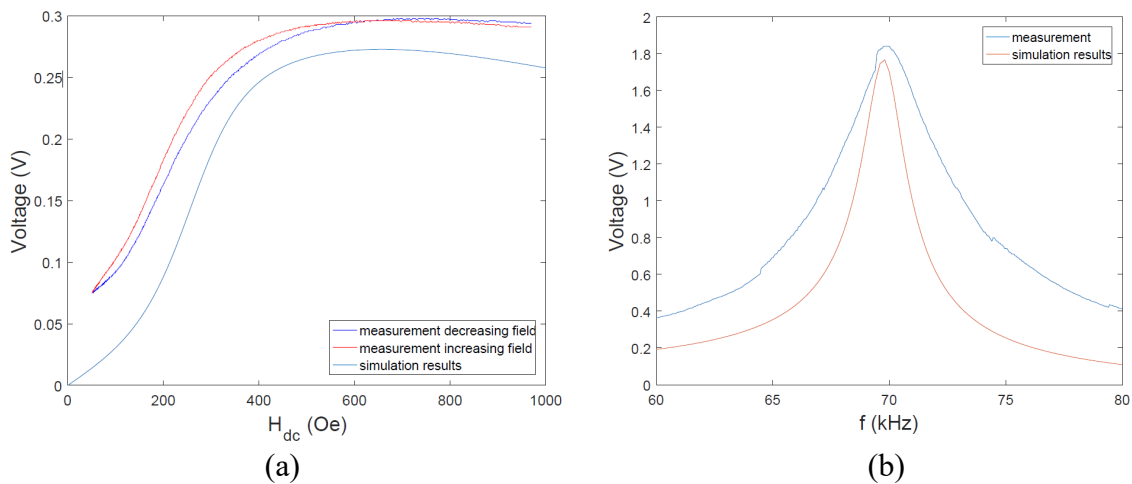


Figure 1.34. Simulation results of the electric output voltage of a trilayer laminate ME composite using 3D FEM model: (a) in the quasi-static regime (b) in the dynamic regime.

## 1.7 Conclusion

In this chapter, we explored the fundamental concepts and classifications of magnetoelectric (ME) materials, focusing primarily on composite materials. Our research emphasizes self-biased ME materials, which are particularly promising for biomedical applications like wireless power transmission. These materials offer significant advantages, such as functioning without a constant magnetic bias, making them ideal for use in the human body. Their compact design enables efficient energy transfer while meeting safety regulations, positioning them as excellent candidates for medical implants where space and energy efficiency are critical.

In my doctoral research, the focus is on investigating how the sputtering process in the Ni/LiNbO<sub>3</sub> material combination leads to the emergence of self-biased magnetoelectric (ME) properties. A key aspect of this research is understanding the mechanisms behind this ME self-

biasing behavior, which eliminates the need for external magnetic fields. I have also studied and mastered the team's existing modeling approaches for ME materials. By comparing the modeling predictions with the experimental measurements of the materials, I aim to verify the accuracy of our models. Furthermore, using these models, I intend to conduct simulations to study how the thickness ratio of nickel and  $\text{LiNbO}_3$  within the composite affects the magnetoelectric performance. This approach will help optimize the magnetoelectric response of the composites. By fine-tuning the thickness ratios, we hope to enhance the overall performance, contributing valuable insights into the design of ME materials for low-power devices and biomedical applications.

## Chapter2. Study of self-biased ME behaviors

In this chapter, an in-depth examination of the ME materials investigated in our research is presented. The fabrication of our magnetoelectric composites involves the growth of ferromagnetic nickel layers on piezoelectric substrates via RF sputtering. Given that the piezoelectric substrates utilized are commercially sourced, a detailed material characterization, including texture analysis and magnetization measurements of the nickel films, is imperative to evaluate their integrity. This stage is followed by the development of nickel films across diverse cuts of  $\text{LiNbO}_3$  piezoelectric substrates, as well as on alternative piezoelectric materials, to discern the magnitude and the presence of self-bias within the resulting magnetoelectric responses.

### 2.1 Fabrication of ME transducers

In this thesis work, we primarily investigated ME transducers fabricated using radio frequency (RF) sputtering technology. This process involves depositing high-purity nickel films ( $\text{Ni} > 99.95\%$ ) on piezoelectric substrates. These transducers are produced under the operation of Loic Becerra at the INSP (Institute des NanoSciences de Paris) laboratory. RF sputtering is a Physical Vapor Deposition (PVD) technique, utilizes a radio frequency power source to ionize argon gas in a vacuum, creating a plasma. Ions from this plasma bombard a high-purity Ni target, causing nickel atoms or molecules to be ejected and deposited onto the substrate, thereby forming uniform and high-quality films. These Ni films act both as magnetostrictive layers and as electrodes for the piezoelectric material, making this method particularly suitable for producing high-precision polycrystalline films as it allows for effective control over the film deposition process and thickness.

Prior to the sputtering deposition, each piezoelectric substrate was chemically prepared using an acetone cleaner in an ultrasonic bath, and the surfaces were in situ cleaned with argon plasma. The sputtering process was conducted at room temperature within a chamber under an argon atmosphere, maintained at a pressure of  $10^{-3}$  mbar, and with a supply power of 500 W. Ni films were deposited on each face of the piezoelectric substrate without continuous substrate rotation, achieving a growth rate of approximately 55.5 nm/min. During the deposition, the Ni target and the substrates were kept in a planar configuration. To prevent potential electrical connections between the Ni films, a 1 mm gap was maintained between the Ni films and the edges of the piezoelectric substrate.

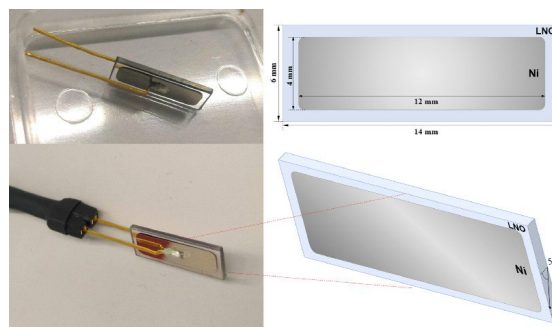


Figure 2.1. A trilayer  $\text{Ni}/\text{LiNbO}_3/\text{Ni}$  ME transducer fabricated using RF sputtering, with gold-plated leads bonded to the nickel films on both surfaces using conductive epoxy for electrical contact.

## 2.2 Magnetostrictive Polycrystalline Nickel

Nickel (Ni), characterized by an atomic number of 28 and an atomic weight of 58.6934, possesses a density of 8908 kg/m<sup>3</sup>, a melting point of 1455°C, and a boiling point of 2913°C. Ranking as the 24th most abundant element in the Earth's crust, nickel holds the position of the fifth most abundant element by weight, following iron, oxygen, magnesium, and silicon. In its elemental form, nickel presents as a silver-white metal, notable for its high thermal and electrical conductivity. Owing to its chemical properties, luster, and affordability, nickel and its compounds find extensive usage across various industrial and commercial domains. The widespread application of nickel can be attributed to its unique blend of exemplary physicochemical properties. Not only is it resilient to extremely high temperatures, corrosion, and oxidation, but it also exhibits significant ductility, alloys with ease, and is completely recyclable.

We chose nickel as the magnetostrictive material for our study for several key reasons. Previous research on self-biased magnetoelectric (ME) composite materials has shown that nickel, when bonded to piezoelectric materials using epoxy glue, can exhibit significant self-biased ME behavior [43]. Furthermore, pure nickel is a commonly available target material for RF sputtering, which allows for its direct deposition onto any piezoelectric substrate to form ME composite materials without the need for glue. In addition, as this material is a good conductor, it can be used as electrodes when used in a laminar composite, deposited on both sides of a piezoelectric substrate.

## 2.3 Piezoelectric monocrystalline LiNbO<sub>3</sub>

Lithium niobate (LiNbO<sub>3</sub>) single crystals, can be industrially produced as piezoelectric materials, are not only easily accessible, devoid of rare-earth and toxic elements, and economically viable. These materials have been extensively exploited in the development of acoustics and optical devices, presenting a similar efficiency in energy harvesting to the commonly used PZT ceramics [53]. The major advantages of LiNbO<sub>3</sub> over PZT encapsulate extreme chemical inertness, and high Curie temperature (> 1150 °C). These properties complement their widely researched and practically applied potential in optoelectronics and nonlinear optics.

Significantly, the biocompatibility of LiNbO<sub>3</sub> renders it an ideal candidate material, capable of interacting safely with biological bodies, crucial for implants to prevent potential bio-rejection or inflammatory responses [54]. Moreover, LiNbO<sub>3</sub> demonstrates substantial corrosion resistance, another pivotal property for implant materials since the intra-body environment frequently contains elements that could induce material degradation. Unifying its piezoelectricity, biocompatibility, and corrosion resistance, LiNbO<sub>3</sub> demonstrates substantial future application potential in the biomedical implant domain. The primary focus on LiNbO<sub>3</sub> materials stems from their good piezoelectric properties.

During this study, we discovered that their thermal expansion for certain commercially available cuts can lead to a thermal expansion mismatch during the RF sputtering for the growth of magnetostrictive Ni, leading to obtain self-biased Magnetoelectric behavior, which will be detailed in this chapter.

The coordinate system used to describe the physical tensor properties of LiNbO<sub>3</sub> employs a Cartesian system (X,Y,Z), with its crystallographic coordinate system being (a,b,c). Conventionally, the coordinate system is selected such that: the Z axis aligns with the electric polarization c-axis, the X axis is perpendicular to the mirror plane, and the Y axis is chosen to establish a right-handed system, thereby residing within a mirror symmetrical plane. For a flat LiNbO<sub>3</sub> substrate shaped as a rectangular parallelepiped, if its thickness (the minimal edge length) aligns with one of the Cartesian system axes (X,Y,Z), it is denoted as an LiNbO<sub>3</sub> substrate of that respective axis-cut.

Figure 2.2 illustrates a LiNbO<sub>3</sub> substrate of Y-cut with a rotation angle  $\theta$  around the X axis, and the conventional 36°-Y-cut, common in most publications, is achieved by a 36° counterclockwise rotation around the X axis. In the IEEE standard [55], Figure 2.3 depicts  $l$ ,  $w$ , and  $t$  as the length, width, and thickness of substrate, respectively. The conventional 36° Y-cut is denoted as (YXl) 36°, implying that the Y axis aligns with the substrate thickness, the X axis is the rotation axis and aligns with the substrate length  $l$ , and  $\theta$  is the counterclockwise rotation angle. For the remainder of this report, the  $\theta$ -Y-cut is expressed as (YXl)  $\theta$  Y-cut.

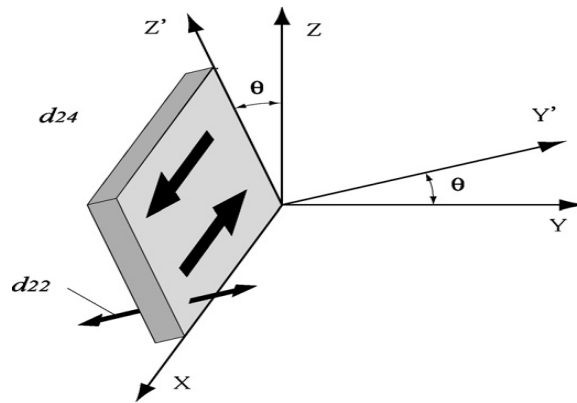


Figure 2.2. A Y-cut crystal substrate with a rotation of  $\theta$  about the X-axis within the (XYZ) coordinate system [56].

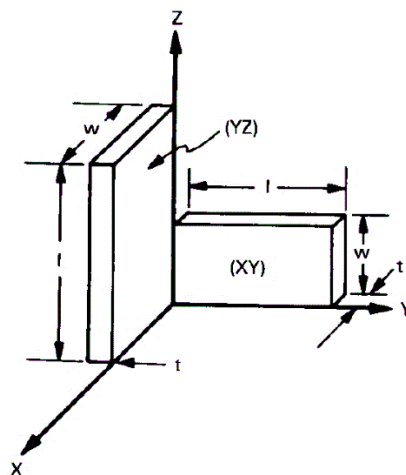


Figure 2.3. Non-rotating flat substrates [55].

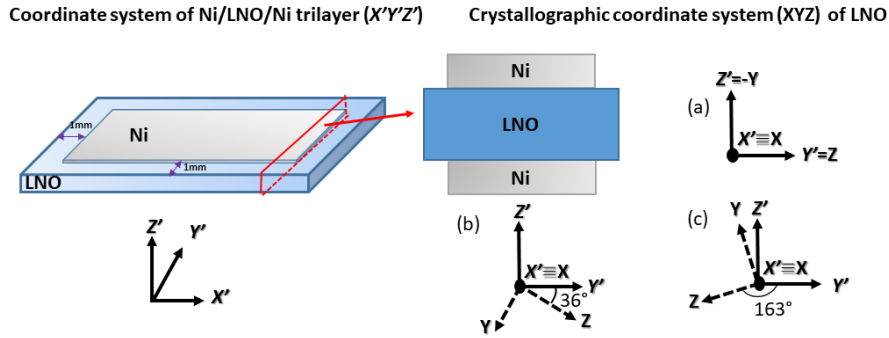


Figure 2.4. Illustration of trilayer ME transducer with two different cuts: 36° Y cut and the 163° Y cut.

Dr. Ulisses ACEVADOS initially investigated Ni/LiNbO<sub>3</sub>/Ni magnetoelectric composites using a 36° Y-cut LiNbO<sub>3</sub>, which exhibited self-biased ME behavior. As shown in Figure 2.5, the effective electromechanical coupling coefficient  $k_{eff}$  is a crucial parameter that describes the efficiency with which a piezoelectric material converts mechanical energy into electrical energy and vice versa. The Figure 2.5 illustrates  $k_{eff}$  for different Y-cut angles of LiNbO<sub>3</sub>, including variations in the "quasi-shear" and "quasi-extensional" modes with respect to the cut angles.

For the 36° Y-cut, the quasi-longitudinal coupling is dominant, indicating that the material effectively converts mechanical strain into an electric signal along a single axis. As shown in Figure 2.4, this occurs along the Y axis (Z' axis), which corresponds to the thickness of the piezoelectric substrate, thus making it a quasi-longitudinal cut.

In contrast, the 163° Y-cut is a quasi-shear cut, where the longitudinal piezoelectric coupling factor approaches zero, as seen from the drop in the "quasi-extensional" curve in Figure 2.5. Simultaneously, the "quasi-shear" coupling factor is near its maximum at this angle, suggesting that mechanical shear strains are more efficiently converted into electrical induction.

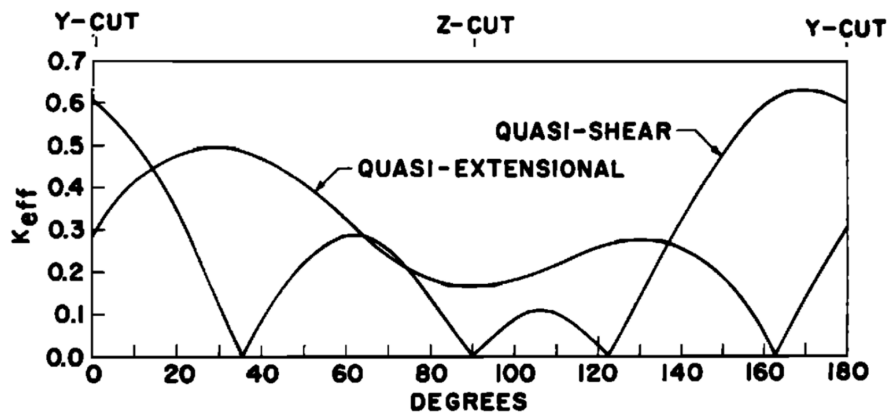


Figure 2.5. Effective electromechanical coupling coefficients  $k_{eff}$  for lithium niobate (LiNbO<sub>3</sub>) at various Y-cut angles, showing the variations in quasi-shear and quasi-extensional modes [57].

In our subsequent research, we chose the 163° Y-cut to further explore the self-biased ME behavior in Ni/LiNbO<sub>3</sub>/Ni composites, investigating whether this behavior is related to the unique properties of different cuts and how it affects the overall magnetoelectric performance.

This comparison will help to deepen our understanding of piezoelectric anisotropy's role in achieving self-biased ME behavior and explore how to optimize the magnetoelectric material's performance using the effective coupling coefficient.

### 2.3.1 Comparison of the piezoelectric performance

When selecting the appropriate piezoelectric material for the use in biomedical implantable applications, we need to delve into a series of key parameters to ensure that the chosen material meets the requirements of a specific application:

- piezoelectric coefficients (revealing the relationship between the electric field and strain or stress).
- mechanical quality factor (reflecting the degree of mechanical energy loss).
- dielectric constant (indicating the material's response to the electric field).
- electromechanical coupling coefficient (measuring the conversion efficiency between electrical and mechanical energy).
- Curie temperature (limiting the maximum working temperature of the material).
- density (affecting the mass and size of the device).
- strength and stiffness (determining the performance and durability of the material under mechanical stress).
- frequency stability (especially important in applications where precise frequency control is required).
- thermal expansion coefficient (reflecting the size stability of the material with temperature changes).
- corrosion resistance and chemical stability (critical especially in harsh environments).
- biocompatibility (crucial in biomedical applications).

As aforementioned, when compared to PZT ceramics, LiNbO<sub>3</sub> material demonstrates superior biocompatibility, corrosion resistance, and chemical stability, illustrating its suitability for biomedical applications, particularly considering its non-inclusion of toxic lead. And in the following, we aim to compare 2 common cuts of LiNbO<sub>3</sub> 36° Y-cut and 163° Y-cut LiNbO<sub>3</sub> with the most studied PZT ceramics through the electromechanical coupling coefficient and the strain driven Figure of Merit, providing a comprehensive analysis of their respective capabilities and performances.

#### 2.3.1.a. Electromechanical coupling coefficient

Electromechanical coupling coefficient ( $k$ ) is a crucial parameter in characterizing piezoelectric materials. It describes the efficiency with which electrical energy is converted to mechanical energy (and vice versa) in a piezoelectric material. Essentially, it provides insight into how effectively a piezoelectric material can transform electrical energy to mechanical vibrations and is often used to gauge the performance of piezoelectric devices.

The coefficient is dimensionless and is generally expressed as a number between 0 and 1. A higher electromechanical coupling coefficient indicates a more efficient conversion between electrical and mechanical energy, and can be estimated by:

$$k_{ij} = \sqrt{\frac{d_{ij}^2}{s_{ij}^E \epsilon_{ii}^T}} \quad 2.1$$

where  $d_{ij}$  is the piezoelectric coefficient,  $s_{ij}^E$  is the compliance coefficient under a constant electric field  $E$ , and  $\epsilon_{ii}^T$  is the dielectric permittivity under a constant mechanical stress  $T$ .

There are different types of electromechanical coupling coefficients, such as  $k_{33}$  (longitudinal piezoelectric mode),  $k_{31}$  (transverse piezoelectric mode), and  $k_{15}$  (shear piezoelectric mode), which refer to the efficiency of energy conversion in different modes of vibration and polarization direction.

### 2.3.1.b. Figures of Merit of piezoelectric material in ME composite

The role of piezoelectric material in a ME composite is as a strain-driven energy harvester, because when the magnetostrictive material is stimulated by a magnetic field, it undergoes deformation and transfers this deformation to the piezoelectric material. We should refer to the strain driven Figures of Merit ( $FOM^S$ ) that represent the density of energy of a piezoelectric material or system that is related to the capability for converting applied strain into electrical energy, as delineated in references [58], [59], and can be estimated by:

$$FOM_{ij}^S = \frac{d_{ij}^2}{s_{ii}^E s_{ii}^D \epsilon_{jj}^T} \quad 2.2$$

Where  $s^D$  is the compliance under constant electric displacement  $D$ , and we can calculate by using:

$$s_{ii}^D = s_{ii}^E (1 - k_{ij}^2) \quad 2.3$$

The unit of  $FOM^S$  is  $J \cdot m^{-3}$ .

Table 2.1. comparison of transverse piezoelectric mode for ME L-T working mode

Material	$s_{11}^E$ ( $pm^2 \cdot N^{-1}$ )	$s_{11}^D$ ( $pm^2 \cdot N^{-1}$ )	$\epsilon_{33,r}^T$	$d_{31}$ ( $pC \cdot N^{-1}$ )	$k_{31}$	$FOM^S$ ( $KJ \cdot cm^{-3}$ )
PZT-5A	16.4	14.5	1700	171	0.34	8.2
PZT-5H	15.9	12.9	3935	320	0.44	14.3
LiNbO3 (36° Y-cut)	5.78	5.2	65.34	17.58	0.3	17.8
LiNbO3 (163° Y-cut)	5.78	5.2	79.38	-19.79	0.31	18.55

According to Table 2.1, the comparison of the transverse piezoelectric mode for ME L-T working mode, by comparing the coupling coefficient and the Figure of Merit, shows that the piezoelectric capabilities and performances of these two cuts of LiNbO<sub>3</sub> are comparable to those commonly used and studied of PZT ceramics. This makes LiNbO<sub>3</sub> a suitable choice as a replacement for PZT ceramics in biomedical implantable applications.

## 2.4 Characterization of ME transducers

Regarding the characterization of the ME transducer, we utilized a measurement platform developed by a previous doctoral student, Kevin Malleron, from our GeePs laboratory [52]. During this thesis work, I adapted this measurement bench and the control programs for the new ME composites, I redid all the calibrations, and I made modifications to characterize the samples under new conditions.

As shown in Figure 2.6 and Figure 2.7, when measuring ME materials, we place the ME sample horizontally within a coil located at the center of the rail. This coil is powered by an arbitrary waveform generator (Rohde & Schwarz HM8150) to generate and adjust the frequency and strength of a dynamic excitation magnetic field  $H_{ac}$ . The static excitation magnetic field  $H_{dc}$  is produced by two permanent magnet blocks placed on either side of the coil. By moving these magnets with a stepper motor, we alter their distance  $d$  between these magnets, thereby adjusting the strength of  $H_{dc}$  exerted on the ME sample. The magnetic fields are then in the plane of the sample, which is placed at the center of the coil and parallel to the axis along the length of the sample.

An oscilloscope (Keysight MSO7054A) is used to display the input signals  $V_{coil}$  (coil voltage) and output signals  $V$  (voltage between electrodes of the ME composite, in an open circuit condition). All measurements are controlled through a Graphical User Interface (GUI) programmed in Matlab.

As shown in Figure 2.7b, the radius of the coil designed by Malleron for generating  $H_{ac}$  in the measurement bench is 8 mm (with a cylindrical coil support with a thickness of 1 mm, which not only supports the coil but also prevents direct contact between the coil and the sample during measurements). When the maximum dimension of the sample's plane exceeds 14 mm, we cannot apply a magnetic field perpendicular to this direction due to the size limitations. Therefore, in my doctoral research, based on the required strength of the dynamic magnetic field and the frequency range for measurement, I designed a coil with a radius of 13 mm (with a cylindrical coil support with a thickness of 1 mm). This allows us to measure the frequency and magnetic field strength range for materials with a maximum plane dimension of up to 24 mm.

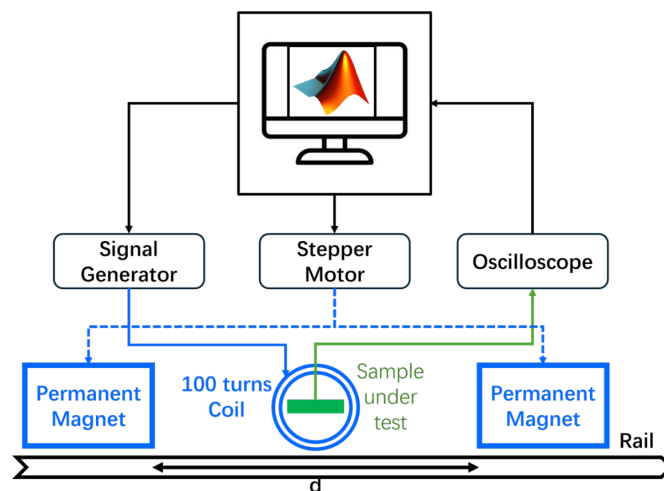


Figure 2.6. Schematic illustration of ME experimental bench

As mentioned before, our research on ME materials as ME transducer is conducted in two regimes: quasi-static and dynamic (harmonic), and the ME coefficient  $\alpha_E$  can be obtained with  $\alpha_E = \delta V / (\delta H_{ac} \cdot t_p)$ . In the quasi-static regime, the dynamic magnetic field is kept constant to study how the ME coefficient changes with variations in the static magnetic field. In the dynamic regime, while the static magnetic field remains constant, since the ME coefficient is related to the unit strength of the dynamic magnetic field, we focus on how the ME coefficient changes with the frequency of the dynamic field. In the following, a detailed explanation of the measurement process for obtaining the ME coefficient will be provided through a measurement of a Terfenol-D/PZT ME transducer sample.

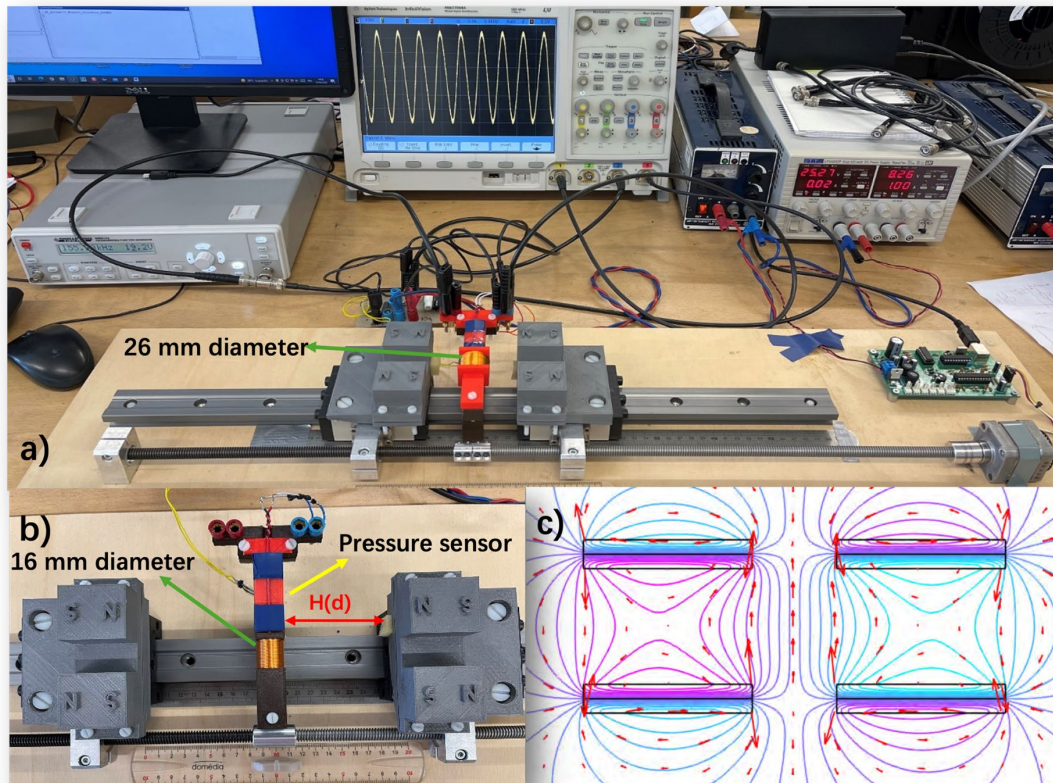


Figure 2.7. (a) Experimental bench for the characterization of ME transducer, with a coil of 26 mm diameter (red); (b) zoom in the part for magnetic excitation field: two permanent magnets for static excitation field  $H_{dc}$  and a coil of 16 mm diameter (brown) for dynamic excitation field  $H_{ac}$ ; (c) Illustration of static magnetic field distribution generated by the two permanent magnets (in the same direction as the dynamic magnetic field).

#### 2.4.1 Measurement in quasi-static regime

As previously mentioned, the strength of the static magnetic field,  $H_{dc}$ , is determined by the distance  $d$  between the two permanent magnets, which can be identified by the number of steps taken by the stepper motor. When the magnets are in their closest position, i.e., in contact with the pressure sensor (see Figure 2.7b), the step count is zero, and the static magnetic field strength is at its maximum. The maximum distance between any one of the permanent magnets and the central coil is 20 cm, equivalent to 20,000 steps. Figure 2.8 shows the calibration we conducted using a Gaussmeter on two coils with diameters of 16 mm (support in brown color)

and 26 mm (support in red color), mapping the static magnetic field strength relative to the motor steps, which indicates the distance between the magnets and the central coil.

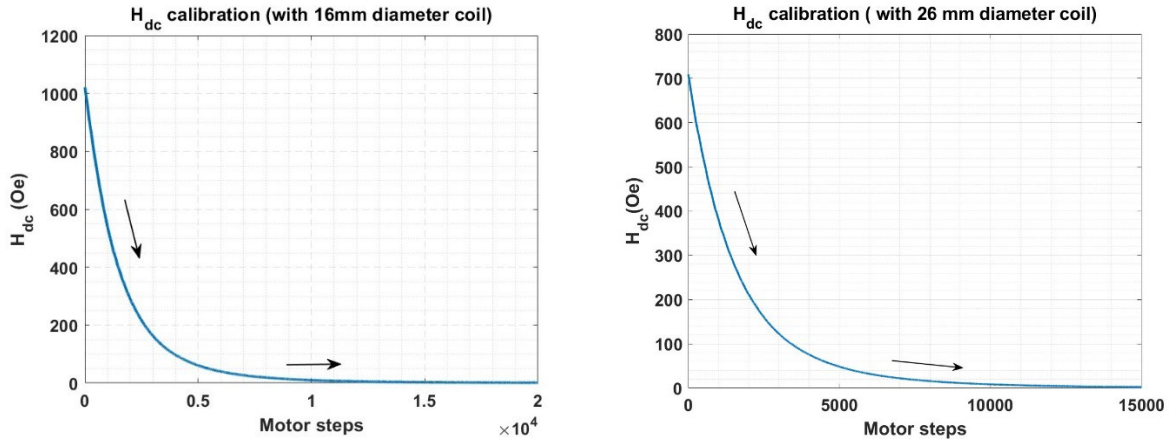


Figure 2.8. Static magnetic field calibration with a coil with (a) diameter of 16 mm and (b) diameter of 26 mm.

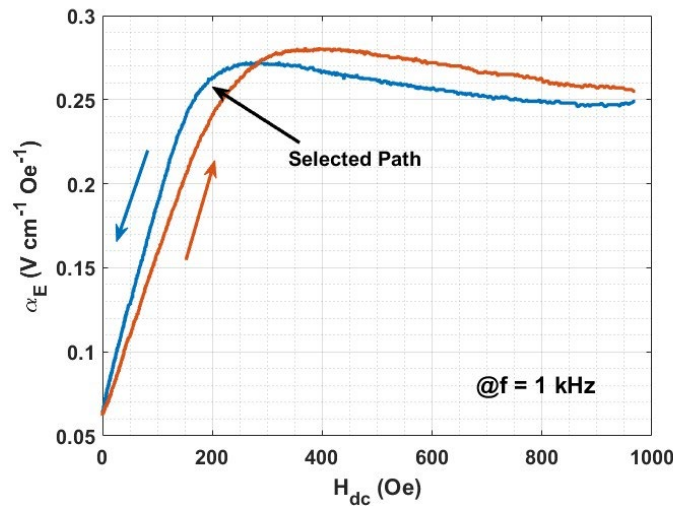


Figure 2.9. ME coefficient measurement in quasi-static regime for a bilayer Terfenol-D/PZT-5H transducer.

When characterizing the ME coefficient in the quasi-static regime, we typically choose a frequency of 1 kHz and a constant strength in RMS (Root Mean Square) for the dynamic magnetic field  $H_{ac}$ . And by varying the distance between two permanent magnets to achieve an  $H_{dc}$  sweep, we measure the corresponding open-circuit voltage  $V$  of the ME sample, and based on the relationship between the ME coefficient  $\alpha_E$  and  $V$ , we can obtain the  $\alpha_E$  as a function of  $H_{dc}$ . As shown in Figure 2.9, we observed the ME coefficient curves are nonlinear and hysteresis, resulting primarily from the nonlinear magnetic hysteresis behavior of the magnetostrictive phase. We select the blue curve (decreasing  $H_{dc}$  sweep) as our reference and determine the maximum value of the ME coefficient along with its corresponding  $H_{dc}$  value. Subsequently, we select this value as the magnetic bias field  $H_{bias}$ , for the subsequent measurements in the dynamic regime.

## 2.4.2 Measurement in dynamic regime

The dynamic magnetic field  $H_{ac}$  is produced by two coils consisting of 100 turns, with a common length of 20mm and their respective diameters of 16mm and 26mm, as depicted in Figure 2.6. Each coil is powered by the arbitrary waveform generator, which allows us to alter the dynamic magnetic field in both frequency and amplitude through the dynamic AC current control. Since we do not possess a gaussmeter capable of measuring high-frequency magnetic fields with a probe that can be inserted into both coils, we verify the dynamic magnetic field of 1 Oe in RMS through calculation. We use a gaussmeter (HIRST GM08) to measure the static magnetic field as a function of the direct current in each coil respectively, as illustrated in Figure 2.10, where the slope is denoted as  $B(I)$ , it worth noting that  $0.1 \text{ mT} = 1 \text{ Oe}$  in the air, and we could transfer in unit Oe/A. Subsequently, we measured the internal impedance  $Z_{coil}$  using an impedance analyzer (HP4194A) for each coil, separately. And then, the amplitude of the control voltage provided by the arbitrary waveform generator for a  $H_{ac}$  of 1 Oe in RMS, as a function of frequency, is calculated as:

$$V_{GBF} = \sqrt{2}(Z_{coil} + Z_{GBF}) / B(I) \quad 2.4$$

In this way, we can use the formula to calculate the voltage that each coil should receive within a fixed frequency range. Additionally, we should import these results into our Matlab GUI during the frequency sweep in dynamic regime for the chosen coil.

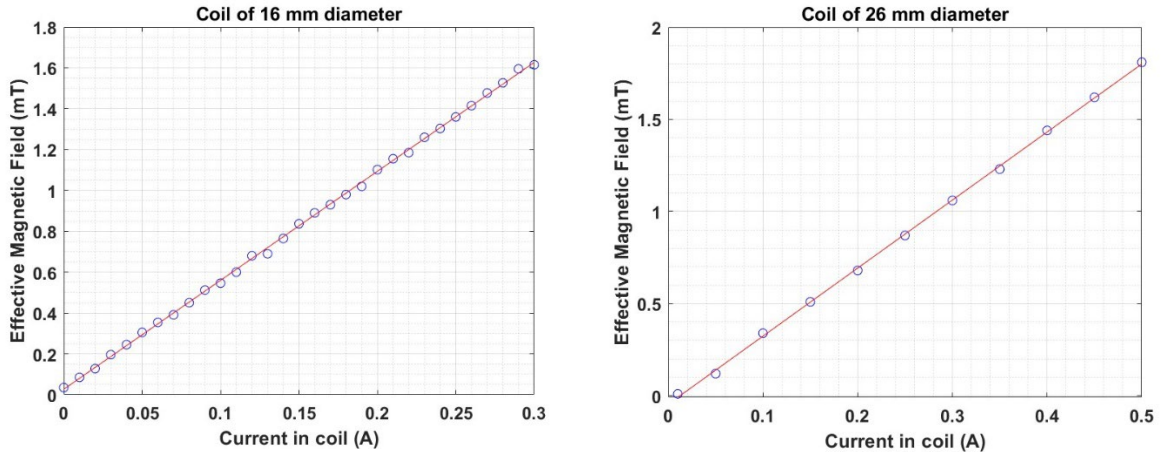


Figure 2.10. Effective magnetic field as a function of input DC current curves of both used coils, for the calibration of  $H_{ac}$ .

Once we know the value of  $H_{bias}$ , we fix this value for static magnetic excitation  $H_{dc}$ , which corresponds to a relative distance between the permanent magnets and the central coil. As shown in Figure 2.11, during our measurement in dynamic regime, we maintained the intensity of  $H_{ac}$  and performed a frequency sweep around the first longitudinal electromechanical resonance (EMR) frequency of our ME sample to find the optimal ME coefficient at its ME resonance frequency. Additionally, we can estimate approximately this value using an analytical formula when the lengths of magnetostrictive and piezoelectric phase are equivalent or approximate, as follows [60]:

$$f_r = \frac{1}{2l} \sqrt{\frac{1}{\bar{\rho} \bar{s}_{11}}} \quad 2.5$$

where  $l$  is the length of the ME composite,  $\bar{\rho}$  is the average density, and  $\bar{s}_{11}$  is the equivalent elastic compliance in length direction in global coordinate of ME material. The values of  $\bar{\rho}$  and  $\bar{s}_{11}$  can be determined by using a magnetostrictive volume fraction denoted as  $n$ , when the in-plane dimensions of the magnetostrictive and piezoelectric phases are close in size:

$$n \cong \frac{t_{m,total}}{t_{m,total} + t_{p,total}} \quad 2.6$$

$$\bar{\rho} = n\rho_{mag} + (1-n)\rho_{piezo} \quad 2.7$$

$$\bar{s}_{11} = \frac{s_{33}^H s_{11}^E}{n s_{11}^E + (1-n) s_{33}^H} \quad 2.8$$

where  $\rho_{mag}$  and  $\rho_{piezo}$  is mass density, and  $t_{m,total}$  and  $t_{p,total}$  are the total thickness, for magnetostrictive and piezoelectric materials respectively.

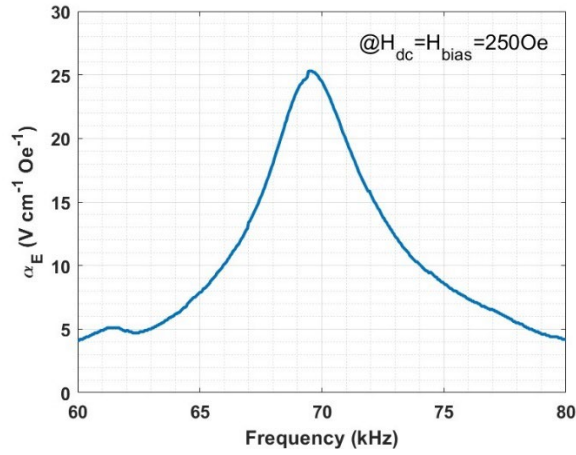


Figure 2.11. ME coefficient measurement in dynamic regime.

### 2.4.3 Prediction of deliverable electric power

Subsequently, we measured the electrical impedance response using the aforementioned impedance analyzer for the ME transducer sample (see Figure 2.12), in the same frequency range as in the ME coefficient measurement, and we can predict the maximal deliverable electric power of the ME transducer, based on the equation 1.3 from the previous chapter, as shown in Figure 2.13.

$$P_{opt} = \frac{(V_{oc} / 2\sqrt{2})^2}{Z_{internal}} \quad 2.9$$

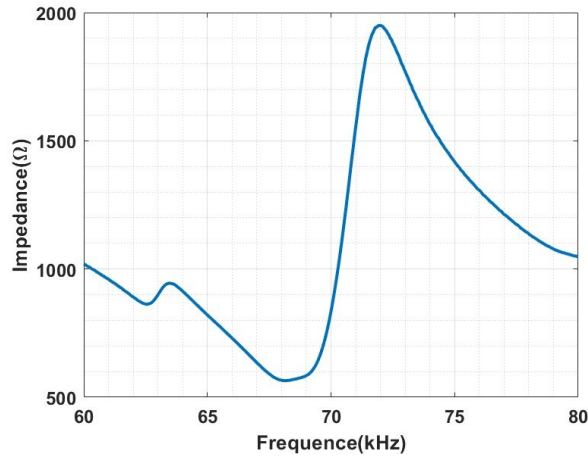


Figure 2.12. Electrical impedance measurement of the ME transducer.

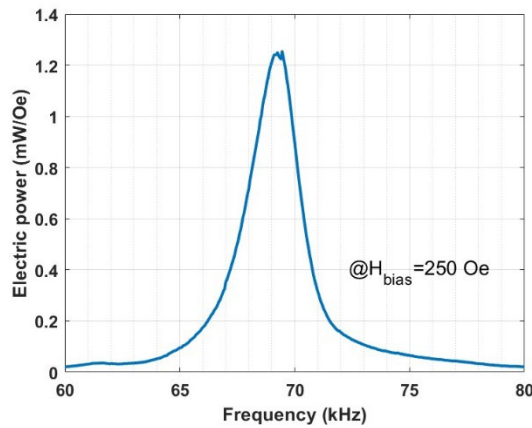


Figure 2.13. Prediction of deliverable electric power.

The above three measurements are crucial for characterizing the ME coefficient in ME materials. Firstly, we determine the magnetic bias needed for optimal magnetoelastic coupling. Next, we identify the ME resonance frequency from the best response in dynamic mode. Finally, by analyzing the electrical impedance, we can predict the optimal deliverable electric power of the measured ME transducer.

## 2.5 Characterization of RF sputtered nickel

As mentioned earlier, in the fabrication process of our studied magnetolectric composite materials, we achieved this by depositing ferromagnetic nickel films on commercially available piezoelectric materials with known properties. We needed to study the properties of the deposited nickel materials as the magnetostrictive phase within the composite materials, in order to further investigate the behavior of these ME materials as ME transducers. In collaboration with the laboratory INSP at Sorbonne University, we used X-ray Diffraction (XRD) to analyze the texture and residual stress in the nickel. Additionally, we employed Vibrating Sample Magnetometer (VSM) to examine its magnetic behavior in the platform MPBT (Plateforme Mesures Physiques à Basses Températures) at Sorbonne University.

## 2.5.1 XRD measurement

X-ray diffraction (XRD) is a precise analytical method used to investigate the crystal structure, phase, and various intrinsic properties of materials, including strain, strain gradients, impurities, and defects. This analysis is carried out by irradiating the sample with X-rays and observing the resulting diffraction patterns. As shown in Figure 2.14, according to Bragg's law, diffraction events are a function of the wavelength  $\lambda$  of the incident radiation and the atomic spacing  $d$  within the sample, ensuring that X-ray scattering within the crystal is coherent and follows the relationship:

$$2d \sin \theta = n\lambda \quad 2.10$$

where  $n$  is the order of diffraction, typically equal to 1 for the first-order diffraction peak.

When the phases of waves from multiple scattering events align, their path length differences are multiples of the interatomic spacing  $d_{hkl}$  of the lattice planes, where  $(hkl)$  denotes the lattice planes. When the angle  $\theta$  satisfies Bragg's law, the scattered waves achieve maximum amplitude, which is evidenced by the prominent Bragg's peaks in the X-ray diffraction pattern. These peaks not only indicate the internal planes of the solid but also allow for the determination of specific crystal structures and chemical compositions by comparing them with established reference data.

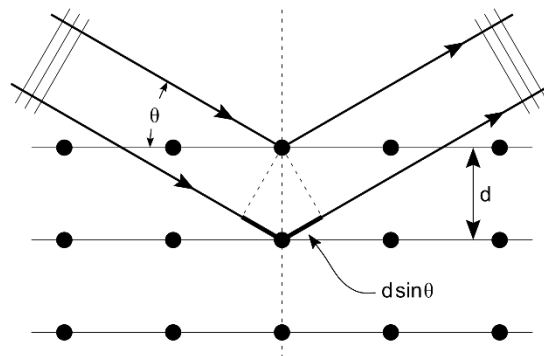


Figure 2.14. Schematic illustration of Bragg's law

The XRD measurement was conducted under the guidance of Dr. Yunlin Zheng from the INSP laboratory, using the XRD diffractometer shown in Figure 2.15. For the measurement, we used a copper (Cu) X-ray tube as the XRD source, which provides two characteristic wavelengths:  $\lambda_{CuK\alpha 1}$  (1.54059 Å) and  $\lambda_{CuK\alpha 2}$  (1.54443 Å). These wavelengths form the so-called K-alpha doublet, with  $\lambda_{CuK\alpha 1}$  being the preferred choice due to its higher emission intensity and shorter wavelength, which helps improve diffraction pattern resolution and measurement accuracy. In contrast,  $\lambda_{CuK\alpha 2}$  has a slightly longer wavelength and typically appears in the diffraction pattern together with  $\lambda_{CuK\alpha 1}$  when a monochromator is not used.

To enhance experimental resolution and accurately determine crystal structures, particularly when high-resolution analysis is required, we used a monochromator in this study to select  $\lambda_{CuK\alpha 1}$  as the primary wavelength for measurement, thus,  $\lambda = \lambda_{CuK\alpha 1}$  for Bragg's law. The monochromator effectively isolates the  $\lambda_{CuK\alpha 1}$  wavelength and eliminates interference from  $\lambda_{CuK\alpha 2}$ , ensuring clear and precise diffraction patterns.



Figure 2.15. Rigaku Smartlab Diffractometer was utilized for the XRD measurements, in the laboratory INSP.

### 2.5.1.a. Texture study using XRD

The  $\theta$ -scan (Theta scan), also known as the  $2\theta/\theta$  scan, was used to determine the crystal structure and interplanar spacing of the nickel films produced by RF sputtering. As shown in Figure 2.16, the X-ray incident angle  $\omega = \theta$  and diffraction angle  $2\theta$  change simultaneously in this scan, allowing the detection of diffraction intensity at various angles according to Bragg's Law. The X-ray source and detector were positioned on opposite sides of the sample, and the X-ray beam was emitted at an angle  $\theta$  towards the sample surface. The detector moved synchronously at an angle  $2\theta$ , relative to the incident beam, to record diffraction intensity at different angles.

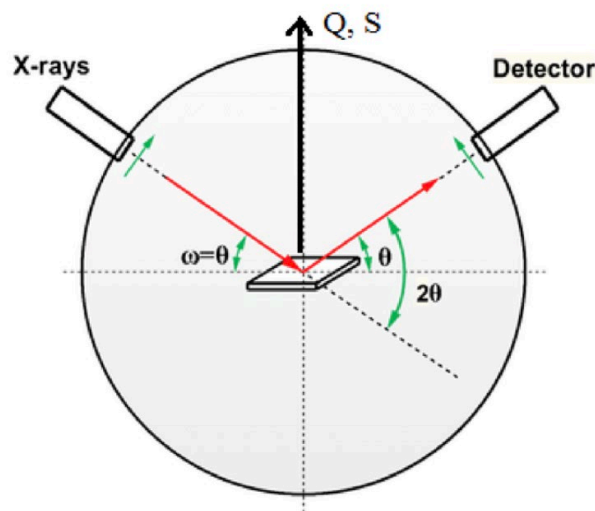


Figure 2.16. Schematic illustration of X-ray diffraction (XRD), with Q represents the scattering vector, and S is the surface normal [61].

In texture studies, the calculation of Texture Coefficient (TC) was pivotal in analyzing the crystal orientation of nickel films produced by RF sputtering, based on the formula as follows [62]:

$$TC_{(hkl)} = \frac{I_{(hkl)}}{I_{0(hkl)}} \left( \frac{1}{n} \sum_{n=1}^n \frac{I_{(hkl)}}{I_{0(hkl)}} \right)^{-1} \quad 2.11$$

Here,  $I_{(hkl)}$  is the XRD intensity measured for a specific lattice plane (hkl), and  $I_{0(hkl)}$  is the intensity of the same plane in a reference material.  $n$  is the number of peaks considered. This formula quantifies the material's crystal orientation by comparing the intensity of a specific plane in the experimental data against that in a non-textured reference.

To apply this formula, we first determined the diffraction peak intensity  $I_{(hkl)}$  for each lattice plane and the corresponding peak intensity  $I_{0(hkl)}$  in a reference sample. Next, we calculated the inverse of the average of these ratios and compared the experimental intensity to this inverse. This method allows us to assess the preferential orientation of specific planes. When  $TC_{(hkl)} > 1$  indicates a stronger orientation preference compared to a non-textured reference, and  $TC_{(hkl)} < 1$  indicates less orientation than reference.

By analyzing the XRD data of RF sputtered nickel films, focusing on characteristic planes like (111), (002), and (022), we were able to quantitatively analyze and compare the texture preferences of different planes. This analysis not only deepened our understanding of the microstructure of nickel films but also provided essential data for further evaluation of the material properties.

The XRD patterns can be used to determine the grain size of nickel (Ni) films. It is crucial to estimate the grain size from the full width at half maximum (FWHM) of the diffraction peaks using the Scherrer equation, defined as:

$$D = \frac{K\lambda}{\beta \cos \theta} \quad 2.12$$

where  $D$  represents the grain size,  $K$  the shape factor (assumed to be 0.9 for spherical grains),  $\beta$  is the corrected FWHM of the diffraction peak, which  $\beta$  is the actual width of the peak minus the instrumental broadening.

### 2.5.1.b. Determination of existence of residual stress

As shown in Figure 2.17, additional degrees of freedom are required to determine in-plane texture and obtain pole figures. These include the tilting angle ( $\psi$ ) and the azimuthal angle ( $\phi$ ).

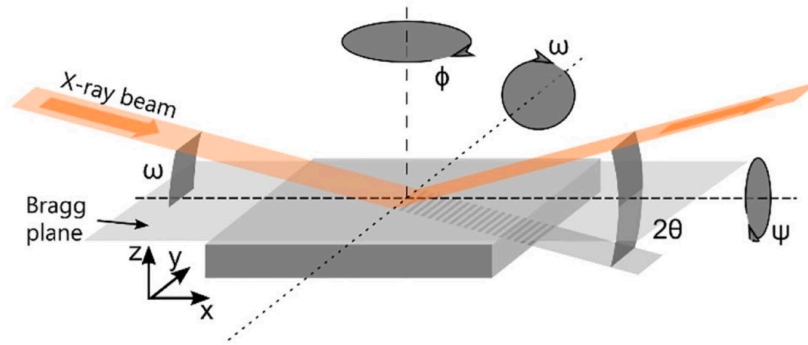


Figure 2.17. Schematic representation of the angles used in XRD measurements, illustrating the notations for the four key angles, which are essential for controlling sample orientation and diffraction measurements [63].

In grazing incidence X-ray diffraction (GIXRD), the  $\phi$ -scan (Phi scan) is used to analyze the in-plane crystallographic orientation and texture of materials. In the  $\phi$ -scan, the incident angle  $\omega = 0.5^\circ$  and diffraction angle ( $2\theta$ ) remain constant, with the X-ray source and detector fixed in position. As shown in Figure 2.18, the X-ray beam is directed at a constant angle toward the sample, while the detector records the diffraction signal from different directions as the sample is rotated azimuthally  $\phi$ . Additionally, in our measurement setup, the sample remains stationary while the detector rotates horizontally around the sample, gathering diffraction data at different azimuthal angles. In this configuration, the detector rotates over a range of  $0^\circ$  to  $360^\circ$  around the sample, collecting diffraction intensities at different orientations. Through  $\phi$ -scan, the in-plane crystallographic orientation and anisotropy of the material can be quantitatively analyzed, providing detailed insights into texture and stress.

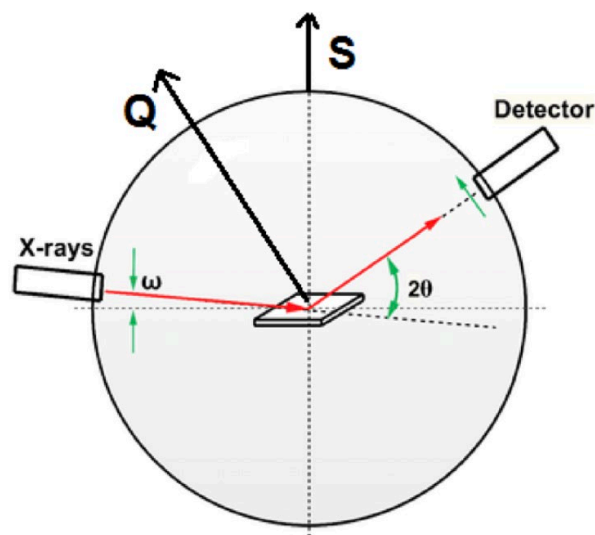


Figure 2.18. Schematic illustration of grazing incidence X-ray diffraction (GIXRD), with  $Q$  represents the scattering vector, and  $S$  is the surface normal [61].

As detailed in the reference [64], Phi scans are used to measure residual stress within the film by determining changes in lattice strain. During the phi scan, the sample is tilted at different angles ( $\phi$ ) while maintaining a fixed  $\theta$ . This method examines the change in the interplanar spacing ( $d_{hkl}$ ) as the sample is rotated around its normal, helping identify unidirectional internal stresses.

We decided to employ XRD technique to verify the existence of residual stress through lattice strain measurement, due to its suitability for crystalline materials and its non-destructive measurement capabilities. The XRD enables the accurate measurement of interplanar distances  $d_{hkl}$ , where relative changes reflect unidirectional internal material strains  $S$ . The strain  $S$  in the lattice planes indexed by (hkl) can be computed using the formula:

$$S = \frac{d_{hkl} - d_{hkl,0}}{d_{hkl,0}} \quad 2.13$$

here,  $d_{hkl,0}$  represents the interplanar distance without stress, and  $d_{hkl}$  is the distance when the lattice is under stress. This method allows for the quantification of residual stresses within the film by correlating the variations in crystal structure with measured strains.

### 2.5.2 Magnetization measurement

We employed a Vibrating Sample Magnetometer (VSM) to characterize the magnetization properties of our magnetostrictive nickel materials. We chose this technique due to its precision and efficiency in analyzing both ferromagnetic and paramagnetic materials. During the vibrating sample magnetometry process, the sample is mounted on a vibrator and exposed to a static magnetic field  $H = H_{dc}$ . As the sample vibrates, it induces a voltage in the surrounding coils, which directly correlates with the magnetization strength of the sample. The VSM is also equipped with a temperature control system, allowing us to conduct magnetic measurements at various environmental temperatures and assess the impact of temperature on the sample's magnetic properties.

The magnetization  $M$  was precisely measured as a function of static magnetic field  $H$  ranging from 2 kOe down to -2 kOe, with precise adjustments at a step of 2 Oe. It is worth noting that, before the measurement, the samples were precisely cut into a dimension less than  $5 \times 5 \text{ mm}^2$  to fit the VSM sample holder. And before installing each sample, an oscillating field from 10 kOe down to zero was applied to reduce the residual magnetic field in the coil to less than 5 Oe.

By using a  $\text{Yb}_2\text{O}_3$  reference, we obtained the field error for the applied magnetic field  $H$  as shown in the Figure 2.19. Therefore, when our measurements focus on the range of -1000 to 1000 Oe, we should adjust the results of the increasing applied magnetic field  $H$  by -12 Oe and the decreasing magnetic field  $H$  by +21 Oe in post-processing. This adjustment compensates for the impact field error on the results, yielding an accurate coercive magnetic field determination.

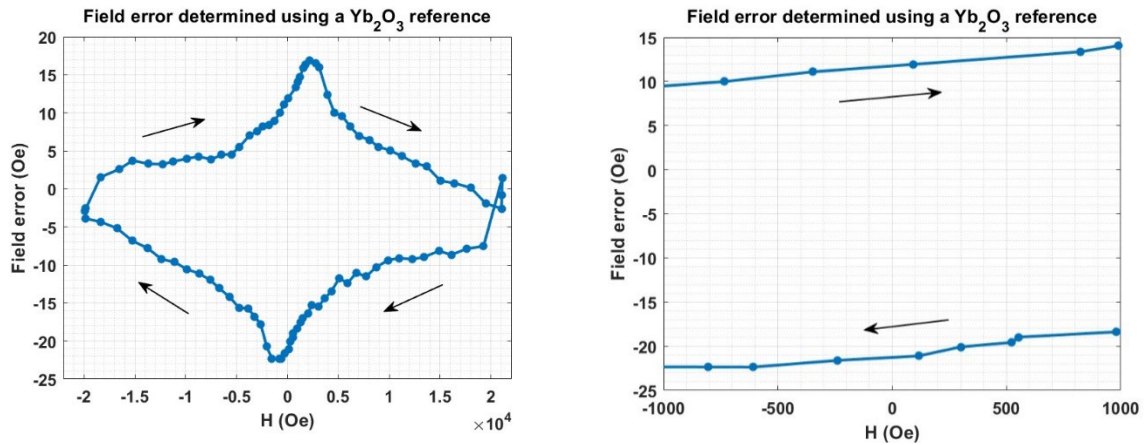


Figure 2.19. Field error determination for VSM measurement using a  $\text{Yb}_2\text{O}_3$  Reference.

## 2.6 Initial study for Ni/LiNbO<sub>3</sub>/Ni transducers

During this thesis work, we focused on Ni/LiNbO<sub>3</sub>/Ni ME transducers made by RF sputtering. Nickel, a commonly used magnetostrictive material in self-biased ME materials, and lithium niobate (LiNbO<sub>3</sub>), discussed in the previous chapter as suitable for biomedical implant applications, were chosen. The two types of LiNbO<sub>3</sub>, namely 36° Y-cut and 163° Y-cut, displayed figures of merit similar to the commonly used PZT piezoelectric ceramics. Thus, we selected firstly four equal-thickness (100  $\mu\text{m}$ ) LiNbO<sub>3</sub> piezoelectric films as substrates: two 36° Y-cut substrate of 30 mm long and two 163° Y-cut substrate of 10 mm long. We deposited nickel films of 2 different sets of thicknesses on both sides of these different cuts of piezoelectric substrates, resulting in four ME transducer samples. The specific dimension configurations of these samples are shown in Table 2.2. It is worth noting that, to facilitate the measurement of the ME output voltage for these four samples, we used conductive epoxy to bond gold-plated leads to the nickel films on both surfaces, establishing electrical contact during ME measurements, as shown in Figure 2.1.

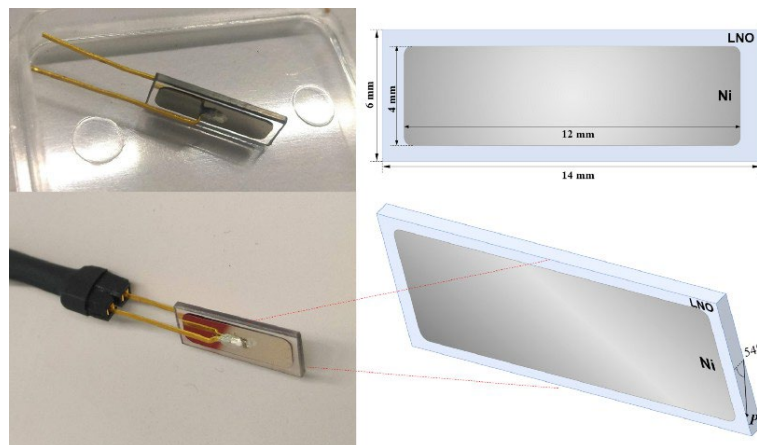


Figure 2.1. A trilayer Ni/LiNbO<sub>3</sub>/Ni ME transducer fabricated using RF sputtering, with gold-plated leads bonded to the nickel films on both surfaces using conductive epoxy for electrical contact.

Table 2.2. Configuration of the first set of ME transducer samples for initial study.

Sample	Ni thickness on both side ( $\mu\text{m}$ )	LiNbO <sub>3</sub> substrates
1	10/10	36° Y-cut (30mm x 5mm x 100 $\mu\text{m}$ )
2	35/32	36° Y-cut (30mm x 5mm x 100 $\mu\text{m}$ )
3	10/10	163° Y-cut (10mm x 5mm x 100 $\mu\text{m}$ )
4	35/32	163° Y-cut (10mm x 5mm x 100 $\mu\text{m}$ )

According to equation 2.5, the first longitudinal resonance frequency of ME materials is inversely proportional to their length. As shown in Table 2.2, we used two different lengths (30 mm and 10 mm) to study the impact of dimensions on the resonance frequency. In practical applications, especially for biomedical implants, a lower dynamic excitation magnetic field frequency reduces the power requirements for generating the magnetic field and minimizes environmental interference. Additionally, lower frequencies are more likely to comply with safety standards for human exposure to magnetic fields, making them more suitable for biomedical implantable applications.

Furthermore, we selected two different nickel thicknesses because the magnetostrictive volume fraction is a key parameter affecting the performance of ME materials. By varying the nickel thickness while keeping the LiNbO<sub>3</sub> thickness constant, we aimed to investigate whether different LiNbO<sub>3</sub> cuts with increased nickel thickness would result in enhanced ME performance. Notably, there are slight differences in the nickel film thickness between samples 2 and 4 due to variations in the deposition times.

Initial measurements of these four Ni/LiNbO<sub>3</sub>/Ni ME transducers were performed along their length, using the previously mentioned ME measurement method in the quasi-static regime. When setting a conventional frequency of 1 kHz for  $H_{ac}$ , the output voltage measured on the oscilloscope was very weak, approximately 5 mV, and the output voltage measured around ME resonance frequency is in the scale of  $10^{-1}$  V. Therefore, we decided to perform ME measurements in the dynamic regime to determine each sample's resonance frequency before conducting quasi-static regime measurements, and after setting this frequency as the constant frequency parameter for  $H_{ac}$ .

The ME coefficient measurement results of samples 2 and 4, which have the same thickness of Ni films but different piezoelectric cuts, in the quasi-static regime are shown in Figure 2.20. We observed that their ME coefficient behaviors at zero  $H_{dc}$  are different. One reaches its maximum value, while the other reaches its minimum value.

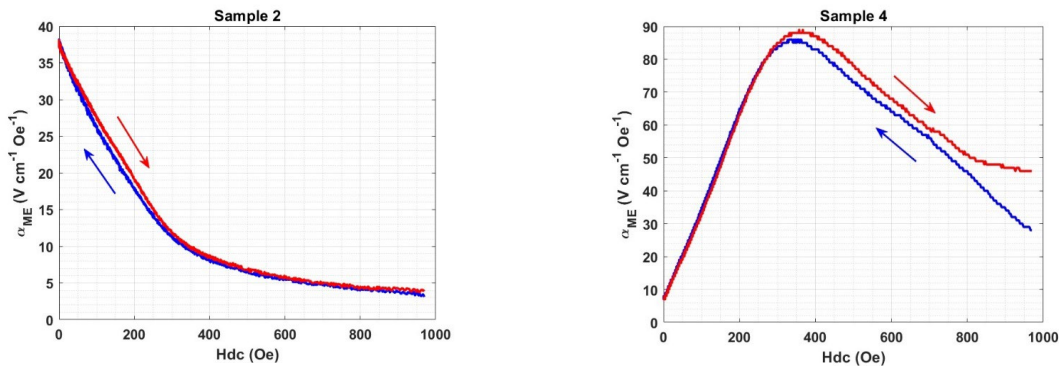


Figure 2.20. ME coefficient measurements for the sample 2 and 4 in quasi-static regime, with a unidirectional static magnetic field  $H_{dc}$ .

Since the ME behavior in the quasi-static regime is strongly correlated with the magnetic behavior of the magnetostrictive material, we made other adjustments to the ME measurements in the quasi-static regime, we refined the measurement of the ME coefficient as it varies also with negative  $H_{dc}$ . We did this by sweeping  $H_{dc}$  from  $-H_{dc,max}$  to  $H_{dc,max}$  and then back from  $H_{dc,max}$  to  $-H_{dc,max}$ . We altered the direction of  $H_{dc}$  by rearranging the permanent magnets when  $H_{dc}$  was approximately zero (maximum distance between the permanent magnets and the ME transducer). It is worth noting that, with these above adjustments, the subsequent quasi-static measurement results enable us to directly derive the optimal ME coefficient of our measured ME transducer sample. Therefore, the upcoming ME measurements will focus only on the results obtained from these quasi-static measurements.

After adjusting the measurement methods, the measurements obtained for these four ME samples, as shown in Figure 2.21, reveal that the two samples based on the  $36^\circ$  Y-cut, samples 1 and 2 exhibited self-biased ME behavior, meaning their ME coefficient at zero  $H_{dc}$  was remarkable compared to the maximum value in the ME curve. In contrast, the other two samples based on the  $163^\circ$  Y-cut, sample 3 and 4 showed typical quasi-static ME behavior, similar to general ME materials.

Given the known strong correlation between magnetoelectric (ME) behavior and the magnetic behavior of magnetostrictive materials, we proceeded to analyze the nickel material in these four samples. As shown in Figure 2.22, revealed that the texture of the nickel in these four samples differed from that of the referenced polycrystalline nickel target, with variations in nickel thickness and different single-crystal cuts resulting in distinct XRD patterns. Since the nickel films produced by RF sputtering are expected to be polycrystalline and not exhibit the pronounced single-crystal characteristics seen in the  $163^\circ$  Y-cuts, and the thicknesses of the nickel films measured are within the penetrable range for XRD, we can assume that the variations in the XRD patterns of the nickel films are due to the influence of the  $\text{LiNbO}_3$  single-crystal substrates.

We continued our measurements on a nickel film isolated from sample 4 and re-measured it. Since the piezoelectric  $\text{LiNbO}_3$  material is less resilient than nickel, we applied stress to crush the sample 4, isolating a single nickel layer. The isolated nickel layer was then cleaned and examined under a microscope to ensure no residual  $\text{LiNbO}_3$  fragments remained. This time, as shown in Figure 2.23, the results compared with our referenced polycrystalline nickel target showed that the nickel deposited on these samples was also polycrystalline, with all the texture coefficients approaching 1.

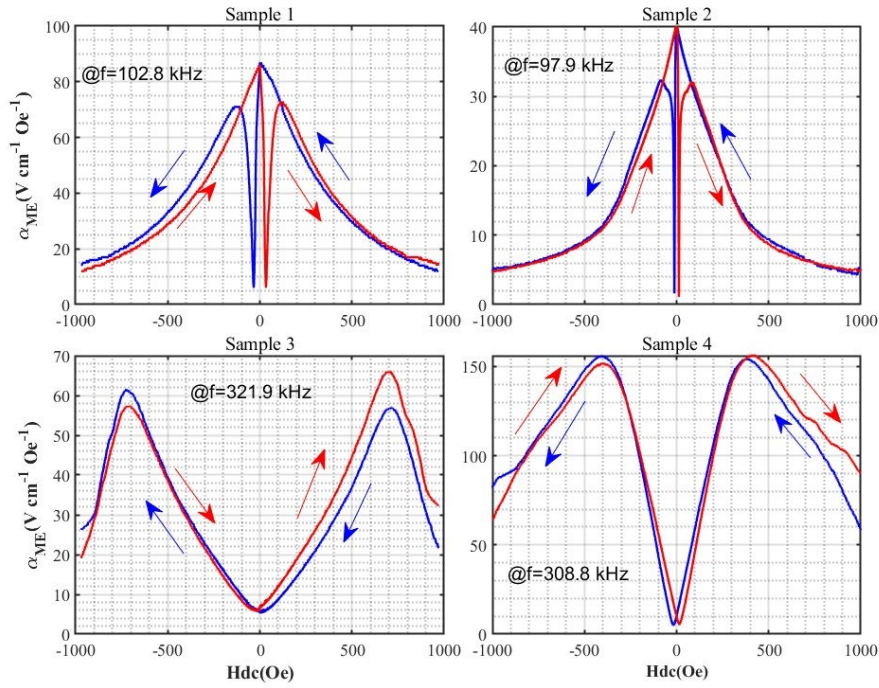


Figure 2.21. ME coefficient measurement in quasi-static regime for the first set of ME transducer samples.

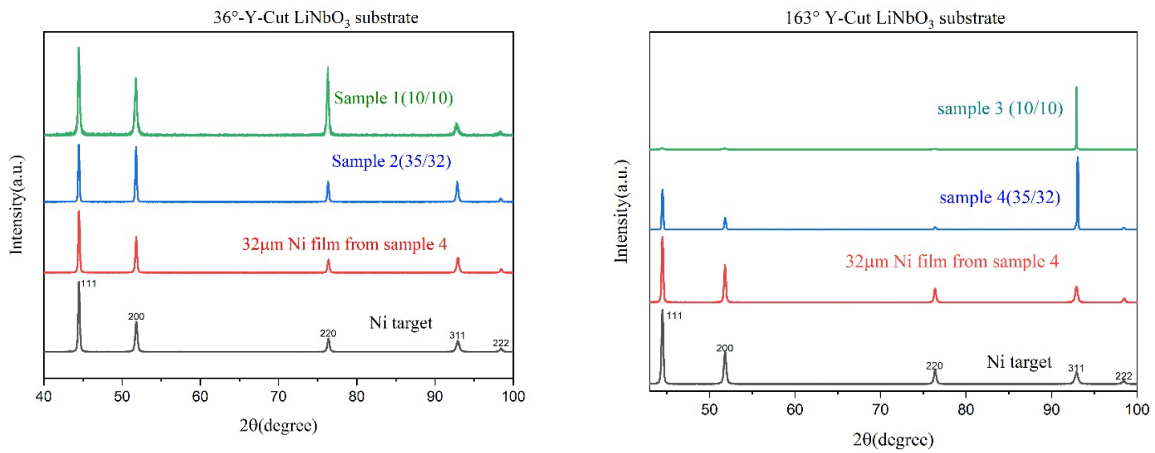


Figure 2.22. XRD patterns of the first set of ME transducer samples.

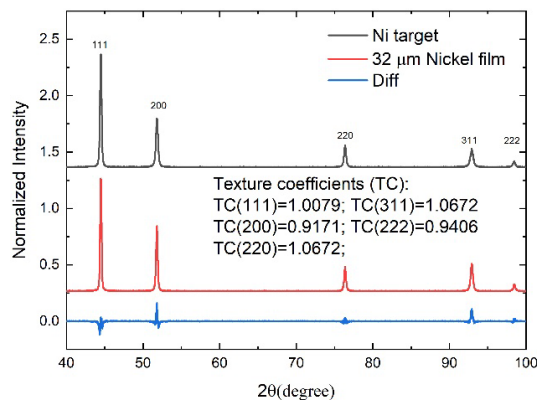


Figure 2.23. Comparison between XRD patterns of one Nickel film isolated from sample 4 and of referenced Nickel target, texture coefficients have been calculated and include inside.

As shown in Figure 2.24, we conducted VSM measurements under the trilayer structure of these four samples, along their length direction. We can observe that their measurements were distinctly different, especially between the samples with different cuts of  $\text{LiNbO}_3$ . This indicates that the differences in the ME behavior of these samples are related to their magnetic behavior of nickel on different  $\text{LiNbO}_3$  cuts; preliminarily, we can say that the magnetic behavior of samples 1 and 2, characterized by high remanence and low saturation magnetic field, is key to their self-biased ME behavior.

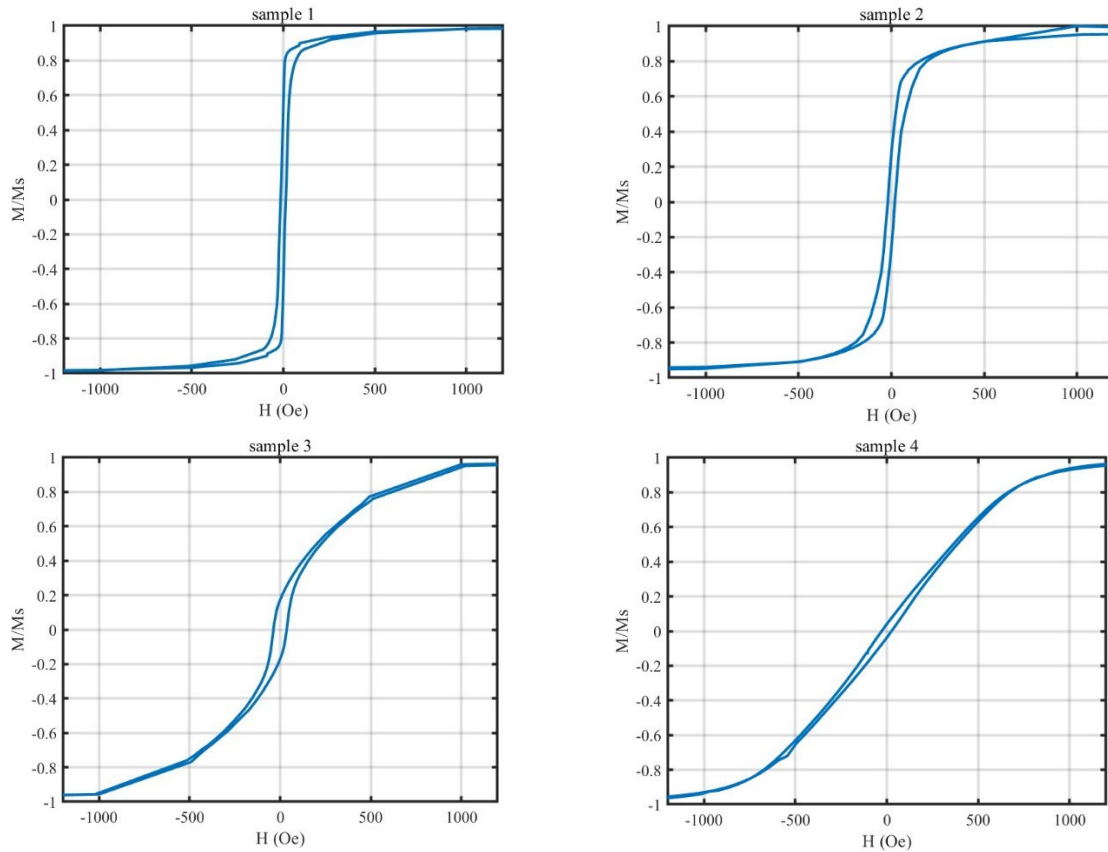


Figure 2.24. Magnetic curves of the first set ME samples along their 2 in-plane direction.

Subsequently, we measured their other in-plane direction along the width for samples 1 and 2. As shown in Figure 2.25, we observed that within the same sample, its magnetic behavior is anisotropic in two in-plane directions. And the magnetic behavior of these two samples along with the width direction is similar to samples 3 and 4. Although we did not perform supplemental VSM measurements along their width for samples 3 and 4, we could predict their in-plane magnetic behaviors are likely anisotropic.

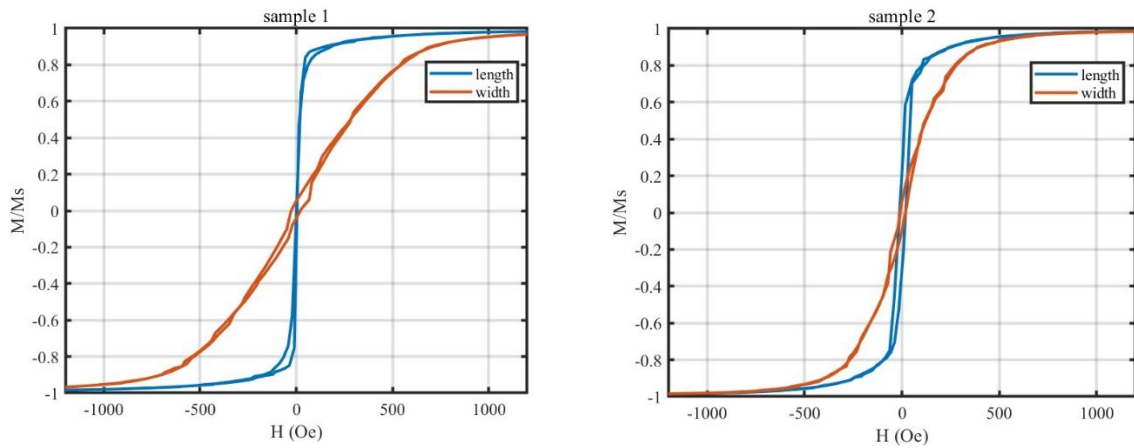


Figure 2.25. In-plane magnetic behaviors of samples 1 and 2.

As shown in Figure 2.26, we isolated a single nickel layer from sample 2 and conducted magnetization measurements along its two in-plane directions. The in-plane magnetic behaviors are much more isotropic compared to those in the trilayer structure, and the curves are between the two results measured in the trilayer configuration. As the magnetoelectric model detailed in the previous chapter, the magnetic behavior of ferromagnetic materials is a function of static magnetic field and can also be influenced by stress applied to or existing in the material. We can assume that the anisotropic characteristics of our Ni/LiNbO<sub>3</sub>/Ni samples are due to two opposite residual stresses occurring at the contact surface between Ni and the LiNbO<sub>3</sub> substrate during the RF sputtering process, and applied on Ni films after the process when Ni stays in trilayer ME transducer.

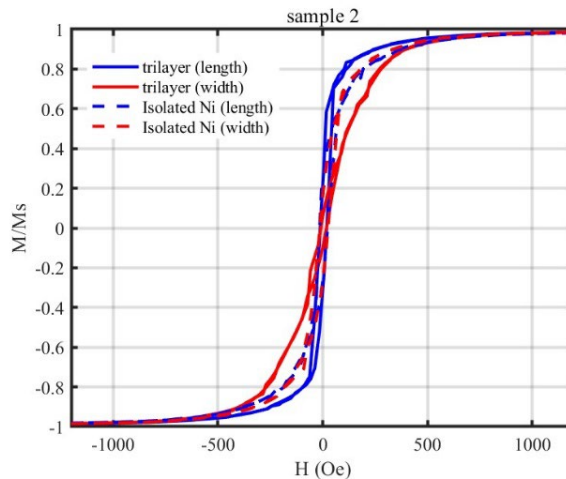


Figure 2.26. Magnetic behaviors of nickel films in trilayer and of one isolated film for the sample 2.

To support the assumption, the sputtering process involves the ejection of atoms from a target material by the bombardment of ions generated by a plasma, leading to the formation of vapor that condenses onto the substrate surface to form a thin-film layer. During the RF sputtering process, the exchange of energy between plasma ions and the substrate surface generates heat during the growth of nickel on the substrate, which can lead to different thermal expansions of Ni and LiNbO<sub>3</sub> materials. This leads to the generation of residual stresses on their contact surface when the nickel films and piezoelectric substrate cool down to room temperature after

sputtering process [65]. The origin of magnetic anisotropy primarily lies in the mismatch of coefficients of thermal expansion (CTEs) of Ni and LiNbO<sub>3</sub>, as illustrated in Table 2.3, and the residual stresses associated with thermal expansion effects, described by:

$$\sigma_{r,ii} = c_e(\alpha_s - \alpha_f)\Delta T \quad 2.14$$

Here,  $\alpha_s$  and  $\alpha_f$  respectively represent the CTEs of LiNbO<sub>3</sub> substrate and of Ni films,  $\Delta T$  is the difference of temperature between the ambient temperature and the temperature of the growth of Ni during the sputtering deposition process (after RF sputtering,  $\Delta T < 0$ ), and  $c_e$  is the biaxial longitudinal stiffness coefficient in the stiffness tensor of the Ni films, equal to the Young's Modulus  $E_Y$ . Our focus will be on the in-plane biaxial (residual) stress within the Ni films, i.e.,  $\sigma_{r,xx}$  and  $\sigma_{r,yy}$  for the two in-plane directions of the LiNbO<sub>3</sub> substrate: parallel to the X axis and perpendicular to the X axis, respectively. Since the coefficient of thermal expansion (CTE) of the LiNbO<sub>3</sub> substrate in the X axis direction is greater than that of Nickel, a negative (compressive) residual stress generated after RF sputtering. Conversely, the CTE of the LiNbO<sub>3</sub> substrate in the direction perpendicular to the X axis, being smaller than that of Nickel, leads to a positive (tensile) residual stress after RF sputtering.

As shown in Figure 2.24, the magnetic behavior of the nickel films on the two samples based on the 36° Y-cut LiNbO<sub>3</sub> along their length direction is as if subjected to a negative stress, so we can determine that their X axis of the piezoelectric substrate is along their length direction. Meanwhile, the magnetic behavior of the nickel films in the two samples based on the 163° Y-cut LiNbO<sub>3</sub> shows that they are subjected to a positive stress, indicating that their X axis is along their width direction.

Table 2.3. CTEs of materials in ME transducers in the direction parallel and perpendicular to the X axis in the coordinate system of LiNbO<sub>3</sub>.

	CTE (parallel to X-axis) (10 <sup>-6</sup> K <sup>-1</sup> )	CTE (perp to X-axis) (10 <sup>-6</sup> K <sup>-1</sup> )
Nickel	13.4	13.4
36° Y-cut LiNbO <sub>3</sub>	15.4	10.23
163° Y-cut LiNbO <sub>3</sub>	15.4	8.18

As shown in Figure 2.27, by using VSM to measure the magnetization of sample 1 at different temperatures, we observed that the changes in temperature along the length of sample 1 do not significantly alter the magnetic behavior of the nickel films, only slightly changes in magnetization saturation and magnetic coercive values under different temperatures. Conversely, by examining the magnetic curves of sample 1 along its width at different temperatures, we observed that a decrease in temperature ( $\Delta T < 0$ ) leads to a later saturation in the magnetic curves compared to those at higher temperatures, similar to the changes seen in a 35 nm thick evaporated nickel film deposited on a LiNbO<sub>3</sub> substrate, under positive strain (equivalent to a positive stress) (see Figure 2.28) [66], [67], [68]. Therefore, the changes in magnetization with temperature preliminarily confirm our hypothesis.

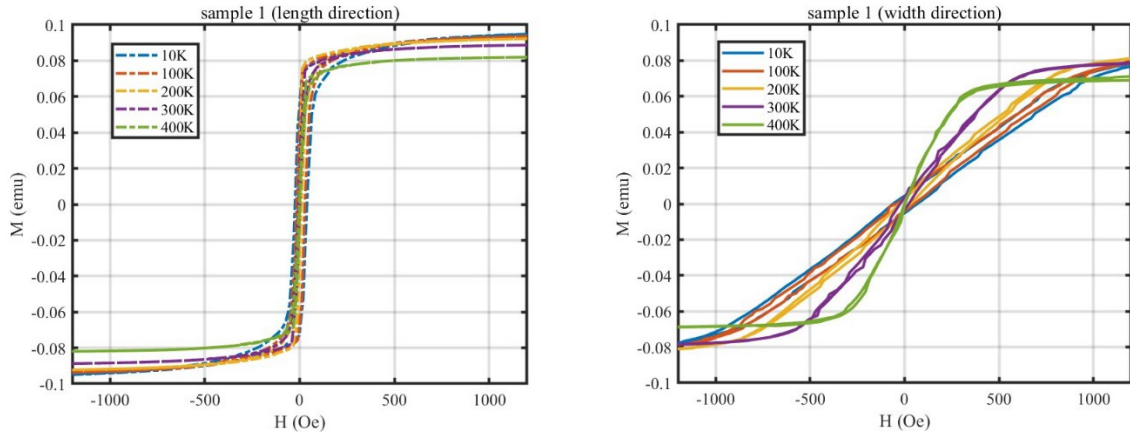


Figure 2.27. Magnetization measurements under different temperature for sample 1 in two in-plane directions.

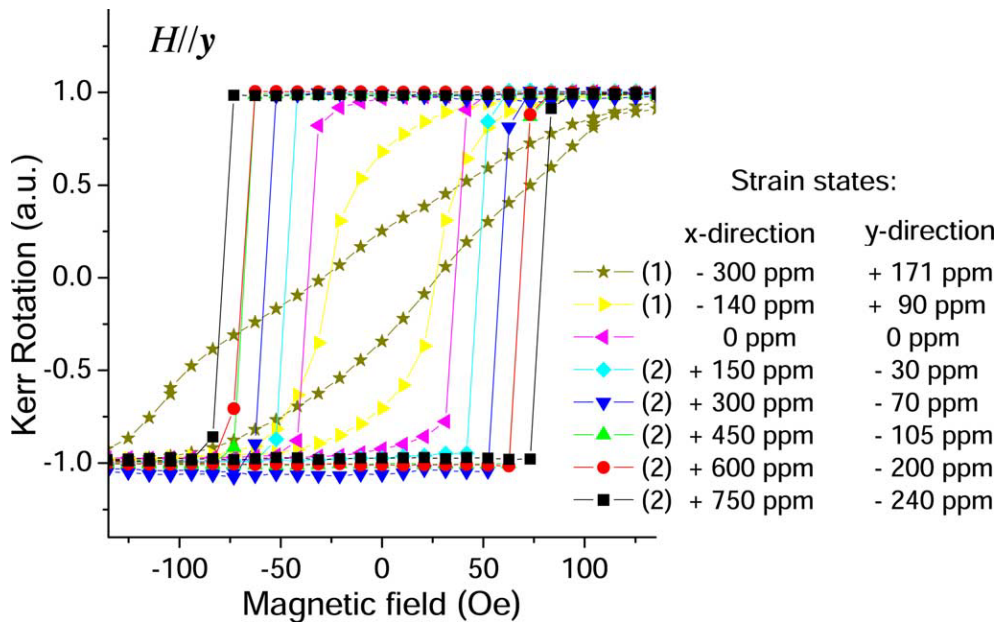


Figure 2.28.  $M$ - $H$  curves of a 35 nm e-beam evaporated Ni thin film on  $\text{LiNbO}_3$  substrate, under different applied strains [66].

Subsequently, we conducted precise in-plane XRD measurements (grazing incident XRD phi-scan) on sample 2 and a reference polycrystalline nickel target, focusing on the (311) planes in two in-plane directions, as shown in Figure 2.29. The three (311) peaks in this figure were fitted using the Pseudo-Voigt function. According to equation 2.10, a larger peak value indicates smaller interplanar distances. Thus, it is shown that the nickel films along the length direction are subject to a compressive stress compared to the reference nickel target, resulting in relatively smaller  $d_{311}$  distances. Conversely, in the width direction, the  $d_{311}$  is larger relative to the nickel target, indicating the effect of a tensile stress.

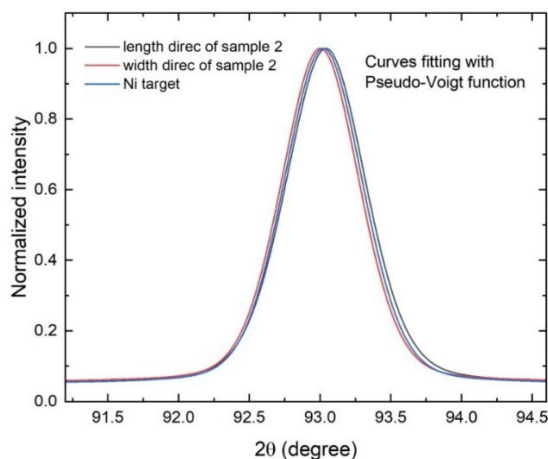


Figure 2.29. In-plane XRD measurements for sample 2 and the Ni target in two in-plane directions.

## 2.7 Full study for 36° Y-cut and 163° Y-cut based ME transducers

After the previous study of samples 1-4, based on the ME coefficient measurements conducted along their length direction in the quasi-static regime, we observed self-biased ME behavior in the two samples containing 36° Y-cut. Subsequently, anisotropic magnetic behavior was observed in these samples through magnetization measurements using VSM, and measurements at different temperatures using VSM tentatively confirmed that the source of the in-plane anisotropy could be residual stress formed during cooling back to room temperature after RF sputtering. As indicated in Table 2.3, samples based on 163° Y-cut LiNbO<sub>3</sub> could also generate negative residual stress along their crystallographic X axis and should exhibit self-biased ME behavior in this direction. To verify these initial results, we decided to carry out a new series of measurements, organizing the different characterizations (X-ray, magnetic and electrical along length and width of the samples) to confirm our results.

Therefore, we continued using two 36° Y-cut and 163° Y-cut LiNbO<sub>3</sub> substrates, explicitly requiring that the X axis of the LiNbO<sub>3</sub> be oriented in this direction (along the length of the sample) prior to purchase. We confirmed the crystallographic X axis through in-plane XRD phi-scan on the (0 $\bar{1}$ 2) lattice plane for these two LiNbO<sub>3</sub> substrates, with each LiNbO<sub>3</sub> substrate's crystallographic X axis parallel to the X' (length) direction of the device, as shown in Figure 2.30. In compliance with the IEEE standard [55], these cuts are more precisely denominated as (YXI)36° and (YXI)163°, respectively. Finally, we fabricate two ME transducer samples as detailed in Table 2.4, for the full study of ME behaviors of Ni/LiNbO<sub>3</sub>/Ni transducer within the 36° and 163° Y-cuts monocrystalline piezoelectric cuts.

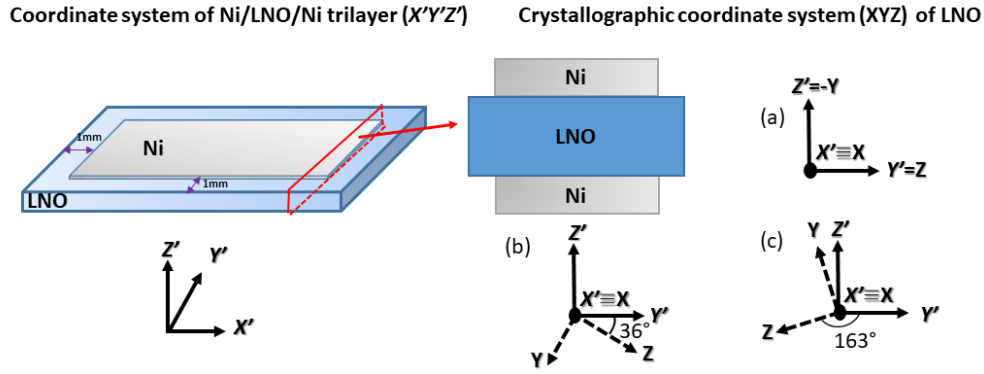


Figure 2.30. Illustration of trilayer ME transducer with two different cuts:  $36^\circ$  Y cut and the  $163^\circ$  Y cut.

Table 2.4. Configuration of the second set of ME transducer samples for full study.

Sample	Ni thickness on both side ( $\mu\text{m}$ )	LiNbO <sub>3</sub> substrates
5	11/10.2	$36^\circ$ Y-cut (20mm x 5mm x 100 $\mu\text{m}$ )
6	11/10.2	$163^\circ$ Y-cut (10mm x 5mm x 100 $\mu\text{m}$ )

The Figure 2.31 illustrate two magnetic excitation configurations used in L-T mode operating mode. Each ME sample was excited by an external magnetic field applied longitudinally (L mode) in the  $X'$  or  $Y'$  in-plane direction, and the electric output voltage was polarized transversely (T mode) in the  $Z'$  direction. Since using conductive epoxy to bond gold-plated leads as our electrical contact during measurements was inconvenient for measuring our ME samples in two different in-plane directions, we modified our setup in subsequent measurements. As shown in Figure 2.32, ME samples were mounted in a sample holder composed of plastic plates printed by a 3D printer and two separate conductive wires. The plastic plates were used to align the length or width direction of ME samples with the applied magnetic field, and the wires were in electrical contact with Ni films on both sides of the ME sample. Since our integration method involves fixing the sample by means of conductive wires that contact the sample like clips, each integration may result in different contact positions and different forces being applied to the sample thickness. As a result, the measurement results may vary slightly. In such cases we select the best result from several measurements of the same sample.

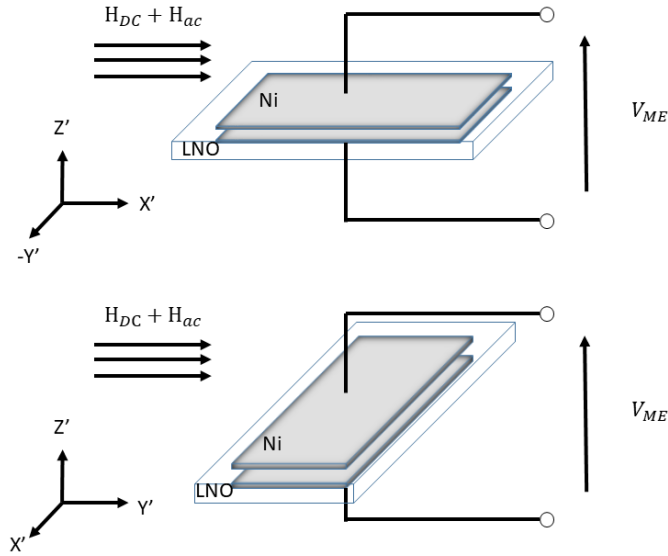


Figure 2.31. Illustration of Ni/ LiNbO<sub>3</sub>/Ni trilayer function in LT mode



Figure 2.32. Illustration of using a sample holder to mount ME samples during measurements.

As shown in Figure 2.33, the ME coefficient measurement for samples 5 and 6 illustrates that each measurement has a maximum ME response at the optimal bias magnetic field  $H_{bias}$ . We notice that  $H_{bias}$  values in the X' direction are much lower than those in the Y' direction: for the sample 5,  $H_{bias}$  is equal to  $\pm 37$  Oe and  $\pm 149$  Oe in the X' and Y' directions, respectively. For the sample 6,  $H_{bias}$  is equal to  $\pm 106$  Oe and  $\pm 238$  Oe in the X' and Y' directions, respectively.

Our main finding is the self-biased behavior with magnetic excitation applied along the X' direction. Interestingly, at zero  $H_{dc}$ , ME coefficient  $\alpha_E$  is at 94.20% of its maximum value for the sample 5 grown on the (YXl) 36° LiNbO<sub>3</sub> substrate and at 80% for another sample 6 grown on the (YXl) 163° LiNbO<sub>3</sub> substrate. Moreover, the self-biased behavior disappears in the Y' direction, where the  $\alpha_E$  values drop to less than 40% of their maximum. Therefore, we could conclude that the self-biased ME behaviors occur in the X' direction (parallel to X axis of LiNbO<sub>3</sub> substrate) for these two ME transducer samples.

In addition, we can confirm our hypothesis that the X axis of the previously studied samples 3 and 4 is along their width direction by comparing their ME behaviors along their length with the ME coefficient curve in Figure 2.33d. The 163° Y-cut LiNbO<sub>3</sub> can be denoted precisely as (YXw) 163° LiNbO<sub>3</sub>. In the following studies about the Ni/LiNbO<sub>3</sub>/Ni ME transducers, we should validate the X-axis first for the monocrystalline LiNbO<sub>3</sub> substrate.

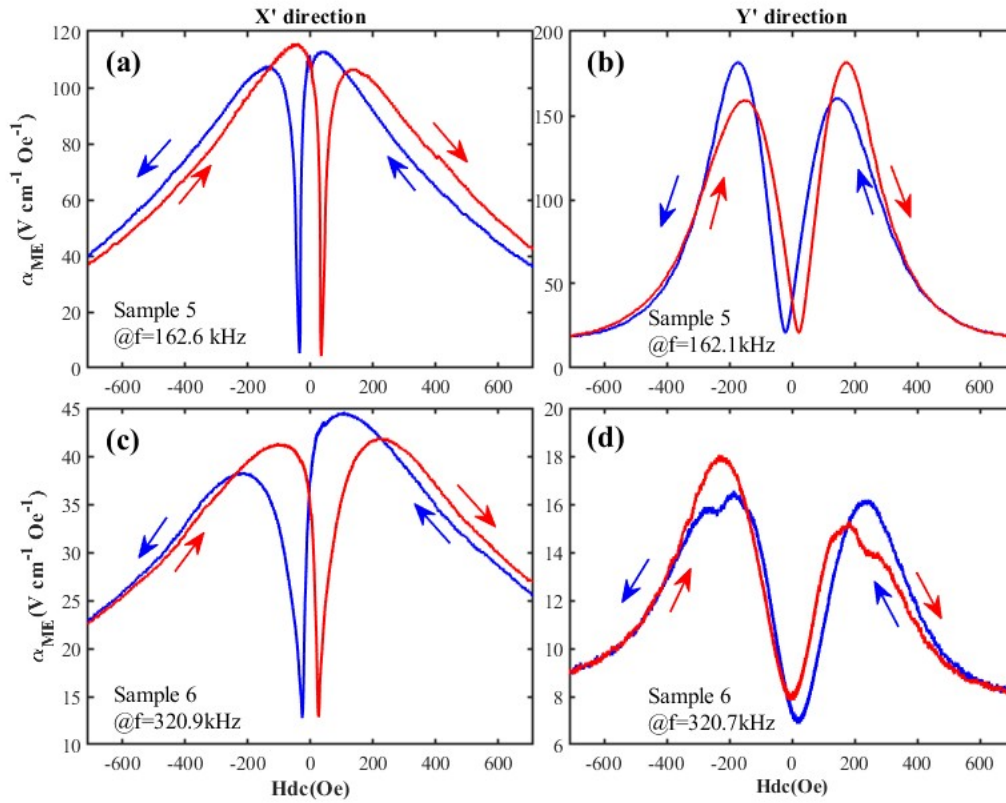


Figure 2.33. ME coefficient characterization of two ME Ni/LiNbO<sub>3</sub>/Ni samples with different piezoelectric cuts.

As in the previous study, our next step involves conducting an in-depth examination of the ferromagnetic properties of the nickel films deposited on the LiNbO<sub>3</sub> substrate via RF sputtering. To validate and confirm the correlation between the self-biased ME behavior and the magnetic behavior of Ni films under a negative stress, as well as the existence of residual stress.

### 2.7.1.a. Nickel films texture

As shown in Figure 2.34, the XRD patterns of the deposited nickel film on the two ME transducer samples are compared to the pattern of the reference polycrystalline nickel target. It can be observed that each deposited nickel film on the lithium niobate substrate exhibits a similar behavior to that of the polycrystalline reference. Additionally, the FWHM of all XRD peaks for sample 6 is greater than that of sample 5. This illustrates that the lattice size of the Ni films growth on the (YX1) 163° LiNbO<sub>3</sub> is smaller than that formed on the (YX1) 36° LiNbO<sub>3</sub>.

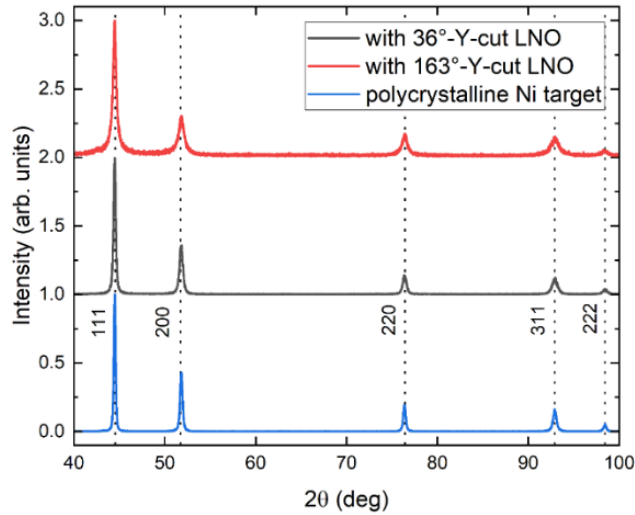


Figure 2.34. XRD patterns of the Ni films deposited using RF sputtering.

### 2.7.1.b. Magnetization measurement

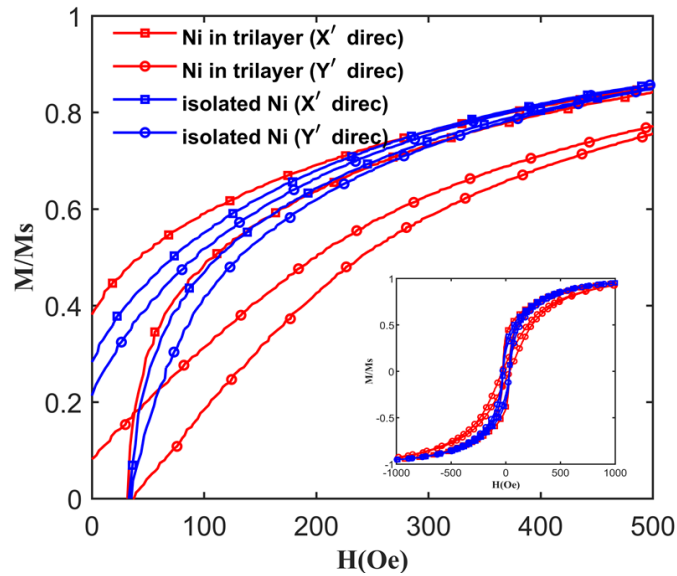


Figure 2.35. Magnetization measurement of the nickel material in the Ni/(YXI)163° LiNbO<sub>3</sub>/Ni sample.

As shown in Figure 2.35, we obtained magnetic hysteresis loops using VSM. An anisotropic magnetization behavior is observed in trilayer samples, with higher remanence and lower saturation fields in the X' direction compared to the Y' direction. Interestingly, the anisotropy is significantly reduced in freestanding films, indicating the substantial impact of residual stress imposed by the substrate. This leads us to deduce that the LiNbO<sub>3</sub> substrates induce significant anisotropic thermal residual stress and subsequent magnetic anisotropy.

We can also verify how the magnetic behavior of nickel in a trilayer structure is influenced by temperature variations through a comparative analysis of magnetization measurements at different temperatures. As shown in Figure 2.36, we report the magnetization cycles measured along the X' and Y' directions under different temperatures. In the X' direction, we observed high remanences are detected at all examined temperatures, as the saturated fields of  $M-H$

curves measured in the X' direction are close to 0 Oe, making it challenging to directly compare the differences in their magnetic behaviors in the X' direction. In the Y' direction, as compared to, the  $M-H$  curve at temperature (200 K) lower than room temperature (300 K), aligns with the curves under positive residual thermal stress related to cooling condition, while the  $M-H$  curve at temperatures (400 K) higher than 300 K, aligns with the curves under negative stress related to heating condition.

As shown in Figure 2.36, when we compared the magnetic curves of sample 5 in X' and Y' directions at 400K. This implies that residual stress is alleviated upon heating, leading to a more isotropic magnetic behavior at 400 K. Such behavior is also consistent with that seen in Figure 2.35 and Figure 2.36, where the magnetization cycle of freestanding films (blue curves) at 300 K are markedly similar to that in clamped trilayers structure at 400 K. Therefore, we can indirectly estimate that when we fabricated our ME transducer through RF sputtering, it involved an approximate temperature difference of 100 K. With stiffness coefficient  $c_{ii} = E_Y = 207$  GPa. We have a magnitude of residual stress,  $\sigma$ , will be in the order of 50 MPa, with opposite signs in the X' and Y' directions.

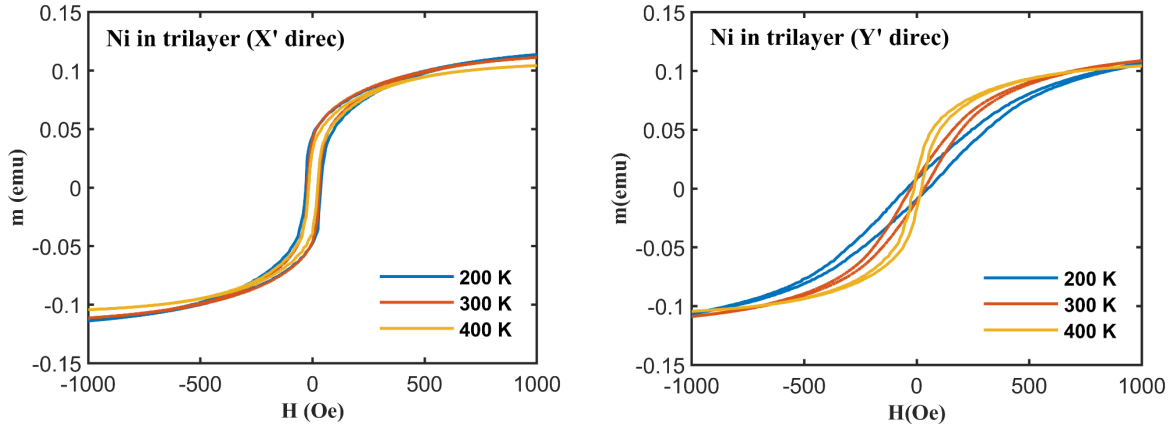


Figure 2.36. Magnetization curves at varying temperatures for the sample 5 (Ni/(YXl) 36° LiNbO<sub>3</sub>/Ni) along two in-plane directions.

Due to the nonlinear ME behavior observed in quasi-static regime is predominantly due to the magnetic nonlinearity in the magnetostrictive phase. Both magnetostrictive and piezoelectric coupling are supposed to be linear, the ME coefficient  $\alpha_E$  can be determined with the product of gradients of piezomagnetic and piezoelectric effects [48], as follows:

$$\alpha_E = \left| \frac{\partial E}{\partial D} \times \frac{\partial D}{\partial T} \times \frac{\partial T}{\partial S} \times \frac{\partial S}{\partial H} \right| \quad 2.15$$

Consequently, the magnetic field dependency of the ME coefficient can be articulated as  $\alpha_E \propto \partial S / \partial H$ , where  $\lambda$  is the strain due to magnetostriction, thus  $\partial S / \partial H = \partial \lambda / \partial H$ . Given that  $\lambda$  is proportional to  $M^2$ , we derive that  $\alpha_E \propto \partial M^2 / \partial H$ , establishing the connection between the ME response and magnetization. Figure 2.37 illustrates a qualitative concordance between the  $H$  dependence of  $\partial M^2 / \partial H$  and the ME hysteresis loop (permuted the sign of  $\alpha_E$  at the anti-resonances), affirming that the magnetic anisotropy of nickel films in contact with LiNbO<sub>3</sub> substrate reflects the ME anisotropic behavior.

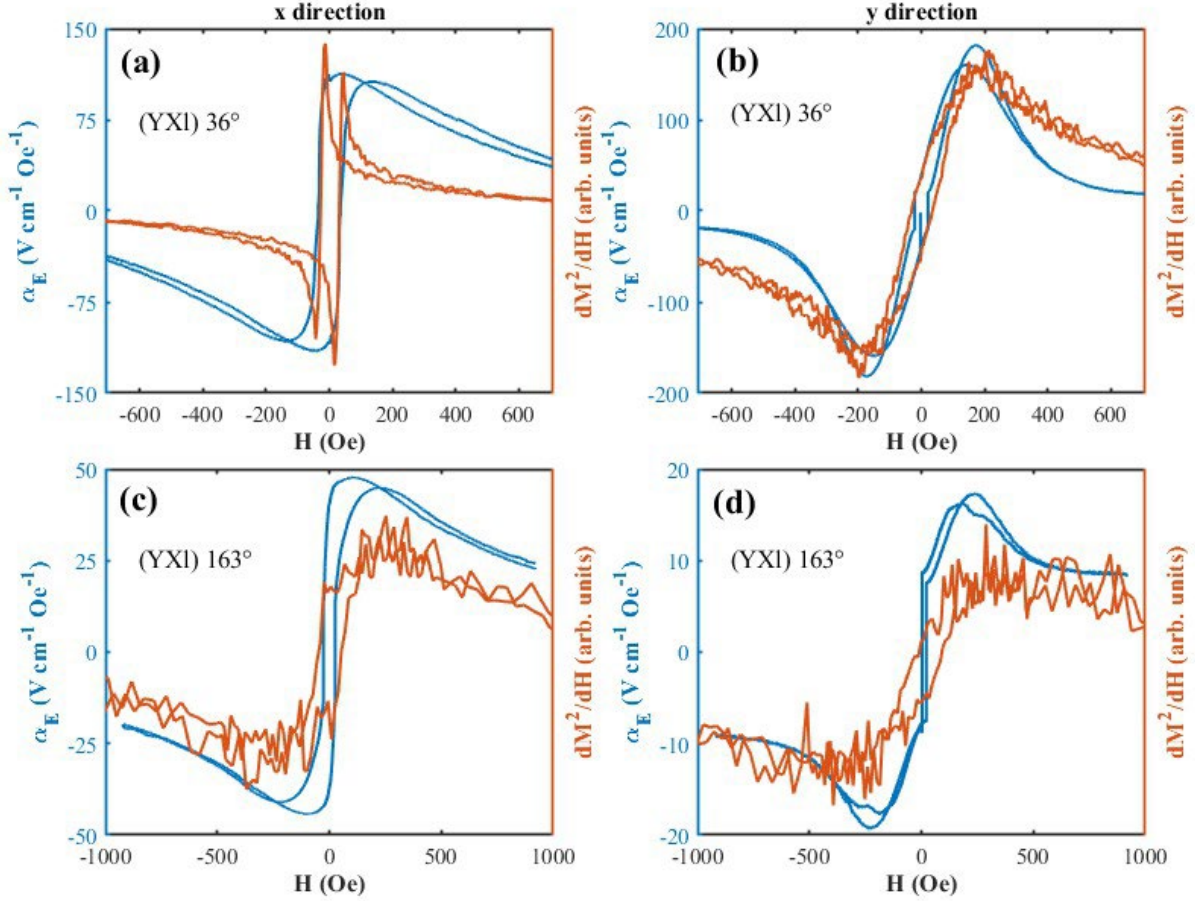


Figure 2.37. ME hysteresis loops and the  $(dM^2/dH)$ - $H$  curves of samples 5 and 6.

### 2.7.1.c. Determination of existence of residual stress

We confirmed the existence of residual stresses by examining the atomic spacing changes in the nickel film using in-plane XRD phi scans along the  $X'$  and  $Y'$  directions. We compared the atomic spacing associated with the (311) peak  $d_{311}$ , of a nickel film deposited on the  $\text{LiNbO}_3$  substrate with that of the this nickel film after detachment from the  $\text{LiNbO}_3$  substrate. As shown in Figure 2.38, with the ME transducer sample 5, the  $d_{311}$  in the  $X'$  and  $Y'$  directions was estimated by fitting the measured (311) peaks with a pseudo-Voigt function. As shown in Table 2.5, the recorded negative (positive) atomic spacing shift indicates the presence of negative (positive) residual stress in the  $X'$  ( $Y'$ ) direction. Using a Young's modulus of 207 GPa and a Poisson's ratio of 0.29 for nickel, a temperature change  $\Delta T$ , of approximately -70 K was derived. However, this temperature change of -70 K is slightly less than the previously estimated temperature change of -100 K during nickel films deposition. This discrepancy is attributed to the fact that grazing incidence in-plane XRD measurements predominantly capture the upper part of the Ni films, as opposed to the segment in direct contact with the  $\text{LiNbO}_3$  substrate.

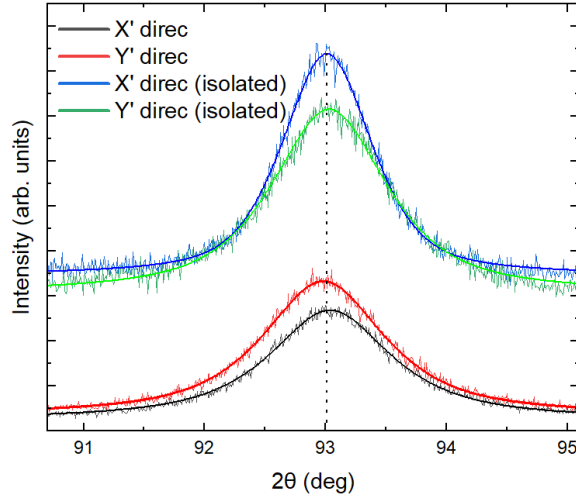


Figure 2.38. In-plane XRD Phi scans to determine residual stress in Ni/(YXl)36 LiNbO<sub>3</sub>/Ni Samples.

Table 2.5. Estimation of atomic spacing change and strain

	Ni in trilayer (X' direction)	Isolated Ni (X' direction)	Ni in trilayer (Y' direction)	Isolated Ni (Y' direction)
$2\theta$ (degree)	93.0401	93.0127	92.9828	93.0318
$d_{311}$ (Å)	1.0625	1.0627	1.0630	1.0626
strain (%)		-0.022		0.041

## 2.8 Magnetostriction measurement for two bilayer ME transducer sample

Since nickel serves as the magnetostrictive phase in our ME transducer, measuring its magnetostriction is crucial. We aim to use the study of magnetostriction in our nickel material to validate our hypothesis that magnetostriction in the ME transducer is nonlinear and piezoelectricity is linear. This will provide reliable support for our previous relationships  $\alpha_E \propto \partial M^2 / \partial H$ , or for finite element simulation calculations using the magnetoelastic nonlinear model mentioned in the previous chapter, to predict the nonlinear behavior of the ME coefficient in the quasi-static regime.

As our samples are in a trilayer structure, for convenience in practical applications, the two nickel films sandwiching the piezoelectric material can directly serve as electrodes, efficiently increasing the nickel quantities. Additionally, the measurements of the magnetostriction of Ni in Ni/LiNbO<sub>3</sub> composites using an experimental setup based on laser deflection technology [69], [70] in the laboratory OPTIMAG (Brest), through the collaboration between the laboratory INSP and Dr. Jean-Philipp Jay (OPTIMAG). Generally, such measurements are conducted on bilayer structures, because in a trilayer structure, this could significantly alter the mechanical interactions between the layers. Such interactions could complicate the stress and strain distributions across the layers, thus affecting the precision and interpretability of the magnetostriction measurements.

Table 2.6. Two Ni/LiNbO<sub>3</sub> bilayer samples for magnetostriction study.

Sample	Ni thickness on both side (μm)	LiNbO <sub>3</sub> substrates
7	11.2	36°-Y-cut (14mm x 6mm x 215μm)
8	11.2	36° Y-cut (14mm x 6mm x 512μm)

We produced a layer of nickel with a thickness of 11 μm on 36° Y-cut LiNbO<sub>3</sub> substrates of thicknesses 215 μm and 512 μm respectively, using the same RF sputtering process, to obtain 2 bilayer samples 7 and 8 as shown in Table 2.6 for the following deflectometry experiment to study the magnetostriction behavior of Ni in the bilayer structure. It is worth noting that we have confirmed the crystallographic X axis for this two 36° Y-cut LiNbO<sub>3</sub> substrates, and they can be denominated as (YXl)36° Y-cut with their X axis along their length.

As shown in Figure 2.39, the experimental setup consists of three main parts: a cantilever beam sample fixing system, a laser emission and deflection detection system, and a magnetic field generation system. The sample is mounted on a cantilever beam (3 in Figure (a)), and a laser emitter (1 in Figure (a)) is fixed to reflect the laser off a mirror (2 in Figure (a)) to illuminate the sample surface. When the sample deforms under the applied magnetic field, the angle of the deflected laser changes accordingly. This change in angle is precisely measured by a position-sensitive detector (PSD) (4 in Figure (a)) located on the opposite side of the sample, thereby indirectly obtaining data on the sample's deformation. The length of nickel film  $l$  of our two samples is 1.2 cm and the distance  $L$  is approximately 1.5 m, so  $l \ll L$ , and the sample is fixed at one end with glue, as shown in Figure 2.40. Under these conditions, by precisely measuring the change in the angle of laser deflection  $\theta$ , we can infer the extent of the deformation of the sample and further calculate the magnetoelastic stress coefficient, as illustrated below:

$$b(H) = \frac{E_Y}{6(1+\nu)} \frac{w_s t_s^2}{w_f t_f l} \theta(H) \quad 2.16$$

where  $E_Y$  is the Young Modulus,  $\nu$  is the Poisson's coefficient,  $w_s$  and  $w_f$  are the widths of substrate and film in our sample, respectively,  $t_s$  and  $t_f$  are the thicknesses of substrate and film in our sample, respectively.

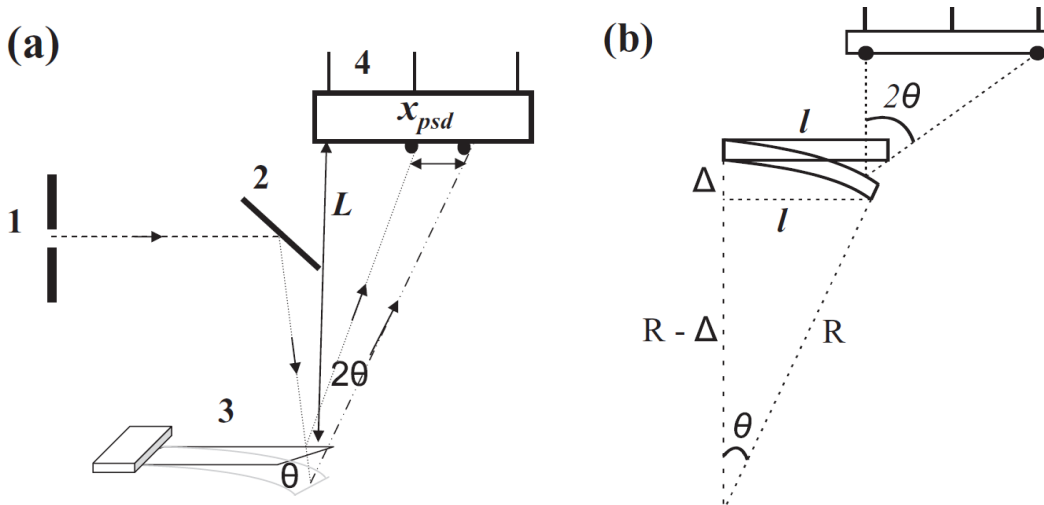


Figure 2.39. Schematic illustration of the magnetostriction measurements based on laser deflection technology. In (a): 1- Laser emitter, 2- Mirror reflection, 3- Cantilever beam

sample, 4- Position-Sensitive Detector (PSD); (b) describes the geometry of laser deflection measurement, where  $R$  is the radius of the circle formed by the cantilever's curvature after bending, and  $\Delta$  represents the bending deflection.[69].



Figure 2.40. Illustration of the sample mounting in the deflectometry experiment.

This magnetoelastic stress coefficient  $b$  can reflect the corresponding shape of magnetostriction but with the opposite sign. It is commonly used to measure the properties of ferromagnetic films. As shown in Figure 2.41, our results indicate that along the length direction of the samples 7 and 8, we observe their magnetostriction behavior similar to bulk polycrystalline nickel material with negative sign, whereas in the width direction, we observed a positive magnetostriction that is two or three times stronger than the values along the length direction.

Subsequently, by deriving  $b$  with respect to  $H$  and plotting the curve of  $d\lambda/dH$  changes with  $H$ , we have obtained results as shown in Figure 2.42. Compared with Figure 2.37, we observed that the shape along the length direction of these two samples is similar to that of sample 5, which is also based on  $36^\circ$  Y-cut. Similarly, the shape along the width direction of these two samples is also similar to that of sample 5. These measurements of magnetostriction for Samples 7 and 8 can represent the magnetostriction behavior of nickel films produced by RF sputtering on  $36^\circ$  Y-cut LiNbO<sub>3</sub>. This allows us to use the relationship that magnetostriction  $\lambda$  is proportional to  $M^2$ , enabling us to predict magnetostriction and ME behavior from only the magnetization measurements in experimental study of magnetostrictive materials.

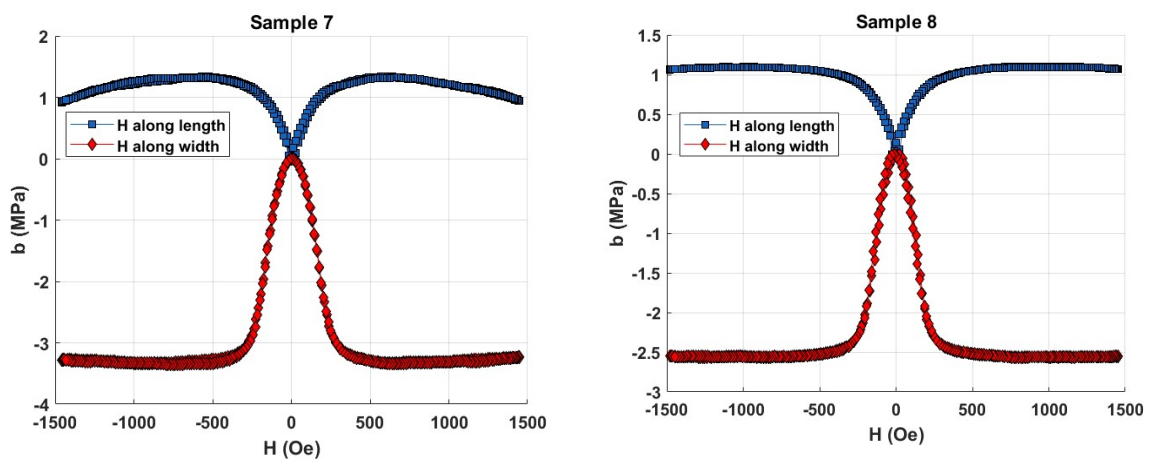


Figure 2.41. Magnetostriction measurements for the nickel films deposited on different thick  $36^\circ$  Y-cut LiNbO<sub>3</sub> substrates for sample 7 and 8, with  $\lambda$  represented by  $b$ , in opposite sign.

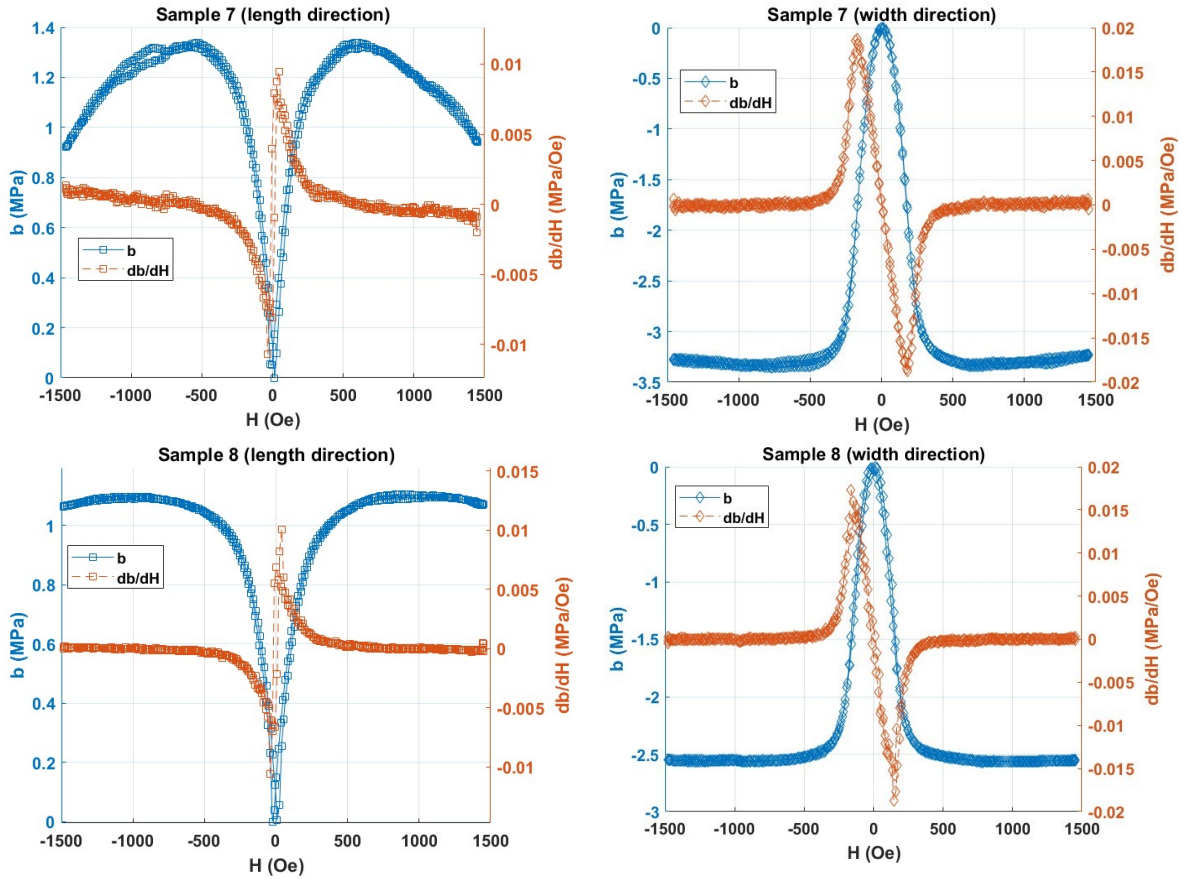


Figure 2.42. Magnetostriction  $b$  curves and  $(db/dH)$ - $H$  curves for samples 7 and 8, with  $\lambda$  represented by  $b$ , in opposite sign.

## 2.9 Comparative study of Ni/LiNbO<sub>3</sub>/Ni ME transducers

### 2.9.1 Selection of LiNbO<sub>3</sub> cuts

Through previous studies on the samples 1-6, we learned that the source of the self-biased ME behavior in our studied Ni/LiNbO<sub>3</sub>/Ni samples is due to negative residual stress altering the magnetic behavior of Nickel. Moving forward, we conducted further comparative studies on different Y-cuts of LiNbO<sub>3</sub> to try to identify a cut that not only maintains self-biased ME behavior but also delivers better ME performance.

We can predict the piezoelectric material's properties of any cut from that of the referenced Z-cut LiNbO<sub>3</sub>, by performing tensor rotation to determine the corresponding properties (this will be detailed in the next chapter). Since the temperature difference is known and less than zero after the fabrication of a ME transducer using RF sputtering, we needed the CTE of LiNbO<sub>3</sub> to be greater than that of Nickel to achieve negative residual stress occurs in nickel films. As shown in Figure 2.43a, for any cut obtained by rotating from a Y-cut at any angle, their CTE along the X-axis always remains unchanged and at its maximum value. As a result, we always achieved maximum negative residual stress along the X-axis of LiNbO<sub>3</sub>, while the residual stress in another in-plane direction perpendicular to this X-axis is positive outside of an angular rotation ranges from 60° to 120°, and negative otherwise. In addition to the CTE, the piezoelectric properties, including the piezoelectric coefficients (Figure 2.43b), piezoelectric

coupling factor (Figure 2.43c), and strain-driven figure of merit (Figure 2.43d), play a crucial role in determining the performance of the piezoelectric material. These parameters are essential for evaluating the efficiency of the material in converting mechanical stress to electrical charge.

According to CTE and all the parameters for the piezoelectric coupling shown in Figure 2.33, the following studies were conducted: By fixing the thickness of the magnetostrictive material on both sides of each sample at approximately 10  $\mu\text{m}$ , and producing the samples through RF sputtering as shown in, we continue our research in the following aspects:

1. Initially, we aim to investigate the impact of different piezoelectric monocrystalline cuts on the ME performance using five LiNbO<sub>3</sub> substrates of different Y-cuts, each with a thickness of 500  $\mu\text{m}$ , as detailed as samples 9-13 in Table 2.7. List of ME samples for comparative studies.. As shown in Figure 2.43c, based on the curve of piezoelectric coupling factor as a function of the angle  $\theta$  rotated from Y-cut, two transversal ( $k_{31}$ ,  $k_{32}$ ) and one longitudinal ( $k_{33}$ ) piezoelectric coupling factors related to the electrical polarization along the thickness direction of  $\theta$  Y-cut LiNbO<sub>3</sub>, as well as the polarization direction for our ME transducer in T-mode.

- With the comparison between 36° Y-cut and 163° Y-cut, their transversal factors are similar, with  $k_{33}$  for the 36° Y-cut is near the maximum of  $k_{33}$  curve (longitudinal LiNbO<sub>3</sub> cut), while  $k_{33}$  for the 163° Y-cut is effectively zero (quasi-shear LiNbO<sub>3</sub> cut). Despite our ME transducer's performance being primarily related to the transverse piezoelectric coefficient, we want to assess whether piezoelectric energy conversion along the thickness direction, which is much smaller than the length and width, has any significant impact.
- For the 41° Y-cut, with almost equivalent  $k_{31}$  and  $k_{32}$ , we want to examine if, when one direction is non self-biased and the other direction is self-biased, the need for magnetic bias affects the maximal ME coefficient value.
- Lastly, for the Y-cut with the largest  $k_{31}$  and theoretically zero  $k_{32}$ , and for a 128° Y-cut with  $k_{32}$  is twice larger than  $k_{31}$ , we want to investigate if a stronger piezoelectric coupling effect in a single direction leads to a dominant response in that direction and enhances the ME performance.

2. Then we studied with the sample 14 based on a thickness of 200  $\mu\text{m}$  Z-cut (90° Y-cut) to investigate whether having the same CTE in two in-plane directions could achieve two isotropic negative residual stresses sufficient to induce self-biased ME behavior in both directions, although the longitudinal piezoelectric coefficients of the Z-cut (90 Y-cut) are very small ( $d_{31} = d_{32} = 1 \text{ pC/N}$ ).

3. Finally, we compared our Ni/LiNbO<sub>3</sub>/Ni samples with the sample 15 based on polycrystalline PZT-5H to study whether a Ni/PZT-5H/Ni trilayer sample obtained through RF sputtering could also exhibit self-biased ME behavior similar to that in the literature with Ni/PZT-5H/Ni fabricated using glue [48], [71].

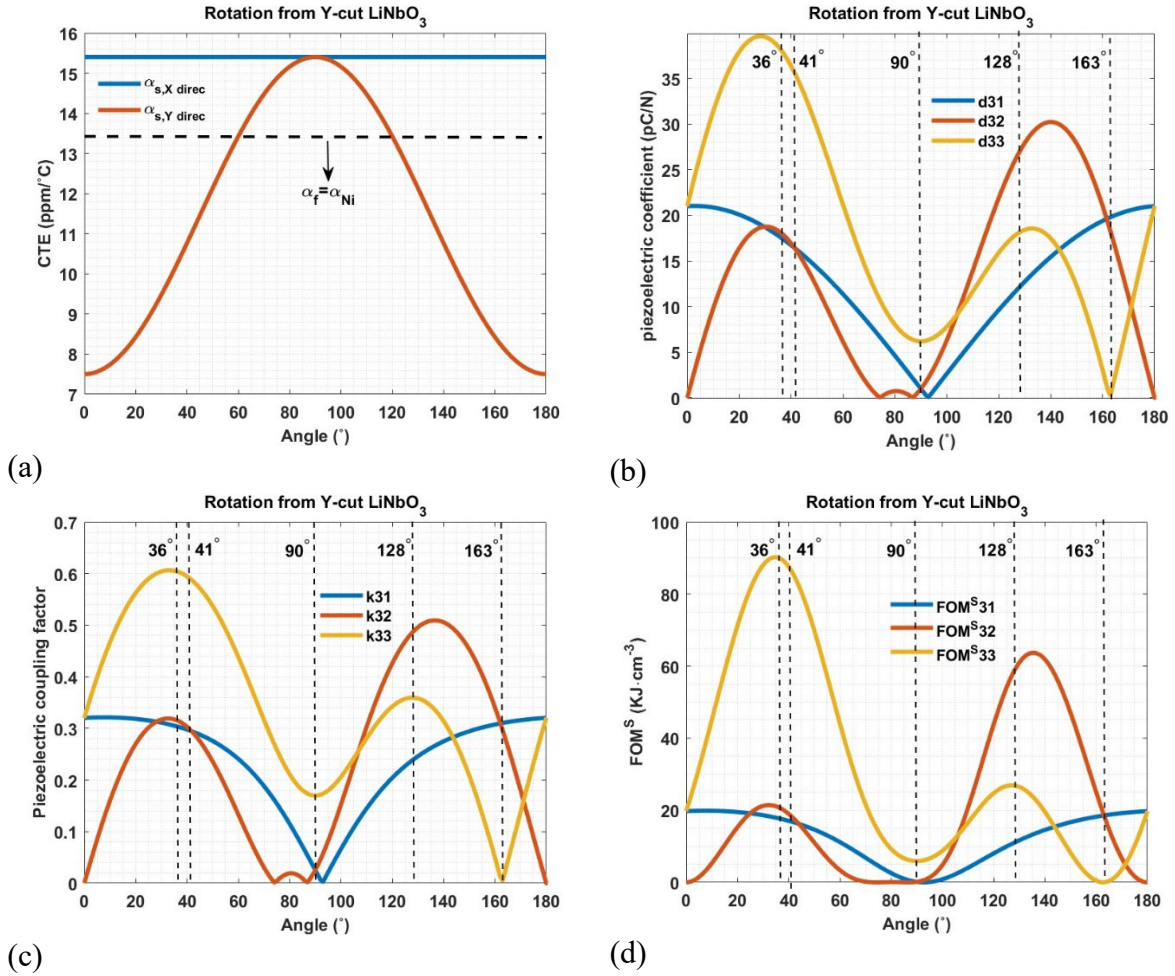


Figure 2.43. Prediction of (a) CTEs, (b) piezoelectric coefficients, (c) piezoelectric coupling factor and (d) strain driven figure of merit for an angle from Y-cut.

Table 2.7. List of ME samples for comparative studies.

Sample	Ni thickness on both side ( $\mu\text{m}$ )	LiNbO <sub>3</sub> substrates
9	11/10.2	36° Y-cut (20mm x 5mm x 500 $\mu\text{m}$ )
10	11/10.2	163° Y-cut (20mm x 5mm x 500 $\mu\text{m}$ )
11	11/10.2	41° Y-cut (20mm x 5mm x 500 $\mu\text{m}$ )
12	11/10.2	Y-cut (20mm x 5mm x 500 $\mu\text{m}$ )
13	11/10.2	128° Y-cut (20mm x 5mm x 500 $\mu\text{m}$ )
14	11/10.2	Z-cut (20mm x 5mm x 200 $\mu\text{m}$ )
15	11/10.2	PZT-5H (11mm x 5mm x 220 $\mu\text{m}$ )

## 2.9.2 Comparison of different cuts of LiNbO<sub>3</sub>

Before growing Nickel film by RF sputtering for samples 9-13, we first confirmed the crystallographic X-axis through in-plane XRD phi-scan on the (0 $\bar{1}2$ ) lattice plane of each LiNbO<sub>3</sub> substrate, finding all their crystallographic X axis aligned along the width direction. According to Figure 2.43a and equation 2.14, these 5 samples should exhibit positive residual

stress in their length direction and negative residual stress in their width direction, leading to self-biased ME behavior in the width direction.

We conducted ME measurements for these five samples in the quasi-static regime in two in-plane directions, as shown in the following three figures. All the measurements for these samples showed that they are non-self-biased in the length direction and self-biased in the width direction, as expected. The Figure 2.44 shows that the self-biased ME coefficients of both sample 9 and 10 are of the same scale in the width direction, but the maximum non-self-biased ME coefficient in the length direction for sample 9 is almost three times of that of sample 10. By comparing sample 9 with sample 11 in Figure 2.45, although the piezoelectric properties of sample 11 based on  $41^\circ$  Y-cut, are similar and slightly lower than those of sample 9 based on  $36^\circ$  Y-cut, we see the same scale of self-biased ME behavior in their width direction. However, the non-self-biased ME behavior in the length direction differs by almost twofold. From the above two comparisons, we could suppose that the piezoelectric properties along the thickness direction have a certain impact on the non-self-biased ME response but a minimal impact on the self-biased ME response.

Next, as shown in Figure 2.46, for samples 12, it's worth noting that we could not find its ME resonance and electrical impedance resonance response through impedance analysis, near the first longitudinal resonance frequency ( $\sim 168$  kHz) using the previously mentioned equation 2.5. Subsequently, we fixed the frequency used in the quasi-static regime around an uncertain ME resonance we found at approximately 220 kHz. Since the piezoelectric coupling factor  $k_{32}$  value of sample 12 is zero, the non-self-biased ME response in the length direction is relatively weak as expected, but it has the largest piezoelectric coupling factor  $k_{31}$  among all the cuts. However, the result is the smallest when compared to other cuts. And next, we see that the self-biased ME response of sample 13 in the width direction is more than twice that of samples 9-12, but despite having a larger  $k_{32}$  value, it did not exhibit the highest ME response among all the measurements.

All samples had very weak self-biased ME responses in their width direction, which were two or more times weaker than their length direction. And except for sample 13 based on  $128^\circ$  Y-cut  $\text{LiNbO}_3$ , the self-biased ME responses of other samples were highly asymmetric. Since the thickness ratio between the magnetostrictive and piezoelectric phases is crucial for the strength of the ME coefficient in most studies on ME transducers [72], [73], we can conclude that these different 500  $\mu\text{m}$ -thick  $\text{LiNbO}_3$  substrates, compared to the previous thickness of 100  $\mu\text{m}$ , reduced this thickness ratio by five times, resulting in very weak self-biased ME behavior. Other unknown factors had a relatively more significant impact, leading to asymmetric outcomes. Consequently, we were unable to conduct a detailed investigation of different cuts using these five samples.

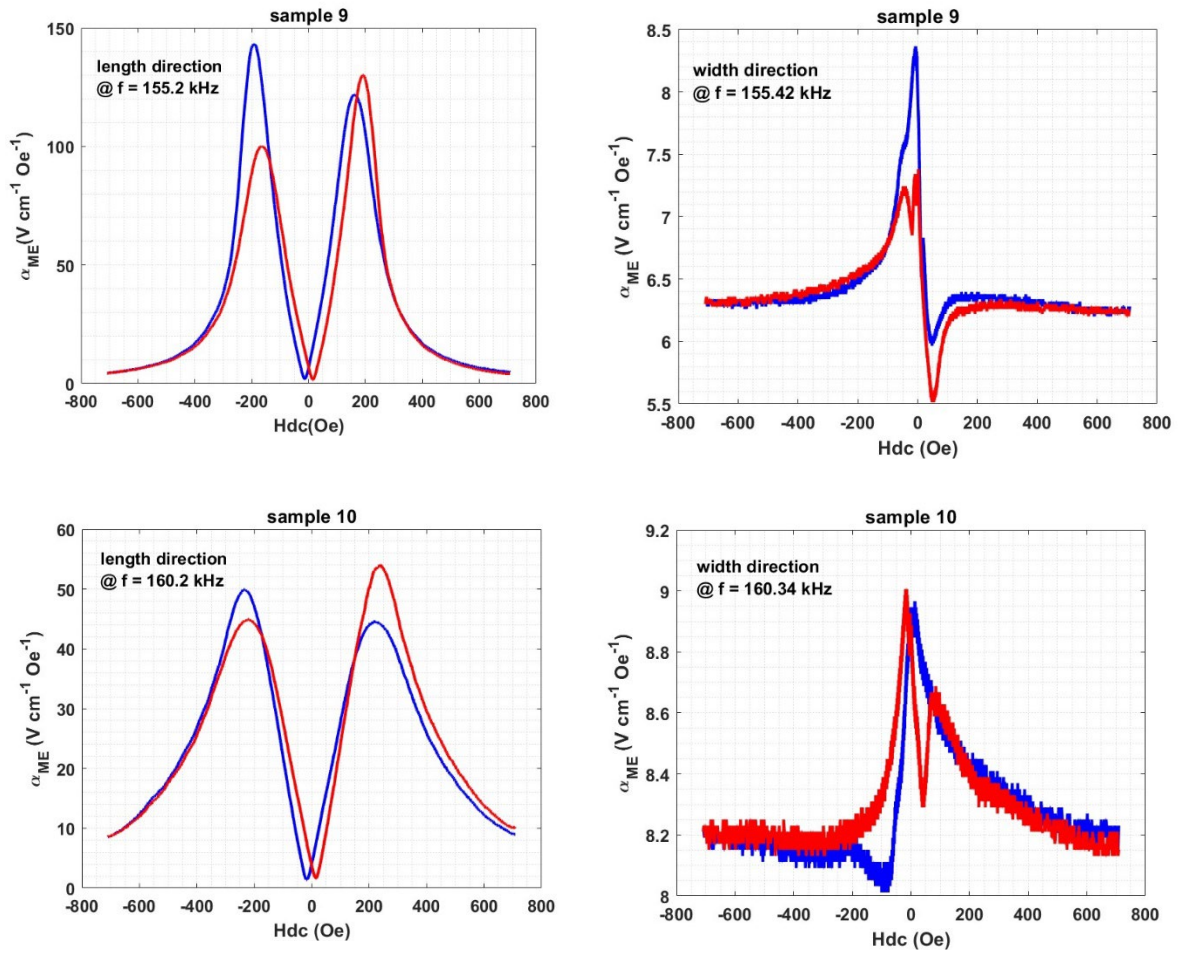


Figure 2.44. ME coefficient measurement in quasi-static regime for sample 9 (36° Y-cut LiNbO<sub>3</sub>) and sample 10 (163° Y-cut LiNbO<sub>3</sub>).

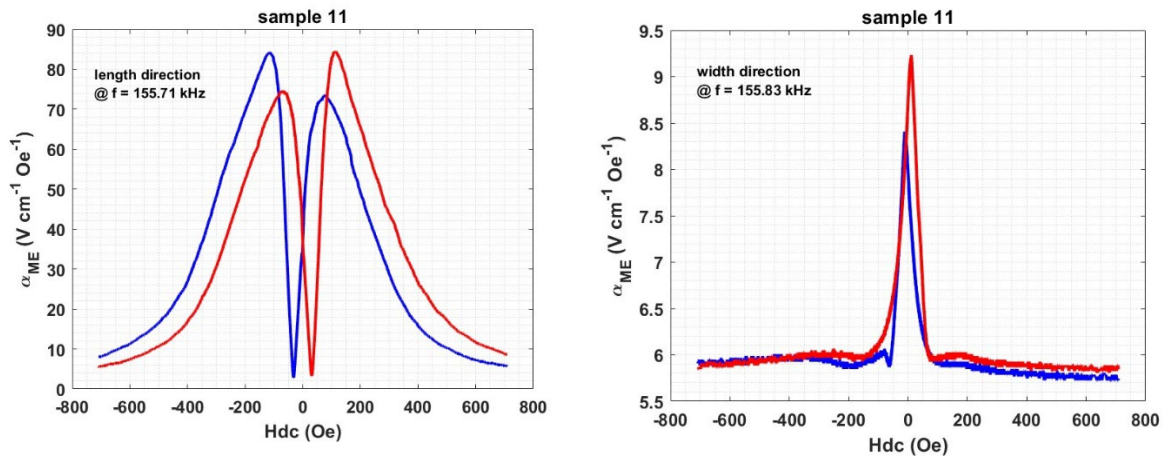


Figure 2.45. ME coefficient measurement in quasi-static regime for sample 11 (41° Y-cut LiNbO<sub>3</sub>).

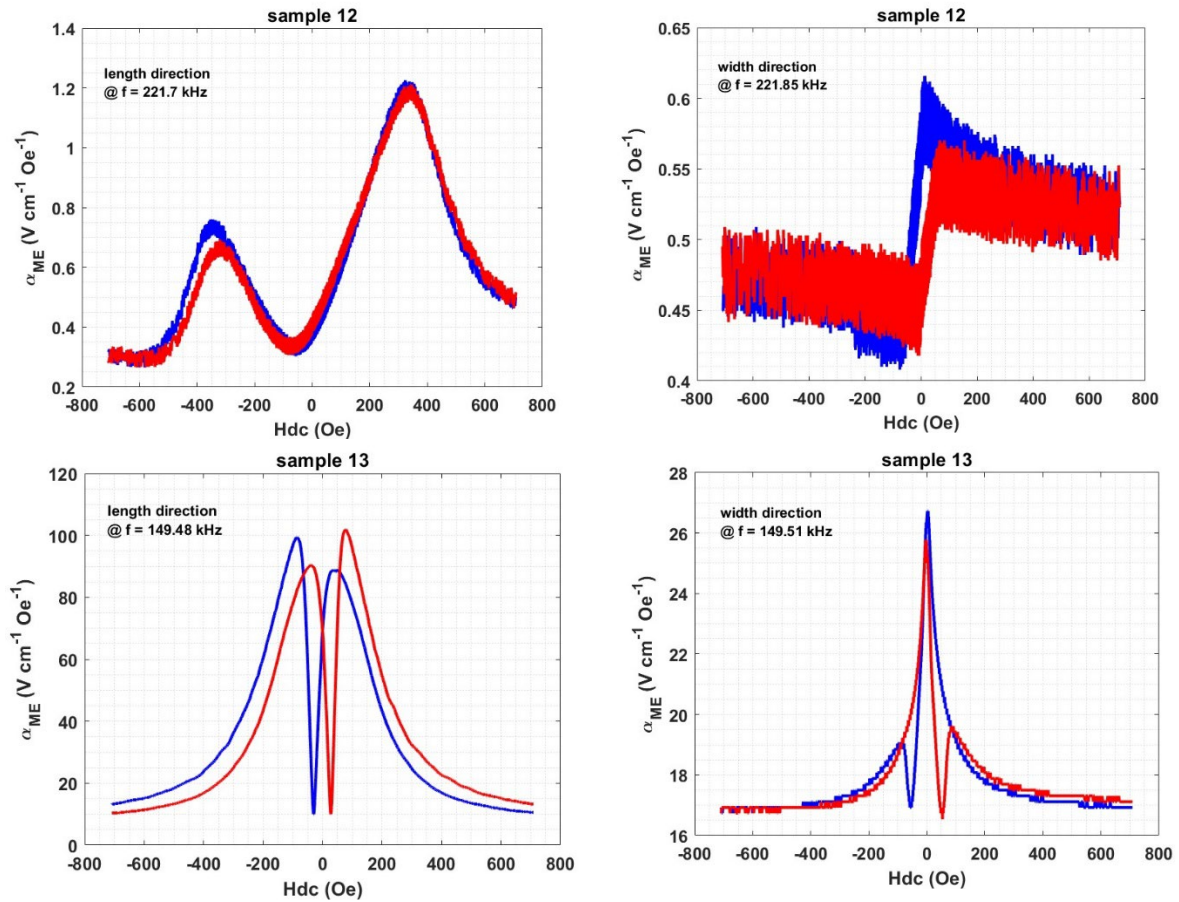


Figure 2.46. ME coefficient measurement in quasi-static regime for sample 12 (Y-cut  $\text{LiNbO}_3$ ) and sample 13 ( $128^\circ$  Y-cut  $\text{LiNbO}_3$ ).

### 2.9.3 Study with Z-cut $\text{LiNbO}_3$

We confirmed the crystallographic X axis through in-plane XRD phi-scan on the  $(0\bar{1}2)$  lattice plane for the Z-cut  $\text{LiNbO}_3$  substrate, finding the crystallographic X-axis aligned along the length direction. As shown in Figure 2.47, we performed ME measurements in the quasi-static regime on samples 14 based on Z-cut. Contrary to our expectations, the samples did not exhibit self-biased behavior in both in-plane directions. This result may be due to the dimensional impact of residual stress during the cooling process of the sample. Given that the length is 20 mm, and the width is 5 mm, the negative residual stress in the length direction is more pronounced than that in the width direction. The stress in the width direction is also significantly offset by a shear stress related to the residual stress in the length direction, projected onto the width direction, which is related to thermal expansion and opposite to this relative shear stress, leading to insufficient force along the width direction to cause self-biased behavior. Therefore, we can suppose that the geometry of the material significantly influences the residual stress produced at the interface between nickel and the  $\text{LiNbO}_3$  substrate. To validate this hypothesis, we will continue with the  $\text{Ni/LiNbO}_3/\text{Ni}$  composites with same dimension in length and width for future research.

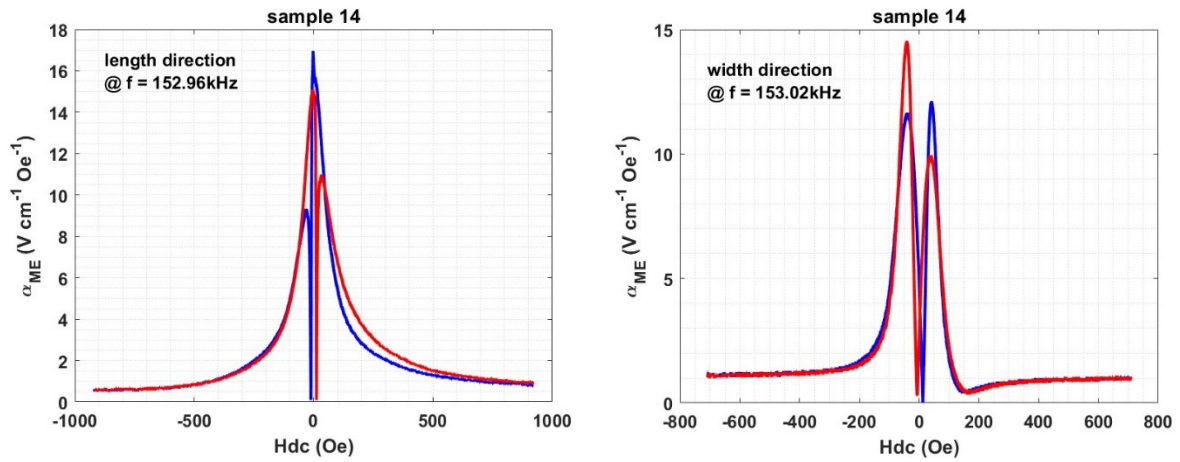


Figure 2.47. ME coefficient measurement in quasi-static regime for sample 14 (Z-cut LiNbO<sub>3</sub>).

### 2.9.4 Comparison between Ni/LiNbO<sub>3</sub>/Ni and Ni/PZT-5H/Ni

After conducting our studies on the Ni/LiNbO<sub>3</sub>/Ni ME transducers, our objective was to investigate whether the Ni/PZT-5H/Ni composite combination, which has been previously studied in literature [48], [71], could also demonstrate self-biased characteristics when fabricated using glue. To accomplish this, we utilized the same RF sputtering process to fabricate a Ni/PZT-5H/Ni sample 15.

Our first step involved characterizing the ME properties of this Ni/PZT-5H/Ni sample in a quasi-static regime. The results of this analysis are depicted in Figure 2.48. We discovered that the Ni/PZT-5H/Ni trilayer transducer displayed non self-biased ME behaviors in both of its in-plane directions, with their shapes being strikingly similar. In order to facilitate a more direct comparison, we transformed the quasi-static regime's ME coefficient results into a hysteresis form, as illustrated in Figure 2.49. From these findings, we can conclude that the in-plane ME behavior of this sample in the quasi-static regime is remarkably similar, with all instances demonstrating a nearly identical magnetic bias for the optimal ME coefficient.

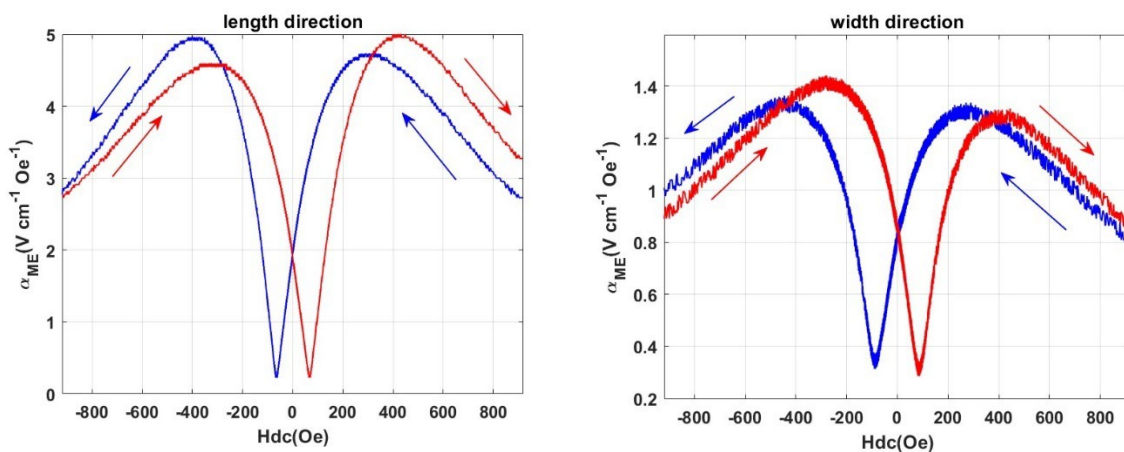


Figure 2.48. ME coefficient measurement in quasi-static regime for sample 15 (Ni/PZT-5H/Ni).

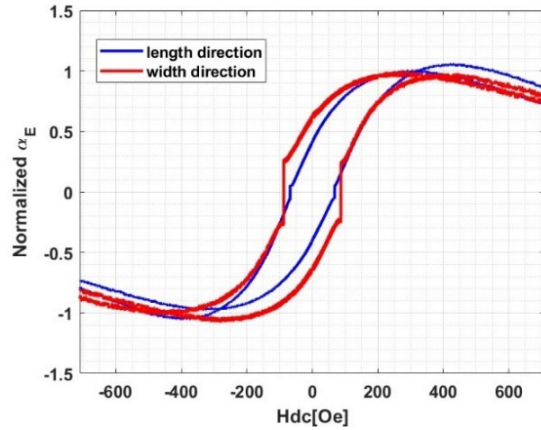


Figure 2.49. ME coefficient hysteresis loops for sample 15 (Ni/PZT-5H/Ni).

Since PZT-5H is a polycrystalline piezoelectric ceramic material, its coefficients of thermal expansion (CTEs) are isotropic, and equal to  $3.5 \cdot 10^{-6} \text{ K}^{-1}$ , like our nickel material. However, the 2 in-plane CTE values of PZT-5H are smaller than those of nickel. Thus, we could preliminarily say that this would lead to the generation of two positive residual stresses in the two in-plane directions we studied when manufacturing this sample via RF sputtering. This view was well supported by the magnetization measurements shown in Figure 2.50, where we observed that the nickel magnetic behaviors are both isotropic in the trilayer structure and in the isolated state. Additionally, by comparing the curves of the nickel material in the trilayer structure and in the isolated state, it was also shown that the Ni film in the trilayer configuration is subjected to equal strengths of positive residual stress in both in-plane directions.

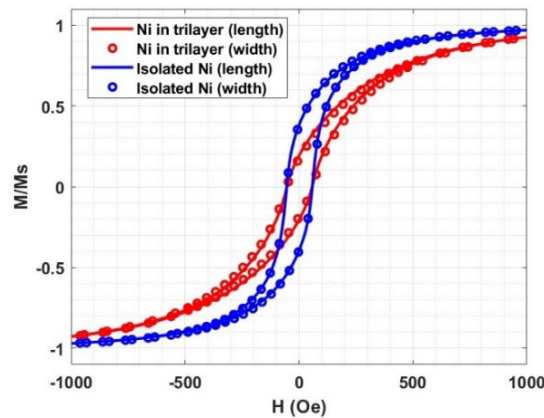


Figure 2.50. ME curves of Nickel in trilayer and in isolated state for sample 15.

When comparing the ME performance of the Ni/PZT-5H/Ni sample with our previously studied Ni/LiNbO<sub>3</sub>/Ni samples, the Ni/LiNbO<sub>3</sub>/Ni demonstrated superior ME coefficient results.

## 2.10 Tests for Optimization of self-biased ME behavior

Based on the Ni/LiNbO<sub>3</sub>/Ni material combination, and the fact that self-biased ME behavior is caused by negative residual stress acting on Ni during the transducer manufacturing process, we attempted to optimize the self-biased behavior in a laminate structure. This was achieved

by using different manufacturing methods to obtain thicker films of the same quality of nickel, thus changing the thickness ratio between the magnetostrictive and piezoelectric phases to increase the ME coefficient. Additionally, based on our previous measurements of the ME coefficient in a quasi-static regime, we observed that in our samples, the ME coefficient of samples 1 and 2 at  $H_{dc} = 0$  approached 100% of the maximum value, while in another sample 6, it was only around 85%. Therefore, we also needed to perform annealing treatments on the produced Ni/LiNbO<sub>3</sub>/Ni samples in a vacuum environment to modify the magnetic behaviors of nickel films with the changes of residual stress in them, and to enhance the remanence value of the ME coefficient at zero  $H_{dc}$  in the self-biased direction.

In our initial studies of ME samples, which included samples 1 and 2 with nickel thicknesses of 32/35  $\mu\text{m}$ , those samples did not show a significantly better ME coefficient than the 10/10  $\mu\text{m}$  samples. This may be due to the limited number of samples studied and the lack of detailed material studies on the nickel films obtained on each sample. We did not observe an improved ME coefficient response with an increase in the thickness ratio of the ME composite. Moreover, since RF sputtering is generally used for thin film deposition in the scale nm, and each sample's nickel films produced through RF sputtering exhibited various defects, especially some darkening on the thicker 32/35  $\mu\text{m}$  nickel films. Therefore, we considered using other methods to manufacture Ni/LiNbO<sub>3</sub>/Ni samples.

Our first idea was to use conductive epoxy glue to bond polycrystalline nickel films onto a LiNbO<sub>3</sub> substrate, enabling the use of nickel films as electrodes while altering the thickness ratio in ME transducer through bonding films of different thicknesses. But we lacked a method to precisely apply a fixed pre-strain during the gluing process. This made it extremely difficult to reproduce self-biased ME behavior in this manufacturing method, as the nickel films produced on both sides of the LiNbO<sub>3</sub> substrate were subject to inhomogeneous and disparate residual stresses.

Another idea we had was to increase the thickness of our nickel films obtained via RF sputtering by using electrodeposition, as used in [74], [75]. We conducted several experiments, but the nickel films from RF sputtering tended to detach from the LiNbO<sub>3</sub> substrate during electrodeposition due to gas bubbles generated in the chemical reaction. This method is viable but requires further precise adjustment of all parameters in the electrodeposition process.

Next, we conducted optimization studies on two existing samples produced via RF sputtering. as the internal electrical impedance of Ni/LiNbO<sub>3</sub>/ Ni samples are much higher compared to that sample 15 Ni/PZT-5H/Ni (see Figure 2.51), which makes impedance matching more difficult in practical applications of Ni/LiNbO<sub>3</sub>/Ni. In a similar ME coefficient condition, these Ni/LiNbO<sub>3</sub>/Ni transducers provide less electric power than Ni/PZT-5H/Ni transducers.

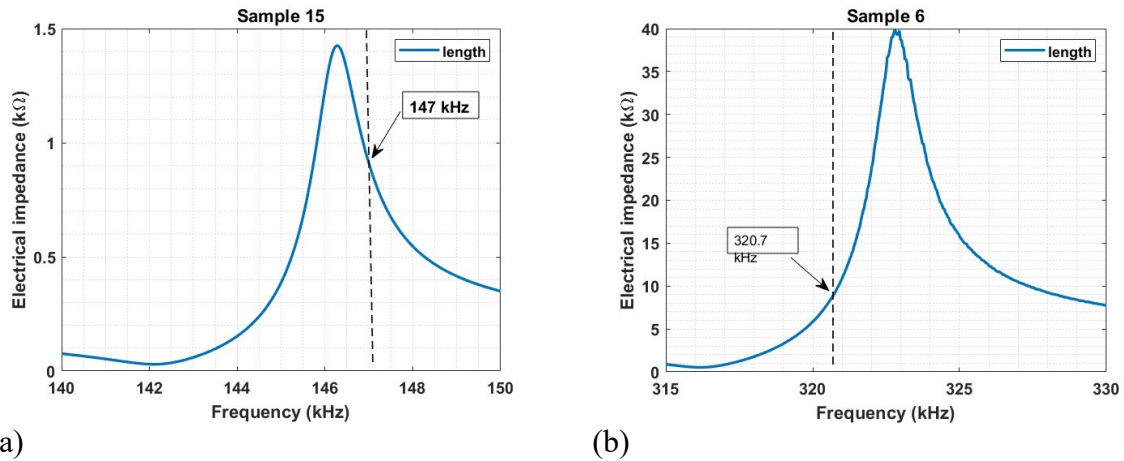


Figure 2.51. Electrical impedance measurements of (a) Ni/PZT-5H/Ni composite (sample 15), and (b) Ni/LiNbO<sub>3</sub> (163° Y-cut)/Ni composite (sample 6).

### 2.10.1 Study of transducers on black LiNbO<sub>3</sub> substrates

According to [76], black lithium niobate demonstrates a lower electrical resistivity compared to traditional lithium niobate while maintaining comparable piezoelectric properties. The “black” color results from reduction annealing in a low-oxygen environment, which creates oxygen vacancies that to enhance electrical conductivity (reduce electrical resistivity). This characteristic makes black lithium niobate an ideal substitute to reduce internal impedance to enhance our Ni/LiNbO<sub>3</sub>/Ni ME transducer performance. Therefore, we compared two samples 16 and 17 with the same 36° Y-cut for LiNbO<sub>3</sub> as shown in Table 2.8, to study whether ME transducers made with black LiNbO<sub>3</sub> could exhibit a smaller electric impedance response around the first longitudinal resonance frequency, to determine delivering superior electric power. Furthermore, we conducted annealing treatments on ME transducers based on standard LiNbO<sub>3</sub> substrates to investigate the feasibility of enhancing the ME coefficient response through annealing.

Table 2.8. Two samples of different types of LiNbO<sub>3</sub> with the same crystalline 36° Y-cut.

Sample	Ni thickness on both side (μm)	LiNbO <sub>3</sub> substrates
16	10/10	36° Y-cut (10mm x 5mm x 100μm)
17	10/10	Black 36° Y-cut (10mm x 5mm x 100μm)

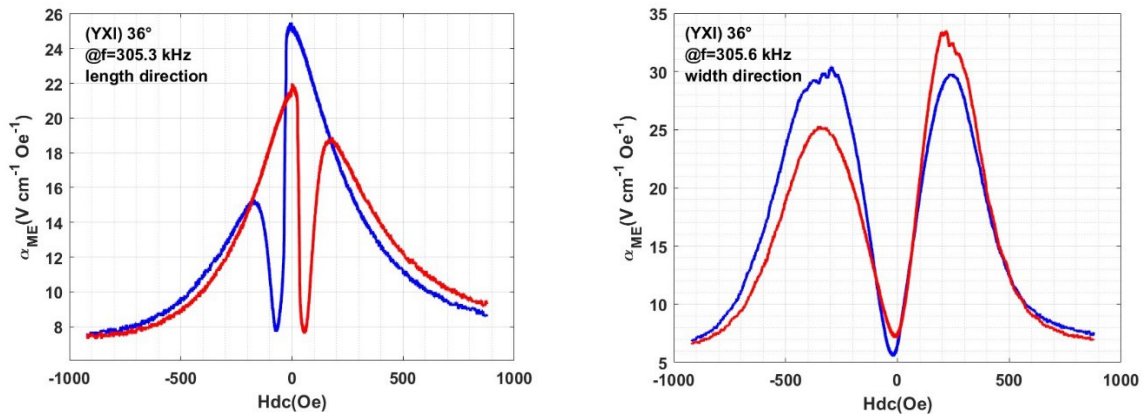


Figure 2.52. In-plane ME coefficient measurement for the sample 16 include 36 Y-cut LiNbO<sub>3</sub>.

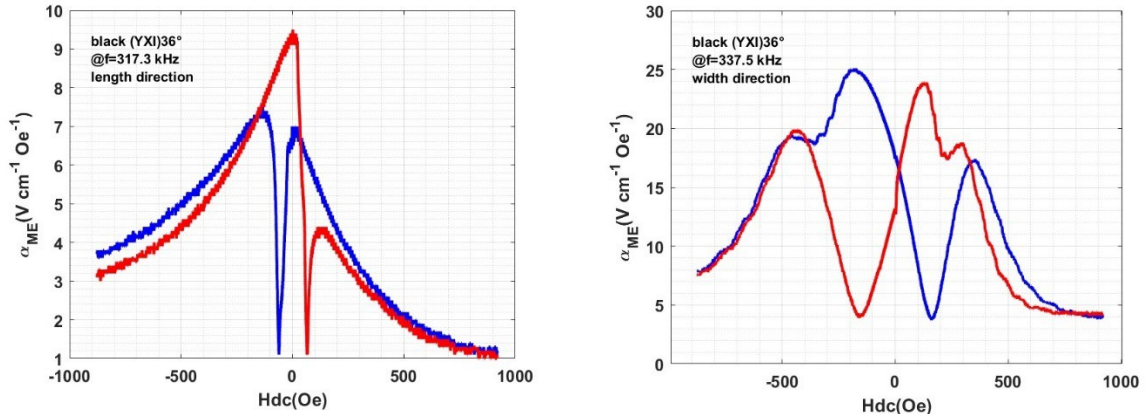


Figure 2.53. In-plane ME coefficient measurement for the sample 17 include black 36 Y-cut LiNbO<sub>3</sub>.

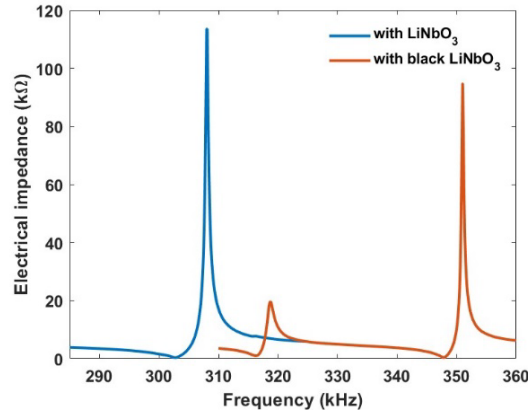


Figure 2.54. Electrical impedances of sample 16 (with LiNbO<sub>3</sub>) and 17 (with black LiNbO<sub>3</sub>).

As shown in Figure 2.52 and Figure 2.53, for these two Ni/LiNbO<sub>3</sub>/Ni samples, the ME measurement shows self-biased ME behavior along the length direction (parallel to X axis), and non self-biased behavior along the width direction (perpendicular to X axis). Subsequently, as shown in Figure 2.54, during the electrical impedance measurements near the predicted first longitudinal EMR frequency, the samples containing LiNbO<sub>3</sub>, like other previously studied cuts of LiNbO<sub>3</sub>, exhibit only one resonance. However, the samples containing black LiNbO<sub>3</sub>, like sample 17 display two resonance peaks, with the first peak in the samples containing black LiNbO<sub>3</sub> being five times smaller than the electrical impedance resonance peak of those containing regular LiNbO<sub>3</sub>.

Subsequently, we measured the ME coefficients of these two samples in the dynamic regime, as shown in the figures. Although using black LiNbO<sub>3</sub> as a substitute could reduce the internal electrical impedance of the ME transducer, the resulting voltage also decreased. According to equation 2.9, electric power is directly proportional to the square of the voltage (voltage is proportional to the ME coefficient) and inversely proportional to electrical impedance. Thus, in the ME transducers using black LiNbO<sub>3</sub>, enhancing the electric power by lowering internal

impedance was not enough to offset the decrease in the square of the voltage. As a result, we obtained lower electric power compared to using normal  $\text{LiNbO}_3$  piezoelectric material.

### 2.10.2 Study of Annealing for Ni/LiNbO<sub>3</sub>/Ni sample

Finally, we explored whether annealing could enhance the thermal residual stresses in the nickel films within the trilayer Ni/LiNbO<sub>3</sub>/Ni structure through annealing in vacuum. We continued our studies with the previously mentioned two samples, conducting annealing at various temperatures for set durations. Subsequently, we measured the changes in the magnetic behavior of nickel in the samples using VSM. It is worth noting that, for VSM measurements, we needed to cut the ME samples into 5x5 mm planar dimensions to fit measurements along both the length and width onto the VSM sample holder. Since we needed to continue further studies on Sample 16, which contains regular  $\text{LiNbO}_3$ , and could not cut this sample 16, we only performed the magnetization measurement using VSM along its length.

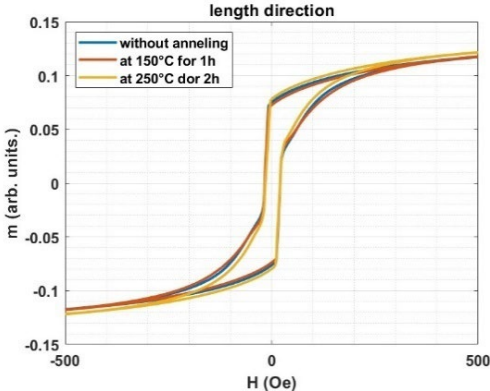


Figure 2.55. Magnetic curves in length direction, under different annealing treatments for sample 16.

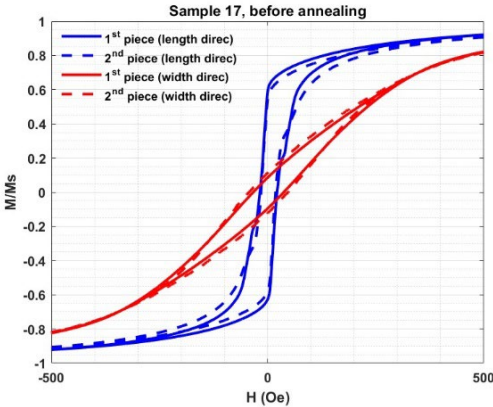


Figure 2.56. Magnetic curves before annealing treatment for sample 17.

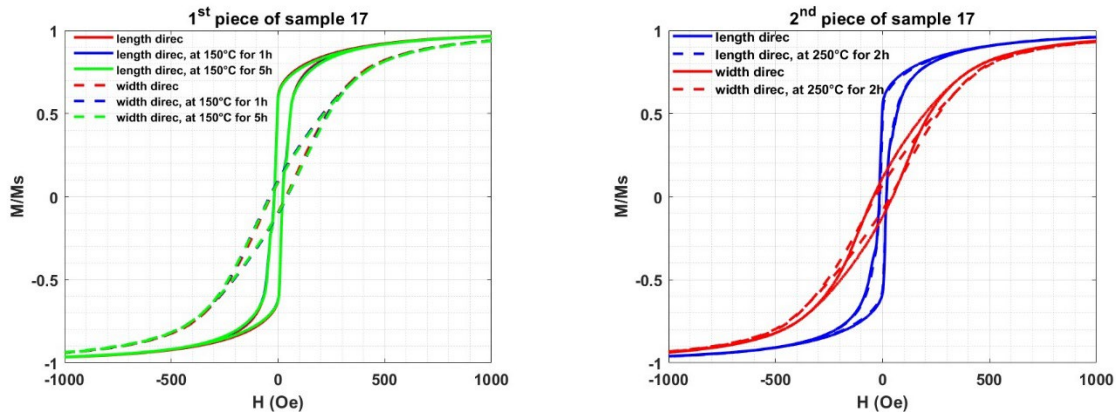


Figure 2.57. Magnetic curves under different annealing treatments for sample 17, with 2 pieces in a similar dimension.

For sample 16, since we didn't cut it, we conducted magnetization measurements only along its length direction using VSM after two different annealing treatments. As shown in Figure 2.55, we can see that sample 16 didn't exhibit any significant change in its magnetic behavior after a 150 °C annealing treatment, and only a minor change after a 250 °C annealing treatment. For sample 17, we cut it into two 5x5 mm planar pieces, and the in-plane magnetic behaviors of the two pieces before annealing are shown in Figure 2.56, displaying very similar magnetic behaviors. We subjected the two pieces to annealing treatments at different temperatures. As shown in Figure 2.57, the annealing at 150 °C didn't alter in-plane magnetic behaviors of sample 17 either. Therefore, we can confirm that all previously studied Ni/LiNbO<sub>3</sub>/Ni samples, manufactured using the same RF sputtering, had a deposition temperature for the nickel films close to 150 °C. When we annealed the other piece of sample 17 at 250 °C for 2 hours, we observed a noticeable change in the magnetic behavior along the width of the material, but no significant changes in the direction of the self-biased ME behavior we were interested in. According to Figure 2.52 and Figure 2.53, the two studied samples had already achieved maximum self-biased ME behavior along their length direction at  $H_{dc} = 0$  Oe, indicating that the magnetic behavior along the length direction had reached the maximum impact of negative residual stresses. Therefore, the annealing method intended to enhance negative residual stresses should be applied, like in previous samples 11 and 12, which did not show the maximum ME coefficient at  $H_{dc} = 0$  Oe in the self-biased direction, or in potential future ME transducers where nickel thickness might be increased through electrodeposition. This method could counteract the internal stresses of newly formed nickel material and enhance thermal residual stresses, having a relatively more significant impact on thicker nickel films.

## 2.11 Comparison of ME coefficient of self-biased Ni/LiNbO<sub>3</sub>/Ni samples with others self-biased ME materials

We selected five samples as shown in the table below and compared the ME coefficients measured along their length with other self-biased ME materials mentioned in the literature in Chapter 1. The results indicate that our Ni/LiNbO<sub>3</sub>/Ni composites exhibit relatively superior ME coefficients at their resonance frequencies, both at the optimal magnetic bias field  $H_{dc,opt}$  and at  $H_{dc} = 0$ , compared to other self-biased ME materials. Since the literature does not provide data on the deliverable electric power for other self-biased ME materials, we did not compare this ME performance parameter.

Table 2.9. Configuration of compared Ni/LiNbO<sub>3</sub>/Ni and Ni/PZT/Ni composite samples.

Sample	Ni thickness on both side (μm)	LiNbO <sub>3</sub> substrates
1	10/10	36° Y-cut (30mm x 5mm x 100μm)
2	35/32	36° Y-cut (30mm x 5mm x 100μm)
5	11/10.2	36° Y-cut (20mm x 5mm x 100μm)
6	11/10.2	163° Y-cut (10mm x 5mm x 100μm)
15	11/10.2	PZT-5H (11mm x 5mm)

Table 2.10. Comparison of ME coefficients of our studied ME composites with self-biased ME materials reported in the literature.

Type	Combination	Synthesis	$\alpha_{Hdc=0}$ (V cm <sup>-1</sup> Oe <sup>-1</sup> )	$\alpha_{max}$ (V cm <sup>-1</sup> Oe <sup>-1</sup> )	$f_{Hac}$ (kHz)
Single phase	Sr <sub>3</sub> Co <sub>2</sub> Fe <sub>24</sub> O <sub>41</sub>	co-fired	$33 \times 10^{-3}$	$42 \times 10^{-3}$	1
	BiFeO <sub>3</sub>	film	3	3.5	-
0-3 composite	CFO/Sr <sub>1.9</sub> Ca <sub>0.1</sub> NaNb <sub>5</sub> O <sub>15</sub>	co-fired	$5.7 \times 10^{-3}$	$6.7 \times 10^{-3}$	5
2-2 composite	CFO/PZT	film	0.4	0.55	1
	Ni/PZT	epoxy	$63.3 \times 10^{-3}$	$87.3 \times 10^{-3}$	1
	Ni/MFC	epoxy	1.25	1.38	1
	SmFe <sub>2</sub> /PZT	epoxy	39.5	48	119.7
	PZT/Ni/FCNSB	epoxy	49.5	51.4	0.35
	Ni/PZT/Ni	epoxy	10	35	resonance
	PZT/Ni/FCNSB	epoxy	89.2	100	193.3
	Sample 1	RF sputterd	87	87	102.8
	Sample 2	RF sputterd	40	40	97.9
	Sample 5	RF sputterd	111.58	112.63	162.6
	Sample 6	RF sputterd	36.27	44.6	320.9
	Sample 15	RF sputterd	1.95	4.72	146.3

## 2.12 Comparison of maximum deliverable electric power with Terfenol-D/PZT

Since our research on ME composites focuses on using them as ME energy transducers for wireless power transfer, it is essential to compare not only their ME coefficients with other materials but also the maximum electric power they can deliver. In the initial phase of my doctoral research, I continued Kevin's work on Terfenol-D/PZT composites. As he previously incorporated Metglas films to optimize the performance of magnetoelectric materials, we fabricated three samples, as shown in Table 2.11. These samples were then compared with the three Ni/LiNbO<sub>3</sub>/Ni trilayer composite materials that we studied later (see Table 2.12).

As shown in Table 2.12, the Ni/LiNbO<sub>3</sub>/Ni samples exhibit relatively advantageous ME coefficients compared to the Terfenol-D/PZT samples. However, due to the generally higher internal electrical impedance of the Ni/LiNbO<sub>3</sub>/Ni ME samples compared to the Terfenol-D/PZT-5H ME samples at their respective frequencies corresponding to their maximum

deliverable electric power, the maximum electric powers of Ni/LiNbO<sub>3</sub>/Ni ME samples are lower than that of Terfenol-D/PZT-5H ME samples. It is also worth noting that for the Terfenol-D/PZT-5H ME samples, measurements were not conducted at  $H_{dc} = 0$  because their ME coefficients were significantly lower than those at the optimal magnetic bias field  $H_{dc,opt}$ .

Table 2.11. Dimension and fabrication method of Terfenol-D/PZT and Terfenol-D/Metglas/PZT-5H samples.

Sample	Composition	Magnetostrictive dimension (each layer)	Piezoelectric dimension	Fabrication method
18	Terfenol-D/PZT	14 mm x 10 mm x 0.75 mm	20 mm x 10 mm x 1 mm	Bonded with epoxy glue
19	Terfenol-D/PZT	14 mm x 10 mm x 0.75 mm	20 mm x 10 mm x 1.2 mm	Bonded with epoxy glue
20	Terfenol-D/Metglas/PZT-5H /Metglas/ Terfenol-D	Terfenol-D: 14 mm x 10 mm x 0.75 mm Metglas: 14 mm x 10 mm x 0.035 mm	20 mm x 10 mm x 1 mm	Bonded with epoxy glue

Table 2.12. Performance comparison of Terfenol-D/PZT based and Ni/LiNbO<sub>3</sub>/Ni magnetolectric composites.

Sample	$H_{dc,opt}$ (Oe)	$f_r$ (kHz)	$\alpha_E$ at $H_{dc,opt}$ (V cm <sup>-1</sup> Oe <sup>-1</sup> )	$\alpha_E$ at $H_{dc} = 0$ (V cm <sup>-1</sup> Oe <sup>-1</sup> )	$P_{max}$ at $H_{dc,opt}, H_{ac} = 1$ Oe (μW)	$P_{max}$ at $H_{dc} = 0, H_{ac} = 1$ Oe (μW)
1	0	102.85	126	126	10.1	10.1
5	37.5	162.6	88.95	88.6	9.65	9.64
6	106	320.6	49.42	41.87	3.76	2.69
18	284	69.45	25.3	-	1250	-
19	286	71.3	6.5	-	130	-
20	370	71.55	29	-	1570	-

## 2.13 Conclusion

In this chapter, we presented the experimental study and performance analysis of Ni/LiNbO<sub>3</sub>/Ni magnetolectric (ME) composites fabricated using RF sputtering. Ulisses Acevado discovered self-biased ME behavior in Ni/LiNbO<sub>3</sub> (36° Y-cut)/Ni materials, but the origin of this behavior was not yet clear. In my doctoral research, we first compared two Ni/LiNbO<sub>3</sub>/Ni samples with different cut angles, 36° Y-cut and 163° Y-cut, to investigate their magnetic properties. The study revealed that these materials exhibit magnetic anisotropy along two mutually perpendicular in-plane directions. This finding provided a direction for further exploring the relationship between ME behavior and the magnetostrictive properties of nickel. By studying samples with both 36° Y-cut and 163° Y-cut, we identified that the self-biased ME behavior in Ni/LiNbO<sub>3</sub>/Ni composites is associated with the residual negative stress induced during the RF sputtering process, which results from the thermal expansion mismatch between nickel and LiNbO<sub>3</sub>.

Subsequently, since LiNbO<sub>3</sub> is a single crystal, we used tensor rotation to study the piezoelectric coefficients and thermal expansion coefficients of different cuts, thus determining the optimal cut angles for subsequent experiments. Although the magnetostrictive volume ratio of the samples in these studies was relatively small, leading to the measurement signals being affected

by other factors and making it difficult to systematically analyze the impact of different cuts on the performance of Ni/LiNbO<sub>3</sub>/Ni composites, we observed an interesting phenomenon in samples containing Z-cut piezoelectric materials: even when the thermal expansion coefficients are isotropic in the two in-plane directions, anisotropic ME behavior was still observed. This suggests that differences in the in-plane dimensions can also affect the distribution of residual stress.

To optimize performance, we further explored using black LiNbO<sub>3</sub> to replace conventional LiNbO<sub>3</sub> to reduce the internal electrical impedance of the ME composites and thereby increase the maximum deliverable electric power. However, due to the relatively lower piezoelectric performance of black LiNbO<sub>3</sub>, the maximum power output remained low despite the reduction in internal impedance.

We also know that self-biased ME behavior is closely related to residual stress. In the Ni/LiNbO<sub>3</sub>/Ni samples, some materials show their maximum ME coefficient at  $H_{dc} = 0$ , while others have it near zero. To address this, we attempted annealing to modify the residual stress, aiming to shift the working point of the materials closer to  $H_{dc} = 0$ .

Finally, we compared the ME coefficients of five Ni/LiNbO<sub>3</sub>/Ni samples with other self-biased ME materials from the literature. Our Ni/LiNbO<sub>3</sub>/Ni composites showed relatively high ME coefficients both at  $H_{dc,opt}$  and  $H_{dc} = 0$ . Additionally, we compared some of the Ni/LiNbO<sub>3</sub>/Ni samples with the previously studied Terfenol-D/PZT-5H samples. The results demonstrated that while Ni/LiNbO<sub>3</sub>/Ni composites exhibit relatively high ME coefficients, they have a smaller maximum deliverable electric power compared to Terfenol-D/PZT-5H composites.

## Chapter3. FE modeling for ME materials

This chapter provides a detailed description of how we use the finite element method (FEM) to model and analyze the coupling effects in our studied ME composites. Given that the thickness of the magnetostrictive layers in this thesis is much smaller than their maximum dimension (e.g., length), directly using a 3D FEM would significantly increase the complexity of the mesh distribution and computational cost. Therefore, we opted for a 2D FEM approach, incorporating shell elements to simulate the thin-film structure of the magnetostrictive layers, effectively reducing computational complexity.

In 2D finite element modeling, the quality of the mesh for the thin-film structure greatly influences the simulation results. To avoid complex mesh partitioning and considering that our studied ME materials operates in ME L-T mode and at the first longitudinal resonance, where the in-plane magnetostrictive behavior is the primary focus, the out-of-plane effects can be neglected. Based on this, we use the shell element formulation to handle the magnetostrictive phase in the thin structure and employ a simplified magnetoelastic anhyseretic model to describe its nonlinear magnetostrictive characteristics, achieving a balance between accuracy and computational efficiency. To validate the robustness and reliability of this model, we compared the simulation results with experimental data under both quasi-static and dynamic conditions, demonstrating its accuracy in modeling thin film deposited ME composite materials.

This chapter first introduces the fundamental governing equations of the magnetoelectric problem and the mathematical formulation of the 2D FEM. It then discusses the application of shell elements in thin-film structure simulation and their advantages in reducing computational complexity. Finally, the accuracy and feasibility of the method are analyzed through numerical simulations and experimental data.

### 3.1 Schematic illustrations of ME transducer in FE modeling

Figure 3.1 illustrates the structure of the trilayer laminate composite materials we studied, highlighting their operation in the L-T mode. The L-T mode signifies that the magnetostrictive phase is magnetized along the longitudinal (L) direction, while the piezoelectric phase is polarized along the transverse (T) direction. The three coordinate systems in the figure represent the material property directions for both the magnetostrictive and piezoelectric phases, as well as the global coordinate system for the overall ME composite in our 2D FEM modeling.

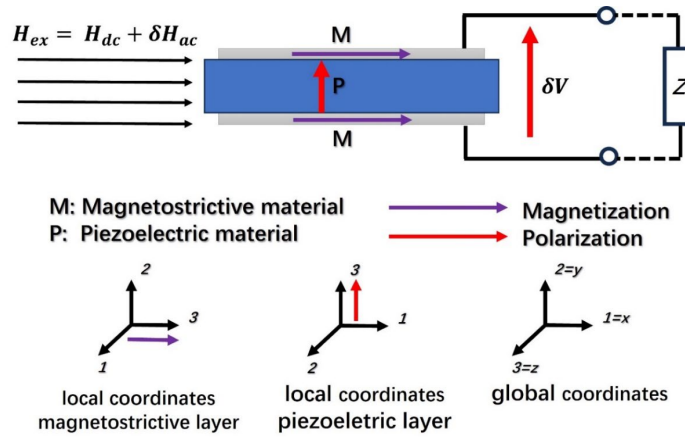


Figure 3.1. Schematic illustration of a ME transducer operating in L-T mode.

As mentioned in Chapter 1, the working principle of our ME materials is shown in Figure 3.2, which consists of a static DC magnetic field and a small dynamic AC magnetic field. On the left side, the static part of excitation field illustrates the nonlinear coupling of the magnetostrictive phase, while the right side shows the linear behavior of the piezoelectric phase under small dynamic condition.

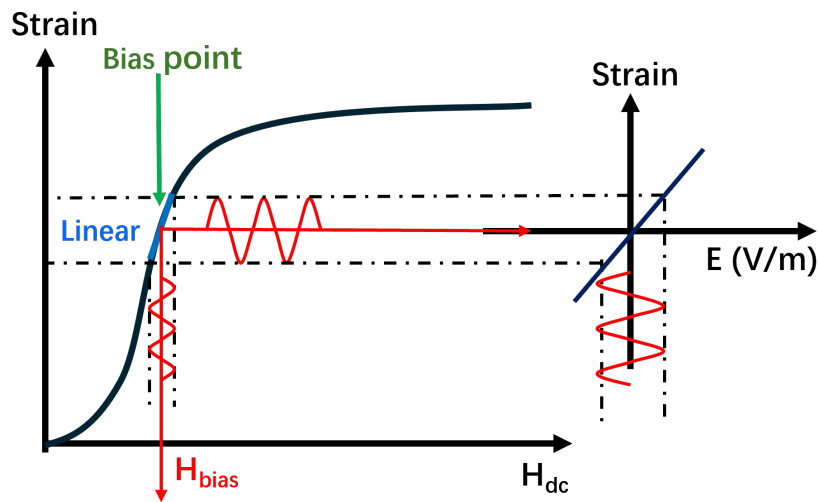


Figure 3.2. Illustration of direct ME operation mode in small signal condition.

## 3.2 Governing equations for ME problem

### 3.2.1 Constitutive laws

#### 3.2.1.a. Electromagnetism

The constitutive relations for electromagnetism are material-specific equations that link the fields with the material properties:

$$\mathbf{B} = \mu \mathbf{H} \quad 3.1$$

$$\mathbf{D} = \varepsilon \mathbf{E} \quad 3.2$$

$$\mathbf{J} = \sigma \mathbf{E} \quad 3.3$$

here,  $\mathbf{B}$  is the magnetic flux density (T),  $\mathbf{H}$  is the magnetic field (A/m),  $\mathbf{D}$  is the electric displacement (C/m<sup>2</sup>),  $\mathbf{E}$  the electric field (V/m), which are first-order tensors (3x1), and  $\mu$  is the magnetic permeability (H/m),  $\varepsilon$  the electric permittivity (F/m),  $\sigma$  the electrical conductivity (S/m), which are second-order tensor (3x3).

### 3.2.1.b. Mechanics

In the domain of linear elasticity, the mechanical stress represented by Cauchy stress tensor  $\mathbf{T}$  (N/m<sup>2</sup>), denotes the force distribution within a material. The resulting mechanical strain  $\mathbf{S}$  (relative deformation without unit), the relationship between  $\mathbf{T}$  and  $\mathbf{S}$  can be described by the Hooke's law:

$$\mathbf{T} = \mathbf{c} : \mathbf{S} \quad 3.4$$

where  $\mathbf{T}$  and  $\mathbf{S}$  are both second-order tensors (3x3), with  $\mathbf{c}$  representing the stiffness tensor (N/m<sup>2</sup> or Pa), which is a fourth-order tensor (6x6) encapsulates the material's resistance to deformation. The relationship of Hooke's law can often be complex due to its representation as a fourth-order tensor requiring four indices. To simplify this, we can use the Voigt notation, which condenses the tensors  $\mathbf{T}$  and  $\mathbf{S}$  into a 6x1 symmetric matrix by treating pairs of indices as single indices. This notational system facilitates computations in anisotropic elasticity by reducing the tensor complexity, making six independent entries that correspond to material stiffness along different axes and planes, and  $\mathbf{T}$  and  $\mathbf{S}$  have been rewritten as:

$$\mathbf{T} = [T_{xx}, T_{yy}, T_{zz}, T_{yz}, T_{xz}, T_{xy}]^t = [T_1, T_2, T_3, T_4, T_5, T_6]^t \quad 3.5$$

$$\mathbf{S} = [S_{xx}, S_{yy}, S_{zz}, 2S_{yz}, 2S_{xz}, 2S_{xy}]^t = [S_1, S_2, S_3, S_4, S_5, S_6]^t \quad 3.6$$

Moreover, the mechanical behavior of a material can also be expressed through the displacement field  $\mathbf{u}$  (m), a three-dimensional vector (3x1) accounting for displacement in space. The strain tensor  $\mathbf{S}$  is correlated with this displacement through the relationship:

$$\mathbf{S} = \mathcal{D}\mathbf{u} = \frac{1}{2}(\nabla\mathbf{u} + (\nabla\mathbf{u})') \quad 3.7$$

### 3.2.1.c. Linear magnetostrictive coupling

As shown in Figure 3.2, magnetostriction demonstrates a nonlinear interaction with the magnetic field and mechanical stress within a material. Nonetheless, this interaction can be approximated through linear coupled constitutive equations for small harmonic signal around a magnetic bias.

The relationship between mechanical stress  $\mathbf{T}$  and strain  $\mathbf{S}$  with using the Voigt notation, magnetic field  $\mathbf{H}$ , and magnetic flux density  $\mathbf{B}$  can be generally represented in stress-magnetization or strain-magnetization formulations.

**Stress-magnetization:**

$$\begin{aligned}\mathbf{T} &= c^H \mathbf{S} - e_m^t \mathbf{H} \\ \mathbf{B} &= e_m \mathbf{S} + \mu^S \mathbf{H}\end{aligned}\quad 3.8$$

**Strain-magnetization:**

$$\begin{aligned}\mathbf{S} &= s^H \mathbf{T} + d_m^t \mathbf{H} \\ \mathbf{B} &= d_m \mathbf{T} + \mu^T \mathbf{H}\end{aligned}\quad 3.9$$

here,  $c^H$  (Pa) and  $s^H$  ( $\text{Pa}^{-1}$ ) represent the stiffness and compliance tensors under a constant magnetic field;  $\mu^S$  and  $\mu^T$  are the magnetic permeabilities measured under constant strain and stress, with the common unit (H/m);  $d_m$  (Wb/N or m/A) and  $e_m$  (T or N/(Am)) are the tensor for the piezomagnetic coupling.

When one of two sets of formulations is established, we can derive the other by utilizing the following relations between their parameters:

$$\begin{aligned}c^H &= (s^H)^{-1} \\ e_m &= d_m^t (s^H)^{-1} \\ \mu^S &= \mu^T - d_m^t e_m^S (s^H)^{-1} d_m\end{aligned}\quad 3.10$$

In our study, we utilize the constitutive laws derived from the equation 3.8, to construct our ME problem model:

$$\begin{aligned}\mathbf{T} &= c^B \mathbf{S} - h^t \mathbf{B} \\ \mathbf{H} &= h \mathbf{S} + \nu^S \mathbf{B}\end{aligned}\quad 3.11$$

here  $h$  (A/m or N/Wb) is the piezomagnetic coupling tensor, and  $\nu^S$  (m/H) is the magnetic reluctivity under constant strain. The coefficients inside can be obtained according to the relations as follows:

$$\begin{aligned}c^B &= c^H + e_m^t \nu^S e_m \\ \nu^S &= (\mu^S)^{-1} \\ h &= e_m \nu^S\end{aligned}\quad 3.12$$

### 3.2.1.d. Linear piezoelectric coupling

In piezoelectric theory, the relationship between stress  $\mathbf{T}$ , strain  $\mathbf{S}$ , electric field  $\mathbf{E}$ , and electric displacement  $\mathbf{D}$  can be generally represented in stress-charge or strain-charge formulations.

**Stress-charge:**

$$\begin{aligned}\mathbf{T} &= c^E \mathbf{S} - e_p^t \mathbf{E} \\ \mathbf{D} &= e_p \mathbf{S} + \varepsilon^S \mathbf{E}\end{aligned}\quad 3.13$$

**Strain-charge:**

$$\begin{aligned}\mathbf{S} &= s^E \mathbf{T} + d_p^t \mathbf{E} \\ \mathbf{D} &= d_p \mathbf{T} + \varepsilon^T \mathbf{E}\end{aligned}\quad 3.14$$

here,  $c^E$  (Pa) and  $s^E$  ( $\text{Pa}^{-1}$ ) represent the stiffness and compliance tensors under a constant electric field;  $\varepsilon^S$  and  $\varepsilon^T$  are the magnetic permittivities measured under constant strain and stress, with the common unit (F/m);  $d_p$  (m/V or C/N) and  $e_p$  ( $\text{C}/\text{m}^2$ ) are the tensor for the piezomagnetic coupling.

In practice, the strain-charge material data, more commonly presented in material databases, can be readily converted into the stress-charge form for analysis. The transformation equations from strain-charge to stress-charge parameters are given by:

$$\begin{aligned}c^E &= (s^E)^{-1} \\ e &= d_p^t (s^E)^{-1} \\ \varepsilon_s &= \varepsilon^T - d_p^t (s^E)^{-1} d_p\end{aligned}\quad 3.15$$

### 3.2.2 Equilibrium equations

The state of electromagnetic equilibrium is described by Maxwell's equations, which correlate the electric and magnetic fields within an ME problem. These fields are not independent but part of a complex interaction, especially under varying conditions. The Maxwell equations are presented as follows:

$$\nabla \cdot \mathbf{B} = 0 \quad 3.16$$

$$\nabla \times \mathbf{E} = -\frac{\partial \mathbf{B}}{\partial t} \quad 3.17$$

$$\nabla \cdot \mathbf{D} = \rho_c \quad 3.18$$

$$\nabla \times \mathbf{H} = \mathbf{J} + \frac{\partial \mathbf{D}}{\partial t} \quad 3.19$$

$\rho_c$  is the charge density ( $\text{C}/\text{m}^3$ ),  $\mathbf{J}$  is the current density ( $\text{A}/\text{m}^2$ ).

In addition to Maxwell's equations, the mechanical equilibrium in a continuous medium is described by:

$$\nabla \cdot \mathbf{T} + \mathbf{f} = \rho_m \frac{\partial^2 \mathbf{u}}{\partial t^2} \quad 3.20$$

where  $\mathbf{T}$  is the stress tensor,  $\mathbf{f}$  is the body force per unit volume,  $\rho_m$  the mass density, and the  $\mathbf{u}$  is the displacement vector.

For interfaces between different media, the continuity conditions for the physical variables are specified as:

$$\begin{aligned}
(\mathbf{B}_2 - \mathbf{B}_1) \cdot \mathbf{n} &= 0 \\
(\mathbf{H}_2 - \mathbf{H}_1) \times \mathbf{n} &= \mathbf{J}_s \\
(\mathbf{D}_2 - \mathbf{D}_1) \cdot \mathbf{n} &= \rho_s \\
(\mathbf{E}_2 - \mathbf{E}_1) \times \mathbf{n} &= 0 \\
(\mathbf{T}_2 - \mathbf{T}_1) \cdot \mathbf{n} &= \mathbf{f}_s \\
(\mathbf{S}_2 - \mathbf{S}_1) \times \mathbf{n} &= 0
\end{aligned} \tag{3.21}$$

where  $\mathbf{n}$  represents the unit normal vector pointing from medium '1' to '2',  $\mathbf{J}_s$  is the current density source,  $\rho_s$  is the charge density source, and  $\mathbf{f}_s$  is the applied force.

These boundary conditions show that across the interface between two media, the normal components of  $\mathbf{B}$  and  $\mathbf{D}$  as well as the tangential components of  $\mathbf{E}$  and  $\mathbf{S}$ , must remain continuous.

From the equations 3.16 and 3.17, we can introduce two state variables magnetic vector potential  $\mathbf{a}$  and electric scalar potential  $V$  as:

$$\mathbf{B} = \nabla \times \mathbf{a} \tag{3.22}$$

$$\mathbf{E} = -\nabla V - \frac{\partial \mathbf{a}}{\partial t} \tag{3.23}$$

### 3.3 FE modelling in 2D

#### 3.3.1 Equations for ME problem in quasi-static regime

The coupled equilibrium equation can be obtained by combining the mechanical equilibrium equation 3.20 and the electromagnetic equilibrium equation 3.18 and 3.19. In our case, the displacement current will not be considered, and there is not an applied source current and displacement current in our study, so  $\mathbf{J} = 0$  and  $\partial D / \partial t = 0$ , by considering the piezoelectric material is as a perfect dielectric medium,  $\rho_c = 0$ . Finally, the coupled equilibrium equation can be expressed as:

$$\left\{ \begin{aligned}
\nabla \cdot \mathbf{T} + \mathbf{f} - \rho_m \frac{\partial^2 \mathbf{u}}{\partial t^2} &= 0 \\
\nabla \times \mathbf{H} &= 0 \\
\nabla \cdot \mathbf{D} &= 0
\end{aligned} \right. \tag{3.24}$$

The coupled constitutive relations can be obtained by combining the magnetostrictive constitutive laws 3.11 and the piezoelectric constitutive laws 3.13, and expressed as follows:

$$\begin{cases} \mathbf{T} = c\mathbf{S} - h^t\mathbf{B} - e_p^t\mathbf{E} \\ \mathbf{H} = h\mathbf{S} + v^S\mathbf{B} \\ \mathbf{D} = e_p\mathbf{S} + \varepsilon^S\mathbf{E} \end{cases} \quad 3.25$$

here the stiffness tensor  $c = c^E$  in the piezoelectric phase, and  $c = c^B$  in the magnetostrictive phase.

The relations between state variables  $\mathbf{u}$ ,  $V$  and  $\mathbf{a}$  and the fields  $\mathbf{S}$ ,  $\mathbf{E}$ , and  $\mathbf{B}$  can be derived by the equations 3.7, 3.22 and 3.23, and the eddy current is not considered in our study, so the terme  $-\partial\mathbf{a}/\partial t = 0$ , finally the state variables can be expressed as:

$$\begin{cases} \mathbf{S} = \mathcal{D}\mathbf{u} \\ \mathbf{B} = \nabla \times \mathbf{a} \\ \mathbf{E} = -\nabla V \end{cases} \quad 3.26$$

Finally, the unknown variables of our ME problem are represented by vector potentials  $\{\mathbf{u}\} = u_x, u_y, u_z$ ,  $\{\mathbf{a}\} = a_x, a_y, a_z$ , and scalar potential  $V$ .

### 3.3.2 2D approximations for the field problems

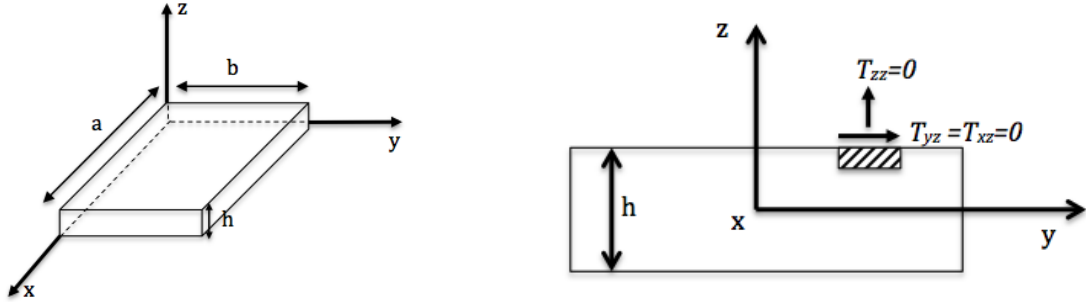


Figure 3.3. Illustration of plane stress approximation.

As shown in Figure 3.3, given a rectangular laminate form with relatively small thickness of the structures in a  $(x, y, z)$  coordinate system, the problem can be addressed using a two-dimensional (2D) plane stress approximation, assuming an isotropic medium condition. In this scenario, under Voigt notation where  $(x, x) = 1$ ,  $(y, y) = 2$ ,  $(z, z) = 3$ ,  $(y, z) = (z, y) = 4$ ,  $(x, z) = (z, x) = 5$ ,  $(x, y) = (y, x) = 6$ , the conditions are such that the out-of-plane stress components in the thickness direction  $z$  are assumed to be negligible and taken to be approximately zero, as follows:

$$\begin{cases} T_3 = T_4 = T_5 = 0 \\ S_4 = S_5 = 0 \\ S_3 = -\frac{\nu}{E_y}(T_1 + T_2) \end{cases} \quad 3.27$$

with  $\nu = -s_{12}/s_{11}$  is the Poisson ratio, and  $E_Y = 1/s_{11}$  is the Young's modulus, and here  $s_{ij}$  are the coefficients in material's compliance tensor.

Regarding the remaining electromagnetic fields in the ME problem in the global coordinate system (see Figure 3.1), we can derive solutions by considering only the components of magnetic induction ( $B_1, B_2$ ) and electric field ( $E_1, E_2$ ) on our two-dimensional working xOy plane. We have assumed that  $B_3$  and  $E_3$  which are perpendicular to the working plane along the x-axis, are both negligible, and equal to zero.

Incorporating the conditions from the plane stress approximation and above assumption for the electromagnetic fields into the constitutive laws, the coefficient tensors should be transformed in the following manner when magnetostrictive and piezoelectric phases in T-mode (magnetization or electrical polarization in transverse direction):

The stiffness tensor:

$$c^X = \begin{bmatrix} \overline{c_{11}^X} & \overline{c_{12}^X} & 0 \\ \overline{c_{12}^X} & \overline{c_{22}^X} & 0 \\ 0 & 0 & c_{66}^X \end{bmatrix} = \begin{bmatrix} c_{11}^X - \frac{(c_{13}^X)^2}{c_{33}^X} & c_{12}^X - \frac{c_{13}^X c_{23}^X}{c_{33}^X} & 0 \\ c_{12}^X - \frac{c_{13}^X c_{23}^X}{c_{33}^X} & c_{22}^X - \frac{(c_{23}^X)^2}{c_{33}^X} & 0 \\ 0 & 0 & c_{66}^X \end{bmatrix} \quad 3.28$$

here, the superscript  $X$  denotes the material type, either piezoelectric ( $E$ ) or magnetostrictive ( $B$ ).

With using  $f$  represents the piezoelectric coupling tensor  $e_p$  or piezomagnetic coupling tensor  $h$ , and the  $g$  in the case of electrical conductivity  $\sigma$  or permittivity  $\varepsilon$ , the following relations are applicable in T-mode:

$$f = \begin{bmatrix} 0 & \overline{f_{31}} \\ 0 & \overline{f_{33}} \\ f_{15} & 0 \end{bmatrix} = \begin{bmatrix} 0 & f_{31} - \frac{f_{33} c_{13}^E}{c_{33}^E} \\ 0 & f_{31} - \frac{f_{33} c_{23}^E}{c_{33}^E} \\ f_{15} & 0 \end{bmatrix} \quad 3.29$$

$$g = \begin{bmatrix} \overline{g_{11}} & 0 \\ 0 & \overline{g_{33}} \end{bmatrix} = \begin{bmatrix} g_{11} - \frac{(f_{13})^2}{c_{33}^X} & 0 \\ 0 & g_{33} - \frac{(f_{23})^2}{c_{33}^X} \end{bmatrix} \quad 3.30$$

And for the L-mode (magnetization or electrical polarization in longitudinal direction), we obtained the tensors with 2D plane strain approximation, with the same calculation for the transformed coefficients inside. And they are rewritten as:

$$c^X = \begin{bmatrix} \overline{c_{22}^X} & \overline{c_{12}^X} & 0 \\ \overline{c_{12}^X} & \overline{c_{11}^X} & 0 \\ 0 & 0 & \overline{c_{66}^X} \end{bmatrix}, f = \begin{bmatrix} \overline{f_{33}} & 0 \\ \overline{f_{31}} & 0 \\ 0 & \overline{f_{15}} \end{bmatrix}, g = \begin{bmatrix} \overline{g_{33}} & 0 \\ 0 & \overline{g_{11}} \end{bmatrix} \quad 3.31$$

Moreover, the 2D study implies a simplification of the magnetic problem since only the normal component  $\mathbf{a}_z$  (perpendicular direction to the working xOy plane) of the magnetic vector potential  $\mathbf{a}$  is considered. In this case, the curl operator can be degenerated into a gradient operator:

$$\nabla \times = r^* \nabla, \quad \text{with} \quad r^* = \begin{bmatrix} 0 & -1 \\ 1 & 0 \end{bmatrix} \quad 3.32$$

Therefore:

$$\mathbf{B} = \nabla \times \mathbf{a} = r^* \nabla \mathbf{a} \quad 3.33$$

### 3.3.3 FE weak formulations

The Finite Element Method (FEM) is a computational technique that stands out in the realm of variational methods for its efficacy in providing approximate solutions to boundary value problems (BVPs) governed by partial differential equations. Its roots extend back to the 1940s [77], originating within the civil engineering discipline to address intricate structural analysis challenges. Today, FEM is prominently utilized across various fields, particularly for problems analyzed in the frequency domain.

The widespread preference for FEM as a problem-solving tool is due to two primary factors. Firstly, its remarkable adaptability allows it to handle diverse geometries and material inconsistencies without requiring changes in the formulation or computer code, ensuring exceptional geometric fidelity. Secondly, FEM offers the advantage of reduced computational burden due to the highly sparse and (or) banded structure of the resulting matrices. This combination of versatility and efficiency makes FEM a cornerstone technique in many scientific and engineering disciplines.

The Finite Element Method is designed to obtain approximate solutions for boundary value problems (BVPs) that are dictated by partial differential equations, the BVP is typically characterized as follows within a domain  $\Omega$ :

$$\mathcal{L}(p) = f \quad 3.34$$

where  $\mathcal{L}$  represents a partial differential operator,  $p$  is the unknown function of the problem that needs to be determined, and  $f$  denotes the known excitation functions associated with boundary conditions. Here, our study domain  $\Omega \subset \mathcal{R}^2$  (2D problems).

The Finite Element Method is commonly implemented using the weighted residuals approach, which begins by representing the unknown function as a linear blend of carefully selected basis functions. In the method of weighted residuals, the residual  $R$  of the partial differential equation is weighted by specific weight (or test) functions  $w$  and set to zero within the study domain  $\Omega$ :

$$\langle R, w \rangle = \int_{\Omega} w(\mathcal{L}(p) - f) d\Omega = 0 \quad 3.35$$

In addressing our ME problem, it's imperative to employ the weighted residual method for each equation of equilibrium. Initially, we began by substituting equation 3.25 into equation 3.24:

$$\begin{cases} \nabla \cdot (c\mathbf{S} - h^t\mathbf{B} - e_p^t\mathbf{E}) + \mathbf{f} - \rho_m \frac{\partial^2 \mathbf{u}}{\partial t^2} = 0 \\ \nabla \times (h\mathbf{S} + v^s\mathbf{B}) = 0 \\ \nabla \cdot (e_p\mathbf{S} + \varepsilon^s\mathbf{E}) = 0 \end{cases} \quad 3.36$$

Subsequently, we substituted the equation 3.26 that express the fields in terms of state variables into equation 3.36, resulting in:

$$\begin{cases} \nabla \cdot (c\mathcal{D}\mathbf{u} - h^t\nabla \times \mathbf{a} + e_p^t\nabla V) + \mathbf{f} - \rho_m \frac{\partial^2 \mathbf{u}}{\partial t^2} = 0 \\ \nabla \times (h\mathcal{D}\mathbf{u} + v^s\nabla \times \mathbf{a}) = 0 \\ \nabla \cdot (e_p\mathcal{D}\mathbf{u} - \varepsilon^s\nabla V) = 0 \end{cases} \quad 3.37$$

Then, by applying the variational principle and taking into account the relevant boundary conditions of the study domain  $\Omega$ , and equation 3.32 for the curl operator, we arrived at the finite element formulation as follows:

$$\begin{cases} \int_{\Omega} \mathcal{D}w(c\mathcal{D}\mathbf{u} - h^t r^* \nabla \mathbf{a} + e_p^t \nabla V - \rho_m \frac{\partial^2 \mathbf{u}}{\partial t^2}) d\Omega = \int_{\Omega} -w\mathbf{f} d\Omega \\ \int_{\Omega} \nabla \times w(h\mathcal{D}\mathbf{u} + v^s r^* \nabla \mathbf{a}) d\Omega = 0 \\ \int_{\Omega} \nabla w(e_p\mathcal{D}\mathbf{u} - \varepsilon^s \nabla V) d\Omega = 0 \end{cases} \quad 3.38$$

### 3.3.4 FEM discretization

During the pre-processing stage of FEM, the computational domain  $\Omega$  is discretized into smaller subdomains, labelled  $\Omega^e$ , with the superscript  $e$  indicating the  $e$ -th element in the mesh, and the number of these subdomains represents by  $n^e$ . This process of discretization allows for the local representation of the equation 3.35 within each individual element as:

$$\langle R^e, w_i^e \rangle = \int_{\Omega^e} w_i^e (\mathcal{L}(\sum_{j=1}^{n^e} N_j^e p_j^e) - f^e) d\Omega^e = 0 \quad 3.39$$

where the  $w_i^e$  represents the  $i$ -th weight function, with  $i$  ranges from 1 to  $n^e$ .

Using the Galerkin approach, where the weight functions  $w$  are chosen to be the basis functions  $N_i^e$ , so that  $w_i^e = N_i^e$ , equation 3.39 transforms as follows:

$$\sum_{j=1}^{n^e} p_j^e \int_{\Omega^e} N_i^e (\mathcal{L}(N_j^e)) d\Omega^e = \int_{\Omega^e} N_i^e f^e d\Omega^e \quad 3.40$$

Thus, the discretization of our ME problem begins by defining the unknown function as follows:

$$\begin{cases} \{\mathbf{u}\} = \sum_{j=1}^{n^e} N_j^e \{\mathbf{u}_j^e\} = N_u \bar{\mathbf{u}} \\ \{V\} = \sum_{j=1}^{n^e} N_j^e \{V_j^e\} = N_v \bar{V} \\ \{\mathbf{a}\} = \sum_{j=1}^{n^e} N_j^e \{\mathbf{a}_j^e\} = N_a \bar{\mathbf{a}} \end{cases} \quad 3.41$$

This discretization is accompanied by the Galerkin method, which involves selecting weight functions identical to the transposed basis functions, leading to the following discretized PDE's formulations:

$$\begin{cases} \int_{\Omega} \left( \mathcal{D}N_u^t c N_u \bar{\mathbf{u}} - \mathcal{D}N_u^t h^t r^* \nabla N_a \bar{\mathbf{a}} + \mathcal{D}N_u^t e^t \nabla N_v \bar{V} - N_u^t \rho_m \frac{\partial^2}{\partial t^2} (N_u \bar{\mathbf{u}}) \right) d\Omega = \int_{\Omega} N_u^t f d\Omega \\ \int_{\Omega} \left( (r^* \nabla N_a)^t h \mathcal{D}N_u \bar{\mathbf{u}} + (r^* \nabla N_a)^t v^s r^* \nabla N_a \bar{\mathbf{a}} \right) d\Omega = 0 \\ \int_{\Omega} \left( \nabla N_v^t e_p \mathcal{D}N_u \bar{\mathbf{u}} - \nabla N_v^t \varepsilon^s \nabla N_v \bar{V} \right) d\Omega = 0 \end{cases} \quad 3.42$$

By substituting  $G_u = \mathcal{D}N_u$ ,  $G_v = \nabla N_v$ ,  $G_a = r^* \nabla N_a$  and  $M = N_u$ , we could obtain the reduced form as:

$$\begin{cases} \int_{\Omega} \left( G_u^t c G_u \bar{\mathbf{u}} - G_u^t h^t G_a \bar{\mathbf{a}} + G_u^t e^t G_v \bar{V} - \frac{\partial^2}{\partial t^2} (M^t \rho_m M \bar{\mathbf{u}}) \right) d\Omega = \int_{\Omega} M^t f d\Omega \\ \int_{\Omega} \left( G_a^t h G_u \bar{\mathbf{u}} + G_a^t v^s G_a \bar{\mathbf{a}} \right) d\Omega = 0 \\ \int_{\Omega} \left( G_v^t e_p G_u \bar{\mathbf{u}} - G_v^t \varepsilon^s G_v \bar{V} \right) d\Omega = 0 \end{cases} \quad 3.43$$

### 3.3.5 ME problem in quasi-static regime

After the FEM discretization, the matrix system for our ME coupling problem in quasi-static regime can be written in a mechanical form:

$$[\mathbf{M}]\{\ddot{X}\} + [\mathbf{C}]\{\dot{X}\} + [\mathbf{K}]\{X\} = \{F\} \quad 3.44$$

with

$$[M] = \begin{bmatrix} M & 0 & 0 \\ 0 & 0 & 0 \\ 0 & 0 & 0 \end{bmatrix}, [C] = \begin{bmatrix} C_{uu} & 0 & 0 \\ 0 & 0 & 0 \\ 0 & 0 & 0 \end{bmatrix}, [K] = \begin{bmatrix} K_{uu} & K_{uv} & K_{ua} \\ K_{vu} & K_{vv} & K_{va} \\ K_{au} & K_{av} & K_{aa} \end{bmatrix} \quad 3.45$$

where  $[M]$  is the mass matrix,  $[C]$  is the damping matrix, and  $[K]$  is the stiffness matrix.  $K_{uv} = K_{vu}^t$ ,  $K_{ua} = K_{au}^t$ ,  $K_{va} = K_{av}^t$ , and  $C_{uu} = \alpha M + \beta K_{uu}$ , with  $\alpha$  and  $\beta$  are the Rayleigh's damping coefficients.

$$\begin{bmatrix} K_{uu} \\ K_{vv} \\ K_{aa} \end{bmatrix} = \sum_e \int_{\Omega} \begin{bmatrix} [G_u]^t c [G_u] \\ [G_v]^t \epsilon^S [G_v] \\ [G_a]^t \nu^S [G_a] \end{bmatrix} d\Omega \quad 3.46$$

$$\begin{bmatrix} K_{uv} \\ K_{ua} \end{bmatrix} = \sum_e \int_{\Omega} \begin{bmatrix} [G_u]^t e_p^t [G_v] \\ [G_u]^t h^t [G_a] \end{bmatrix} d\Omega$$

and the unknown vector  $\{X\}$  and excitation vector  $\{F\}$ :

$$\{X\} = \begin{bmatrix} \mathbf{u} \\ \bar{V} \\ \mathbf{a} \end{bmatrix}, \{F\} = \begin{bmatrix} \mathbf{f} \\ 0 \\ 0 \end{bmatrix} \quad 3.47$$

The Rayleigh's damping concerns the energy dissipation caused by mechanical vibrations of solid materials in fluid mediums, where  $\alpha$  is the mass multiplication factor and  $\beta$  is the stiffness multiplication factor. In the dynamic regime of the magneto-electric materials we study, mechanical vibrations are often accompanied by viscous damping. Therefore, we assume that the damping factor  $\alpha$  related to mass is zero and calculate  $\beta$  using the following equation [78].

$$\beta = \frac{1}{2\pi f_r Q_m} \quad 3.48$$

Where  $f_r$  is the resonant frequency,  $Q_m$  is the quality factor reflects the amount of energy loss at resonance. This quality factor cannot be derived through calculation alone; it requires analysis of the electrical impedance of the ME material we are studying, specifically by measuring the bandwidth at half-maximum of the electrical impedance resonance related to the studied resonance mode, and calculated as follows:

$$Q_m = \frac{f_r}{\Delta f} \quad 3.49$$

When the quality factors of the magnetostrictive material  $Q_{mag}$  and piezoelectric materials  $Q_{piezo}$  in the studied ME materials are known, we can also calculate the quality factor of the composite ME material directly as follows:

$$n \cong \frac{t_{mag}}{t_{piezo}} \quad 3.50$$

$$Q_m = \frac{Q_{mag}}{n} + \frac{Q_{piezo}}{1-n} \quad 3.51$$

where  $t_{mag}$  and  $t_{piezo}$  are the total thickness of magnetostrictive and piezoelectric materials respectively.

As shown in Figure 3.2, in the quasi-static regime of ME materials, the magnetic excitation field consists of a static field and a small dynamic harmonic field. Therefore, the study of the quasi-static regime can be divided into the static part and the harmonic (dynamic) part.

In the static part, as illustrated in Figure 3.4, all the derivative-related terms in equation 3.44 become zero, since their derivatives are zero. In contrast, in the dynamic regime, we retain the full expression of equation 3.44. To analyze the nonlinear behavior in the static regime, we employ a piecewise procedure, whereas in the dynamic part, we adopt a linear approximation. This means that at any given bias point, within the range of variation of the small dynamic magnetic field, the magnetostrictive coupling is assumed to be linear.

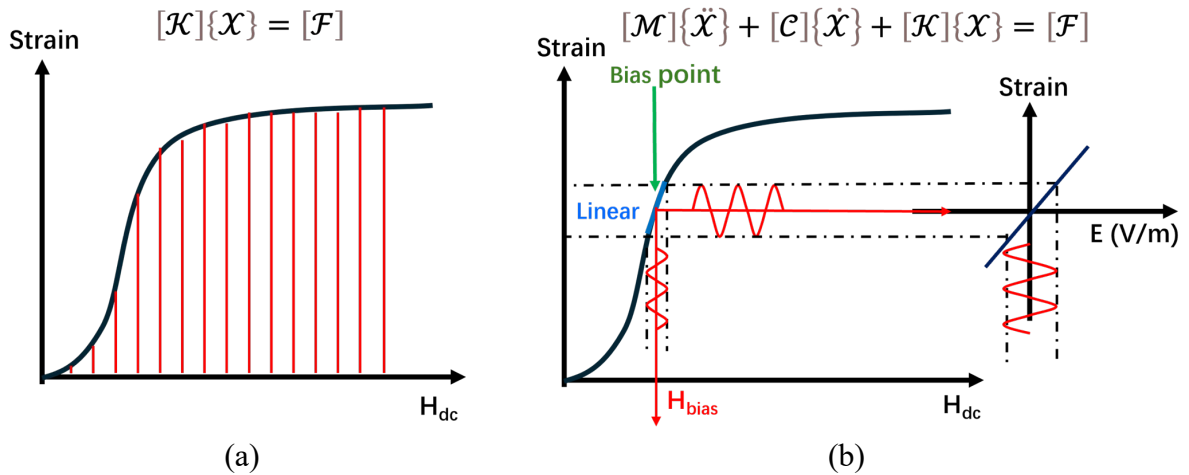


Figure 3.4. In quasi-static regime: (a) Static part solved using a piecewise procedure. (b) Dynamic part approximated with a linear assumption around the magnetic bias point, within the nonlinear magnetostrictive coupling.

### 3.3.6 Boundary conditions

To condition the problem, boundary conditions have been imposed on the Multiphysics problem as illustrated in Figure 3.5.

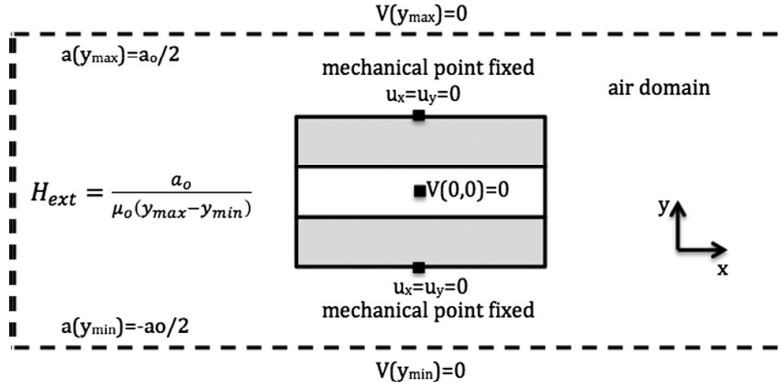


Figure 3.5. boundary conditions in study domain

➤ Mechanical Boundary Conditions

To immobilize the ME composite, two fixed points with no mechanical displacement, are set by Dirichlet conditions  $u_y = u_z = 0$  at the center of both external surfaces of each magnetostrictive layer (see Figure 3.5).

➤ Magnetic Boundary Conditions:

The external magnetic excitation field  $H_{ext}$  is composed of a small dynamic harmonic signal  $H_{ac}$  around a static magnetic polarization field  $H_{dc}$ . These are modelled separately in the finite element model in static and dynamic regimes. The static field  $H_{dc}$  allows for the determination of the nonlinear material characteristics and integrated as  $K_{ua}$  and  $K_{aa}$  in the stiffness matrix [K], which are then used in the dynamic regime. The magnetic excitation is represented by the excitation vector  $\{F\}$  considering non-homogeneous Dirichlet conditions:  $\mathbf{a}(\Gamma_{y,max}) = a_0/2$ , and  $\mathbf{a}(\Gamma_{y,min}) = -a_0/2$  as found on Figure 3.5.

The magnetic flux  $\Phi$  is given by:

$$\Phi = \iint_{\Omega} \mathbf{B} \cdot d\mathbf{S} = \int_{\Omega} \nabla \times \mathbf{a} \cdot d\mathbf{S} = \oint_{\partial\Omega} \mathbf{a} \cdot d\mathbf{l} \quad 3.52$$

which can be reduced to 2D such that  $a_0 = B_0 \Delta_z$ , with  $\Delta_z = z_{max} - z_{min}$ , and  $B_0 = \mu_0 H_{ac}$ , where  $\mu_0$  is the permeability of free space.

➤ Electrical Boundary Conditions:

To guarantee the solution for the electrical potential  $\{V\}$ , the Dirichlet condition  $V(\Gamma_{y,min}) = V(\Gamma_{y,max}) = 0$  is applied.

➤ Electrical impedance load

Since the piezoelectric layer acts as a dielectric, there are no free charges within it; all charges are confined to the electrodes. The electric current  $I$  supplied to the impedance load is the time derivative of the total electric charge  $Q$ , expressed as  $I = \dot{Q}$ , in harmonic regime, the current can be rewritten as  $I = j\omega Q$ .

As shown in Figure 3.1, the electrical voltage of the electrical impedance load  $Z_{load}$  can obtain from:

$$V = Z_{load}I = j\omega Z_{load}Q \quad 3.53$$

And then, this relationship can be directly obtained by discretizing a simple electrical equation as follows:

$$\{V\} K_{vq} - Z_{load}\dot{Q} = 0 \quad 3.54$$

Here,  $K_{vq}$  is an incident vector where the elements are assigned values of 1 or -1, depending on the node's association with either the top or bottom electrode, and 0 otherwise. In this process, both electrodes have been treated as equipotential, and this assignment of values using  $K_{vq}$  indicates that both electrodes share the same degree of freedom, and the charge  $Q$  becomes the unknown in our ME problem.

### 3.3.7 Nonlinear problem in quasi-static regime

#### 3.3.7.a. Nonlinear magnetoelastic model

The static magnetoelastic (ME) problem involves the complex interaction between the nonlinear characteristics of ferromagnetic materials like permeability and piezomagnetic coefficients and the linear properties of piezoelectric materials, including permittivity and piezoelectric coefficients. Aiming to reduce the complexity, an anhysteretic magnetoelastic model for Ni is suggested, relying on the magnetization  $M(H, T)$  formulated through a modified Langevin function as outlined in [79], [80], together with the magnetostriction strain  $\lambda(H, T)$ :

$$H_e = H + \alpha_d M + \frac{9T\lambda_s}{2\mu_0 M_s^2} M \quad 3.55$$

$$M(H, T) = M_s \mathcal{L}\left(\frac{H_e}{a}\right) = M_s \left[ \coth\left(\frac{H_e}{a}\right) - \frac{a}{H_e} \right] \quad 3.56$$

$$\lambda(H, T) = \begin{cases} \frac{3}{2} \lambda_s \left( \frac{M(H, T)}{M_s} \right)^2, & \text{while } T \neq 0 \\ \lambda_s \left( \frac{M(H, T)}{M_s} \right)^2, & \text{while } T = 0 \end{cases} \quad 3.57$$

where  $H$  the static magnetic field,  $a$  mean field parameter, characterizes the shape of the anhysteretic curve,  $\alpha_d$  inter-domain coupling coefficient, and  $T$  representing an equivalent uniaxial applied stress or an uniaxial residual stress after the fabrication of the material.  $\lambda_s$  magnetostriction saturation,  $\mu_0$  free space permeability,  $M_s$  magnetization saturation.

When a magnetic excitation field is applied along the longitudinal direction of the magnetostrictive materials (direction 3 in their local coordinate, refer to Figure 3.1). the piezomagnetic tensor and permeability can be expressed as follows [81]:

$$d_m = \begin{bmatrix} 0 & 0 & 0 & 0 & d_{15}^m & 0 \\ 0 & 0 & 0 & d_{24}^m & 0 & 0 \\ d_{31}^m & d_{32}^m & d_{33}^m & 0 & 0 & 0 \end{bmatrix} \quad 3.58$$

$$\mu^T = \begin{bmatrix} \mu_{11}^T & 0 & 0 \\ 0 & \mu_{22}^T & 0 \\ 0 & 0 & \mu_{33}^T \end{bmatrix} \quad 3.59$$

We can predict these two parameter tensors using the above anhyseretic magnetoelastic model, with the relation below:

$$\mu_{11}^T = \mu_{22}^T = \mu_{33}^T = \mu_0 + \partial_H M(H, T) \quad 3.60$$

$$2d_{31}^m = 2d_{32}^m = d_{33}^m = \partial_H \lambda(H, T) \quad 3.61$$

The shear piezomagnetic coefficients in piezomagnetic tensor cannot be predicted directly, the study in [82] have highlighted that accurately identifying this coefficient is complex. To address this complexity, a method has been proposed to estimate the coefficient by examining the relationship between shear direction and directional cosines of magnetization, symbolized as  $m_i = M_i/M_s$ . For isotropic magnetoelastic materials, the shear strain  $S_{13}$  can be obtained with this relation detailed in [83], [84]:

$$S_{13} = 3\lambda_s m_1 m_3 \quad 3.62$$

with  $m_3 = M(H, T)/M_s$ .

Considering the differential of shear strain in response to  $H_1$ :

$$\frac{dS_{13}}{dH_1} = \frac{\partial S_{13}}{\partial m_1} \frac{\partial m_1}{dH_1} + \frac{\partial S_{13}}{\partial m_3} \frac{\partial m_3}{dH_1} \quad 3.63$$

here,  $\frac{\partial S_{13}}{\partial m_1} = 3\lambda_s m_3$ , and  $\partial m_3/\partial H_1$  when  $\frac{\partial m_1}{\partial H_1} = \frac{dM_1}{dH_1} = \chi_1/M_s$ , with the  $\chi_1$  the magnetic susceptibility coefficient in direction 1.

Finally, the shear piezomagnetic coefficient can be obtained as follows:

$$\begin{aligned}
d_{15}^m &= 2\partial_{H_1} S_{13} \Big|_T \\
&= 2 \frac{dS_{13}}{dm_1} \frac{dm_1}{dH_1} \\
&= 6\lambda_s m_3 \frac{\chi_1}{M_s} \\
&= 6\lambda_s \frac{M(H, T)}{M_s^2} \left( \frac{\mu_{33}^T}{\mu_0} - 1 \right)
\end{aligned}$$

The piezomagnetic tensor  $h$  and reluctivity tensor  $\nu^S$  used in our FEM formulation can be obtained using the equation 3.12, and then transformed in 2D tensor form using the plane stress approximation as shown in equation 3.29 and 3.30, and integrated in equation 3.46 for our simulation, Thus the ME response related to the static magnetic field  $H_{dc}$  is derived from the the curves of  $M(H, T)$  and  $\lambda(H, T)$  predicted in the proposed anhysteretic magnetoelastic model.

### 3.3.7.b. Nonlinear piecewise procedure in FEM

Figure 3.6 illustrates the workflow of the nonlinear piecewise procedure used in the 2D finite element method (FEM) simulation to model the nonlinear behavior of the magnetostrictive phase in a magnetoelectric transducer.

This procedure starts with the application of the external magnetic field and mechanical stress. In each iteration, the magnetostrictive coefficients and the permeability tensor are calculated using the previously described nonlinear magnetoelastic model. Subsequently, various mechanical and magnetic properties are computed. A Jacobian matrix is then constructed to represent the interaction between mechanical compliance, magnetic reluctance, and coupling effects within the material. This matrix is employed in the FEM resolution step, where the stiffness matrix and external forces are used to determine the state variables of the material, including displacement, strain, and magnetic flux.

Once the FEM equations are solved, the simulation updates parameters such as the changes in magnetic field, stress, and other state variables. This iterative process allows for the continuous adjustment of the magnetic field and stress at each step, providing a detailed representation of the nonlinear interactions within the magnetostrictive phase.

Through this nonlinear piecewise procedure, the simulation not only captures the nonlinear response of the magnetostrictive material as described by the magnetoelastic model, but also reflects the non-uniform changes in magnetic field, stress, and other parameters within each element of the finite element mesh during each iteration, as shown in Figure 3.7.

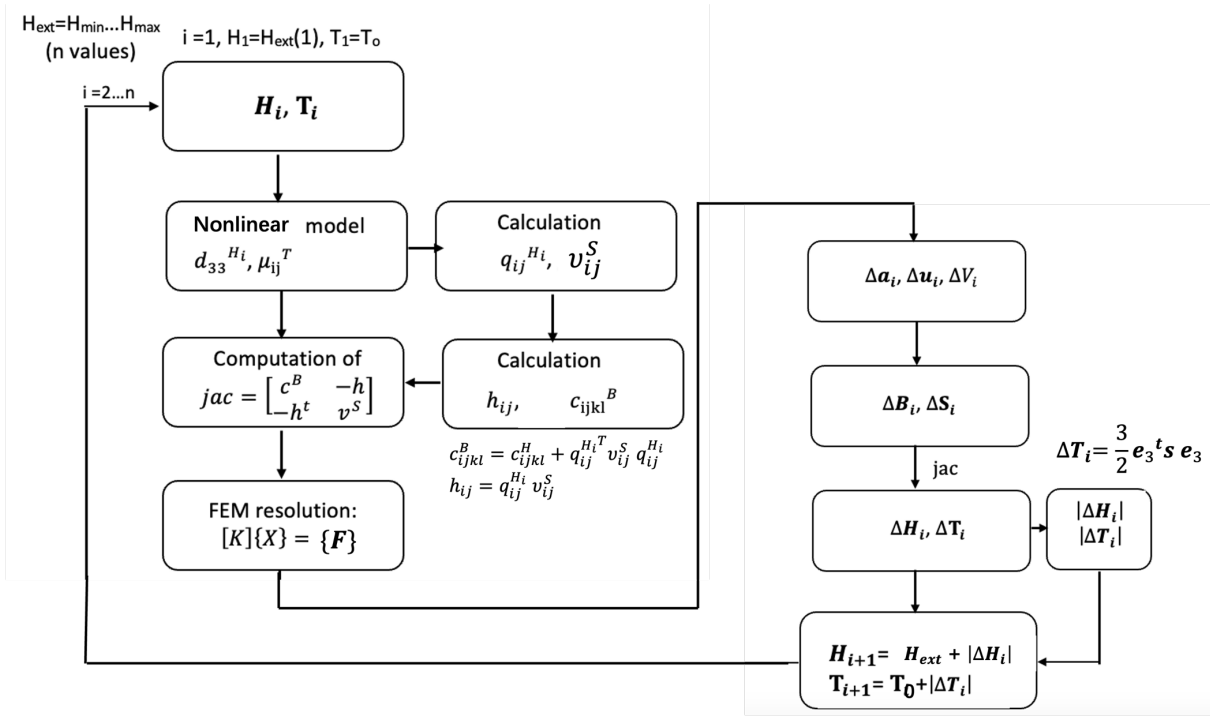


Figure 3.6. Workflow of the nonlinear piecewise procedure used in the 2D FEM simulation for modeling the nonlinear behavior of the magnetostrictive phase in a magnetoelectric transducer.

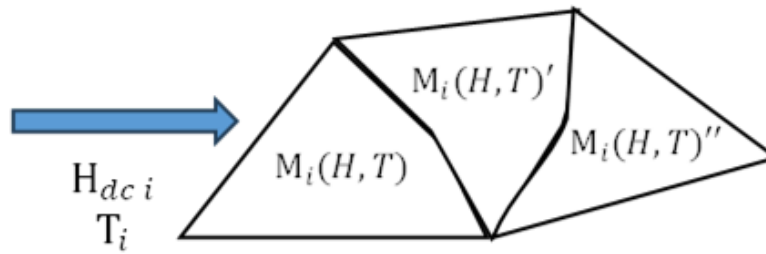


Figure 3.7. Nonlinear distribution of magnetization in piecewise procedure.

### 3.3.8 ME problem in Harmonic regime

The typical form for the FEM calculation is a linear form as  $[K]\{X\}=\{F\}$ , we can rewrite Equation 3.44 in the following form in harmonic regime, with  $\partial/\partial t = j\omega$ :

$$[K] = \begin{bmatrix} K_{uu} + j\omega C_{uu} - \omega^2 M & K_{uv} & 0 & K_{ua} \\ K_{vu} & K_{vv} & K_{vq} & 0 \\ 0 & K_{qv} & -j\omega Z_{load} & 0 \\ K_{au} & 0 & 0 & K_{aa} \end{bmatrix} \quad 3.65$$

And the unknown vector  $\{X\}$  and excitation vector  $\{F\}$  can be expressed:

$$\{X\} = \begin{bmatrix} \mathbf{u} \\ V \\ Q \\ \mathbf{a}_z \end{bmatrix}, \{F\} = \begin{bmatrix} 0 \\ 0 \\ \mathbf{a}_0 \end{bmatrix} \quad 3.66$$

### 3.3.9 Prediction of deliverable electric power

When using a ME material in energy transduction, our primary focus is on how much electric power the ME transducer can provide under a dynamic magnetic excitation of 1 Oe in RMS. Therefore, power estimation of ME materials through our FEM modeling is crucial.

We use a straightforward method corresponding to the classical approach of determining the internal impedance of a ME transducer based on Thevenin's theorem. The internal impedance can be calculated using the voltage in open-circuit condition and the current in short-circuit condition.

$$Z_{\text{internal}} = \frac{V_{\text{open-circuit}}}{I_{\text{short-circuit}}} \quad 3.67$$

In our modeling in harmonic regime, we have considered the electrical impedance load. Thus, we can simulate within two electrical impedance load conditions to estimate the internal impedance: Firstly, by defining a very high impedance load (1 M $\Omega$ ) as an open-circuit condition, the scalar voltage  $V$  in the unknown vector  $\{X\}$  can be calculated and taken as the open-circuit voltage  $V_{\text{open-circuit}}$ . Subsequently, by setting the impedance load to 0  $\Omega$ , we simulate the ME transducer in a short-circuit condition. The scalar electric charge  $Q$  in the unknown vector  $\{X\}$  is then calculated during the harmonic FEM calculations, and based on this relation  $I = j\omega Q$ , the short-circuit current  $I_{\text{short-circuit}}$  is calculated. We can obtain the  $Z_{\text{internal}}$  by the equation 3.67 by performing the above FEM calculations with two different impedance loads.

This model allows us to represent the ME transducer as an electric source, featuring an open-circuit voltage generator with internal resistance in series. In this simple model, we can examine how the deliverable electric power of our ME transducer under a harmonic regime with a dynamic excitation of 1 Oe in RMS varies with the electrical impedance load, and it is easy to demonstrate that the deliverable maximum power is obtained when the load matches the internal resistance:

$$P_{\text{opt}} = \frac{(V_{\text{OC}} / 2\sqrt{2})^2}{Z_{\text{internal}}} \quad 3.68$$

### 3.3.10 Shell element formulation for thin film structure

When ME composites are composed of thin and thick layers, the thickness ( $\delta = t_p$ ) of the magnetostrictive layer is typically much smaller than the dimensions of the piezoelectric layer [23], [24], [25], [85], which include its thickness ( $t_p$ ) and length ( $L_p$ ). When  $\delta/A < 10^{-3}$ , where  $A$  is the maximum between  $t_p$  and  $L_p$ , the traditional finite element modeling of such structures requires an extremely fine mesh, which can be time-consuming. To simplify this process, an

effective thin layer can be considered for the magnetostrictive layer and modeled using a line element. The nodes of the line element are duplicated, as shown in Figure 3.8, and we applied the gradient approximation proposed to degenerate the 3-node linear triangular element into a 2-node line element, as follows:

$$\text{grad}_L[N\phi] = \frac{1}{2} \frac{\partial}{\partial x} \left( \sum_{i=1}^2 N_i^0 \langle \phi_i \rangle \right) \mathbf{e}_x + \frac{1}{\delta} \left( \sum_{i=1}^2 N_i^0 [\phi_i] \right) \mathbf{e}_y \quad 3.69$$

where  $\langle \phi_i \rangle = \phi_i^+ + \phi_i^-$  and  $[\phi_i] = \phi_i^+ - \phi_i^-$  are, respectively, the weighted average and the jump of unknown variable  $\phi_i$  along and across the thickness  $\delta$ . The annotations  $\phi_i^+$  and  $\phi_i^-$  represent the nodal values of  $\phi_i$  on both sides of the thin layer element and  $N_i^0$  is the shape function for 2-node line element.

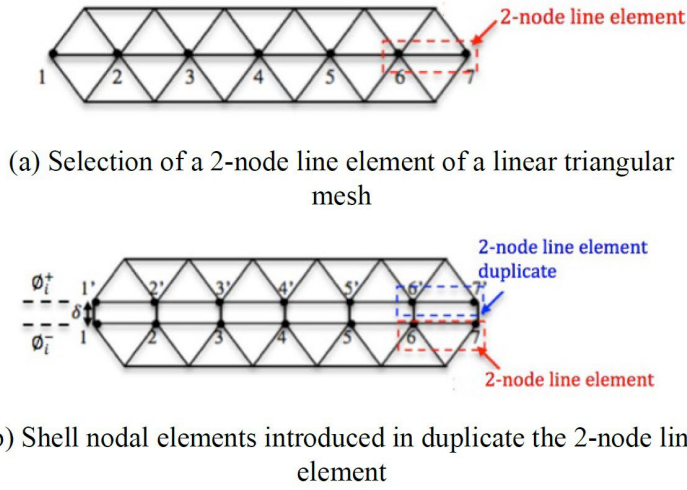


Figure 3.8. illustration of the approach for considering thin film structure using shell element

As a result, we modeled the effective thin layer using symmetric 4-node elements (Q4 element), which approximate the unknown variables  $\mathbf{u} = \{u_x, u_y\}$ ,  $V$ , and  $a_z$  using shape functions 3.71 and 3.72. These functions are obtained by degenerating the 2-node line element.

$$\begin{cases} \{\mathbf{u}\} = N_{ui}^0 \mathbf{u}_i \\ \{V\} = N_i^0 V_i \\ \{\mathbf{a}_z\} = N_i^0 a_{zi} \end{cases} \quad 3.70$$

with the shape functions

$$N_{ui}^0 = \begin{bmatrix} N_1' & 0 & N_2' & 0 & 0 & 0 & 0 & 0 \\ 0 & N_1' & 0 & N_2' & 0 & 0 & 0 & 0 \\ 0 & 0 & 0 & 0 & N_1' & 0 & N_2' & 0 \\ 0 & 0 & 0 & 0 & 0 & N_1' & 0 & N_2' \end{bmatrix} \quad 3.71$$

$$N_i^0 = \begin{bmatrix} N_1' & 0 & N_2' & 0 \\ 0 & N_1' & 0 & N_2' \end{bmatrix} \quad 3.72$$

where  $N_1' = 1 - \frac{x}{L_e}$ , and  $N_2' = \frac{x}{L_e}$  with  $L_e$  denotes the length of the 2-node line element.

And the unknown variables are decomposed as:

$$\begin{cases} u_i = \{u_{x1}^+, u_{y1}^+, u_{x2}^+, u_{y2}^+, u_{x1}^-, u_{y1}^-, u_{x2}^-, u_{y2}^-\} \\ V_i = \{V_1^+, V_1^-, V_2^+, V_2^-\} \\ a_{zi} = \{a_1^+, a_1^-, a_2^+, a_2^-\} \end{cases} \quad 3.73$$

The degenerate gradient operators  $G_u^{shell}$ ,  $G_V^{shell}$  and  $G_a^{shell}$  can be rewritten as:

$$\begin{aligned} G_u^{shell} &= D' [N_{ui}^0] \\ G_V^{shell} &= G_a^{shell} = \text{grad}_L [N_i^0] \end{aligned} \quad 3.74$$

with

$$D' = \begin{bmatrix} \frac{1}{2} \frac{\partial}{\partial x} & 0 & \frac{1}{2} \frac{\partial}{\partial x} & 0 \\ 0 & \frac{1}{\delta} & 0 & -\frac{1}{\delta} \\ \frac{1}{\delta} & \frac{1}{2} \frac{\partial}{\partial x} & -\frac{1}{\delta} & \frac{1}{2} \frac{\partial}{\partial x} \end{bmatrix} \quad 3.75$$

$$\text{grad}_L = \begin{bmatrix} \frac{1}{2} \frac{\partial}{\partial x} & \frac{1}{2} \frac{\partial}{\partial x} \\ \frac{1}{\delta} & -\frac{1}{\delta} \end{bmatrix} \quad 3.76$$

By assuming that the reluctivity and elasticity are constant along the thickness of the thin magnetostrictive structure, it can be integrated into the previous modeling for quasi-static and harmonic regimes using the following submatrices in this following, to substitute the elements for in the stiffness matrix [K] in the ME system matrix:

$$\left\{ \begin{array}{l} K_{aa}^{shell} = \delta v_{11} \sum_e \int_{l_e} [G_a^{shell}]^T [G_a^{shell}] dl \\ K_{uu}^{shell} = \delta c_{11} \sum_e \int_{l_e} [G_u^{shell}]^T [G_u^{shell}] dl \\ K_{ua}^{shell} = \delta \sum_e \int_{l_e} [G_u^{shell}]^T h^t [G_a^{shell}] dl \\ M_{shell} = \delta \rho_m \sum_e \int_{l_e} [N_{ui}^0]^T h^t [N_{ui}^0] dl \end{array} \right. \quad 3.77$$

where  $l_e$  denotes the line element domain. And  $v_{11}$  and  $c_{11}$  are the coefficients of reluctivity and stiffness tensors, respectively, along the thickness direction in the local coordinate of magnetostrictive layers as shown in Figure 3.1.

### 3.4 Simulation of RF sputtered ME transducers

#### 3.4.1 Properties of nonlinear magnetostrictive coupling

Polycrystalline nickel typically has a face-centered cubic (FCC) crystal structure, belong to the  $m\bar{3}m$  point group. From the stress magnetization form of magnetostrictive coupling mentioned in the previous chapter, the following components are essential: the compliance tensor  $s_H$  the piezomagnetic tensor  $d^m$  and the relative permeability tensor  $\mu^T$ , and can be written as:

$$s^H = \begin{bmatrix} s_{11}^H & s_{12}^H & s_{12}^H & 0 & 0 & 0 \\ s_{12}^H & s_{11}^H & s_{12}^H & 0 & 0 & 0 \\ s_{12}^H & s_{12}^H & s_{11}^H & 0 & 0 & 0 \\ 0 & 0 & 0 & s_{44}^H & 0 & 0 \\ 0 & 0 & 0 & 0 & s_{44}^H & 0 \\ 0 & 0 & 0 & 0 & 0 & s_{44}^H \end{bmatrix} \quad 3.78$$

$$\mu^T = \begin{bmatrix} \mu_{33}^T & 0 & 0 \\ 0 & \mu_{33}^T & 0 \\ 0 & 0 & \mu_{33}^T \end{bmatrix} \quad 3.79$$

And when the magnetic excitation is applied longitudinally, the piezomagnetic tensor can be written as aforementioned in equation 3.58.

The values of nickel compliance coefficient are shown in Table 3.1. As shown in Figure 3.9, based on the magnetization measurements from a single layer of nickel material peeled from one magnetoelectric material sample, we have adjusted the parameters within the magnetoelastic model with a condition  $T = 0$ . This allowed us to predict the anhysteretic magnetic curve with a good correlation to the actual measurements. Subsequently, our predictions of the permeability and piezomagnetic tensors are presented in Figure 3.10.

Table 3.1. compliance properties of nickel material [86].

material	$s_{11}$ ( $10^{-12}\text{m}^2/\text{N}$ )	$s_{12}$ ( $10^{-12}\text{m}^2/\text{N}$ )	$s_{44}$ ( $10^{-12}\text{m}^2/\text{N}$ )
Ni	6.3	-2.3	7.6

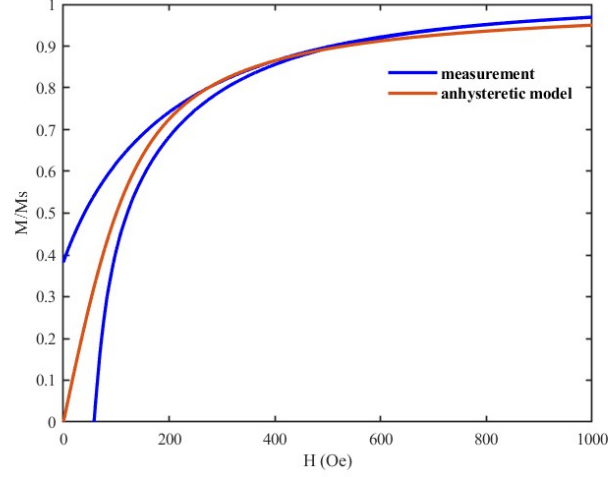


Figure 3.9. Normalized magnetic measured M-H curve (blue) of nickel in a Ni/PZT-5H/Ni ME sample and the magneto-elastic model (red).

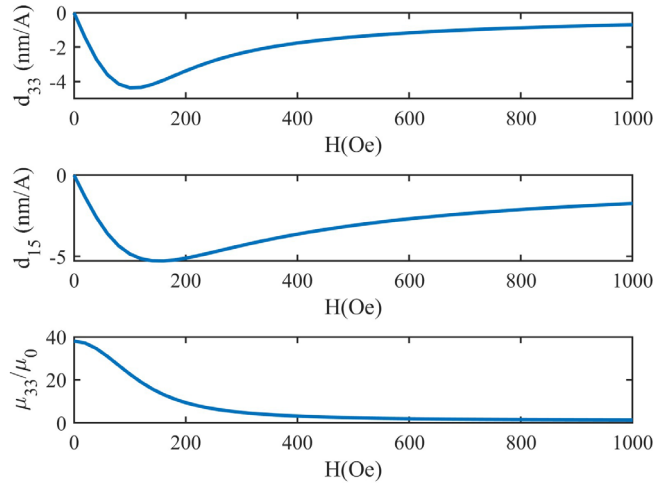


Figure 3.10. Prediction of piezomagnetic  $d_{33}^m$ ,  $d_{15}^m$  and relative permeability  $\mu_{33}^T/\mu_0$  incremental coefficients of the Ni.

According to Figure 3.10, the value of the static magnetic field  $H$  at the minimum of  $d_{33}^m$  corresponds to the optimal magnetic bias point, where the piezomagnetic coupling effect is optimal.

### 3.4.2 Properties of linear piezoelectric coupling

At room temperature,  $\text{LiNbO}_3$  is identified as a monocrystalline ferroelectric material, categorically belonging to the  $3m$  point group. From the strain-charge form of piezoelectric

coupling mentioned in the previous chapter, the following components are necessary: the compliance tensor  $s^E$  the piezoelectric tensor  $d_p$  and the relative permittivity tensor  $\epsilon^T$ , and can be written as:

$$s^E = \begin{bmatrix} s_{11}^E & s_{12}^E & s_{13}^E & s_{14}^E & 0 & 0 \\ s_{12}^E & s_{11}^E & s_{13}^E & -s_{14}^E & 0 & 0 \\ s_{13}^E & s_{13}^E & s_{33}^E & 0 & 0 & 0 \\ s_{14}^E & -s_{14}^E & 0 & s_{44}^H & 0 & 0 \\ 0 & 0 & 0 & 0 & s_{44}^H & 2s_{14}^E \\ 0 & 0 & 0 & 0 & 2s_{14}^E & 2(s_{11}^E - s_{12}^E) \end{bmatrix} \quad 3.80$$

$$d_p = \begin{bmatrix} 0 & 0 & 0 & 0 & d_{15} & -2d_{22} \\ -d_{22} & d_{22} & 0 & d_{15} & 0 & 0 \\ d_{31} & d_{31} & d_{33} & 0 & 0 & 0 \end{bmatrix} \quad 3.81$$

$$\epsilon^T = \begin{bmatrix} \epsilon_{11}^T & 0 & 0 \\ 0 & \epsilon_{11}^T & 0 \\ 0 & 0 & \epsilon_{33}^T \end{bmatrix} \quad 3.82$$

Table 3.2. Physical properties of piezoelectric coupling for Z-Cut LiNbO<sub>3</sub> [57].

Material	Relative permittivity		Compliance ( $10^{-12} \text{m}^2/\text{N}$ )						Piezoelectric coefficients (pC/N)			
	$\epsilon_{11,r}^T$	$\epsilon_{33,r}^T$	$s_{11}^E$	$s_{12}^E$	$s_{13}^E$	$s_{14}^E$	$s_{33}^E$	$s_{44}^E$	$d_{15}$	$d_{22}$	$d_{31}$	$d_{33}$
LiNbO <sub>3</sub>	84	30	5.78	-1.01	-1.47	-1.02	5.02	17.0	68	21	-1	6.2

To study the characteristics of different cuts of LiNbO<sub>3</sub>, coordinate transformations are applied through counterclockwise rotation, which combine bond strain transformation [87]:

The rotation of an angle  $\phi$  around the X-axis:

$$A_x = \begin{bmatrix} 1 & 0 & 0 \\ 0 & \cos \phi & \sin \phi \\ 0 & -\sin \phi & \cos \phi \end{bmatrix} \quad 3.83$$

The rotation of an angle  $\theta$  around the Y-axis:

$$A_y = \begin{bmatrix} \cos \theta & 0 & -\sin \theta \\ 0 & 1 & 0 \\ \sin \theta & 0 & \cos \theta \end{bmatrix} \quad 3.84$$

The rotation of an angle  $\psi$  around the Z-axis:

$$A_z = \begin{bmatrix} \cos \psi & \sin \psi & 0 \\ -\sin \psi & \cos \psi & 0 \\ 0 & 0 & 1 \end{bmatrix} \quad 3.85$$

For example, if a rotation of an angle  $\psi$  around the Z-axis is applied, a frame (X', Y', Z') is obtained with  $Z = Z'$ , and then, applying a rotation of an angle  $\theta$  around the X'-axis, a frame (X'', Y'', Z'') is obtained with  $X'' = X'$ . The transformation notations for the dielectric (second order), piezoelectric (third order), and compliance (fourth order) tensors after these two rotations are:

$$\begin{cases} \epsilon' = A_x \cdot A_z \cdot \epsilon \cdot A_z^t \cdot A_x^t \\ d'_m = A_x \cdot A_z \cdot d_m \cdot A_z^t \cdot A_x^t \\ S^{E'} = N_x \cdot N_z \cdot S^E \cdot N_z^t \cdot N_x^t \end{cases} \quad 3.86$$

where  $N$  represent the bond strain transformation matrix:

$$N = \begin{bmatrix} a_{11}^2 & a_{12}^2 & a_{13}^2 & a_{12}a_{13} & a_{13}a_{11} & a_{11}a_{12} \\ a_{21}^2 & a_{22}^2 & a_{23}^2 & a_{22}a_{23} & a_{23}a_{21} & a_{21}a_{22} \\ a_{31}^2 & a_{32}^2 & a_{33}^2 & a_{32}a_{33} & a_{33}a_{31} & a_{31}a_{32} \\ 2a_{21}a_{31} & 2a_{22}a_{32} & 2a_{23}a_{33} & a_{22}a_{33} + a_{23}a_{32} & a_{23}a_{31} + a_{21}a_{33} & a_{21}a_{32} + a_{22}a_{31} \\ 2a_{11}a_{31} & 2a_{12}a_{32} & 2a_{13}a_{33} & a_{12}a_{33} + a_{13}a_{32} & a_{13}a_{31} + a_{11}a_{33} & a_{11}a_{32} + a_{12}a_{31} \\ 2a_{11}a_{21} & 2a_{12}a_{22} & 2a_{13}a_{23} & a_{12}a_{23} + a_{13}a_{22} & a_{13}a_{21} + a_{11}a_{23} & a_{11}a_{22} + a_{12}a_{21} \end{bmatrix} \quad 3.87$$

here  $a_{ij} = A_{ij}$ .

For instance, to acquire a  $\theta$  Y-cut LiNbO<sub>3</sub>, denoted as (YXl)  $\theta$ , a single counterclockwise rotation of angle  $\phi = \pi/2 + \theta$  around the X-axis is required, starting from a Z-cut LiNbO<sub>3</sub>.

### 3.5 Simulation using 2D FEM

To investigate the magnetoelectric (ME) response of sample 6 (Ni/163° Y-cut LiNbO<sub>3</sub>/Ni) discussed in the previous chapter, we first employed 2D FEM and applied a small signal condition of  $H_{ac} = 1$  Oe and a resistive impedance load  $Z_{load} = 1$  M $\Omega$ . This load was connected between the nickel films serving as electrodes in each ME transducer sample, simulating the output voltage in an open-circuit condition. The meshing of this simulation is shown in Figure 3.11. Due to the extremely small thickness of the nickel film relative to its length, accurately meshing this thin-film structure proved to be highly challenging. We experimented with various mesh densities, but the resulting simulated ME responses differed significantly from the experimental measurements. However, the illustration of the magnetic, mechanical, and electric fields, as shown in Figure 3.12, matched our expectations in both direction and distribution.

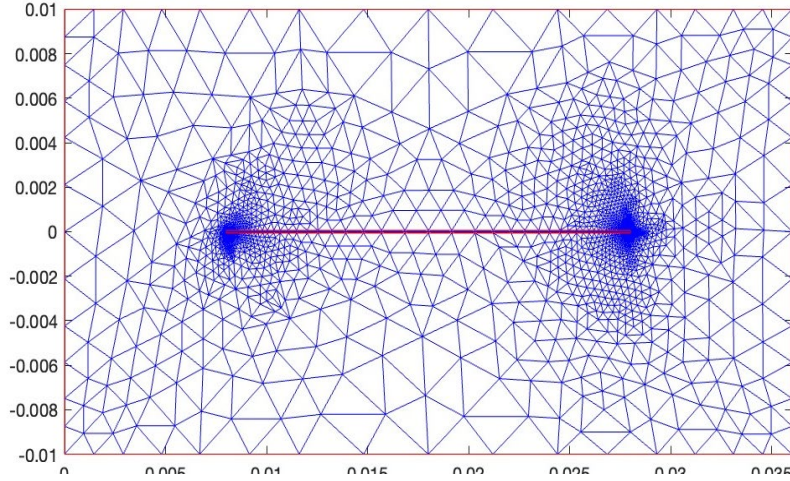


Figure 3.11. Finite element mesh of sample 6 in the 2D FEM model.

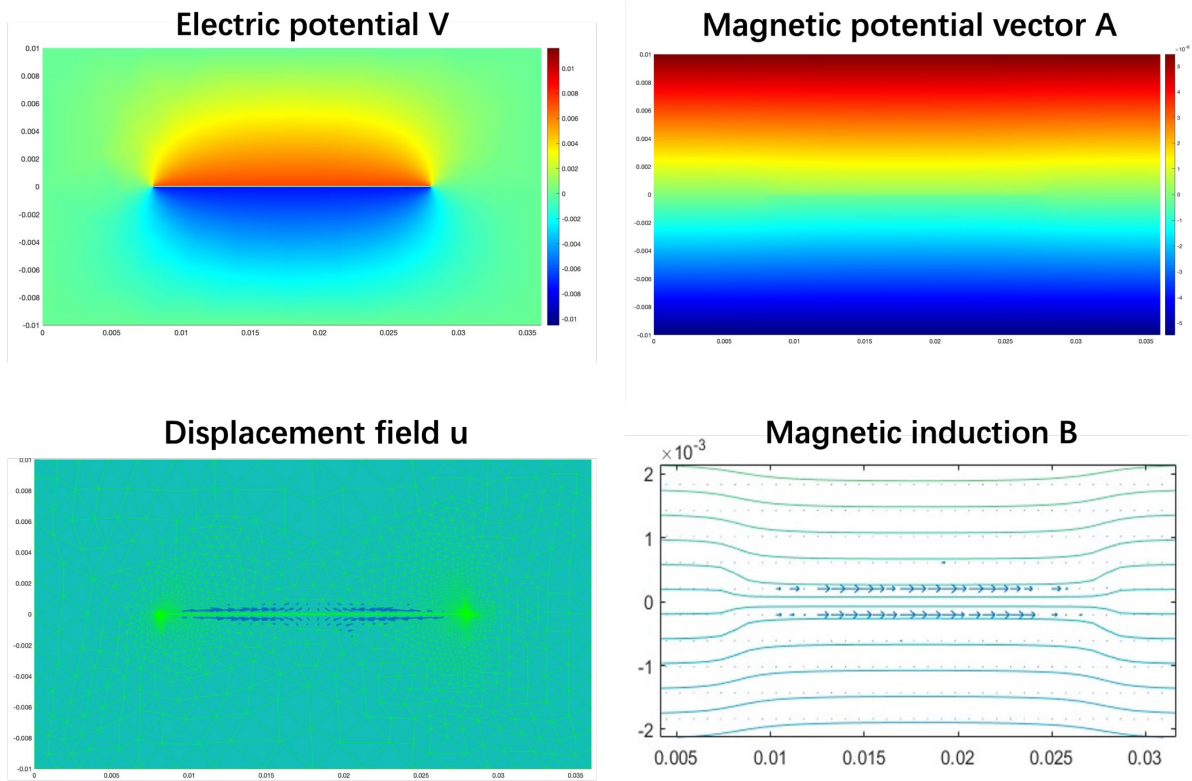


Figure 3.12. Distributions of electric potential  $V$ , magnetic potential vector  $A$ , mechanical displacement field  $u$ , and the lines and orientation of the magnetic induction  $B$  in the 2D FEM simulation.

To improve the accuracy of the simulation, we tried different mesh partitioning methods, but each method still showed discrepancies compared to the measured results. Therefore, we considered using shell elements in the FEM modeling to better capture the characteristics of the magnetostrictive thin-film structure. This approach helped reduce the influence of mesh quality on the calculated ME coefficients and enhanced simulation efficiency and stability.

While using shell elements to model the magnetostrictive phase, we modified the gradient operators within the FEM framework. This change meant that we could not directly derive

variations in magnetic induction and strain or retrieve changes in the magnetic field and stress using the Jacobian matrix in the nonlinear piecewise procedure. To address this issue, we first simulated the differences in magnetostrictive coupling in a 2D FEM model without using shell elements, both with and without the nonlinear piecewise procedure. The comparison is shown in Figure 3.13. We found that the results of both methods were quite similar in the initial region, including the curve descending to its minimum point, with significant differences emerging only after the minimum was passed. Based on this observation, when using shell elements to model the magnetostrictive phase in a thin-film structure in later simulations, we directly adopted the magnetoelastic model to uniformly consider the nonlinear magnetostrictive coupling across all mesh elements.

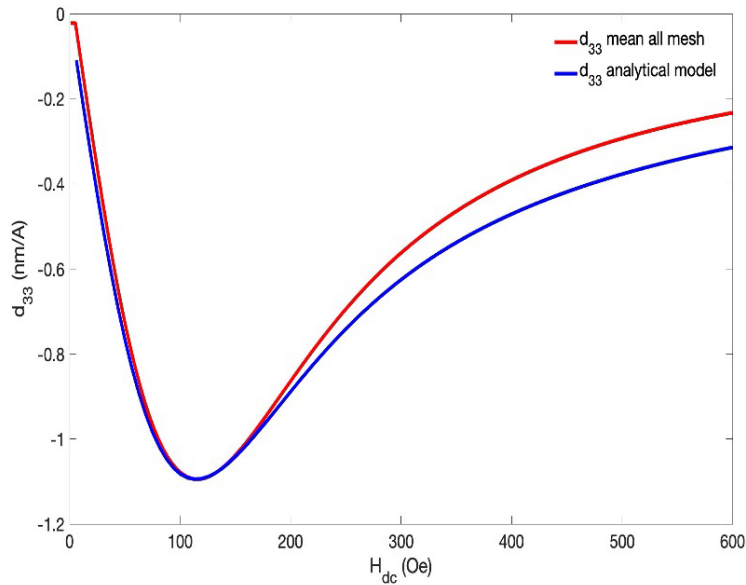


Figure 3.13. Comparison of the evolution of the magnetostrictive coupling factor with and without the nonlinear piecewise procedure.

Subsequently, we conducted simulation calculations using two ME transducer samples with a similar dimension but different piezoelectric substrates: sample 6 (Ni/163° Y-cut LiNbO<sub>3</sub>/Ni) and sample 15 (Ni/PZT-5H/Ni) were chosen. The simulations based on our FEM modeling detailed previously were executed with a small signal application of  $H_{ac} = 1$  Oe and a resistive impedance load  $Z_{load} = 1$  M $\Omega$ , connected between the Ni films serving as electrodes in each ME transducer sample, to simulate the output voltage as in an open-circuit condition, as the same condition when we measured the output voltage  $V$  in our ME coefficient measurements. It is imperative to highlight that all parameter tensors associated with LiNbO<sub>3</sub> originate from conducting a  $(90 + 163)^\circ$  counterclockwise rotation about the X-axis from the parameter tensors of Z-cut LiNbO<sub>3</sub>. The parameter values for the PZT-5H piezoelectric ceramic are detailed in the Annex.

Although our nickel films were deposited on different piezoelectric materials under the same RF sputtering setup for all samples, the qualities of the Ni films among the samples are not similar. For example, Ni films generated on samples 2 and 5, both of which have the same LiNbO<sub>3</sub> cut (36° Y-cut), have differences between their own isolated Ni films, as shown in Figure 3.14. Thus, it is not possible to directly estimate the magnetic behaviors on different piezoelectric substrates by estimating a residual stress related to a cooling condition ( $\Delta T \sim -100$

K), and then derive the magnetic behavior with our proposed magnetoelastic model  $M(H, T)$  by an estimated residual stress.

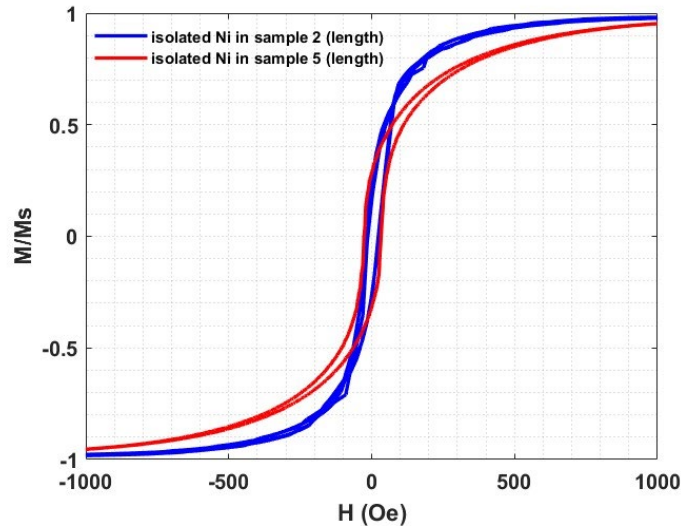


Figure 3.14. ME curves of the freestanding nickel films in samples 2 and 5.

We adjusted our nonlinear anhysteretic curve derived from our proposed magnetoelastic model without considering the stress dependence, to fit the magnetic curve of the Ni in trilayer Ni/PZT-5H/Ni transducer, as shown in Figure 3.10, and we could predict the piezomagnetic coupling tensor  $d^m$  and permeability  $\mu^T = \mu_0 \mu_r^T$  of the nickel films in sample 15, and import this properties of the nickel needed in the quasi-static regime as a function of the static magnetic field  $H_{dc}$ . As shown in Figure 3.15, our proposed FEM analysis demonstrates a good congruence between the magnetoelectric coefficients derived from both static and dynamic regimes for sample 15, corroborated by experimental measurements and simulations utilizing the predicted piezomagnetic and permeability curves. For sample 6, the nonlinear anhysteretic curve from our magnetoelastic model was also recalibrated based on its magnetic hysteresis measurements. Subsequent modifications to the piezomagnetic and permeability tensors in the proposed magnetoelastic model led to congruent alignment between the simulations and experimental observations, as depicted in Figure 3.16.

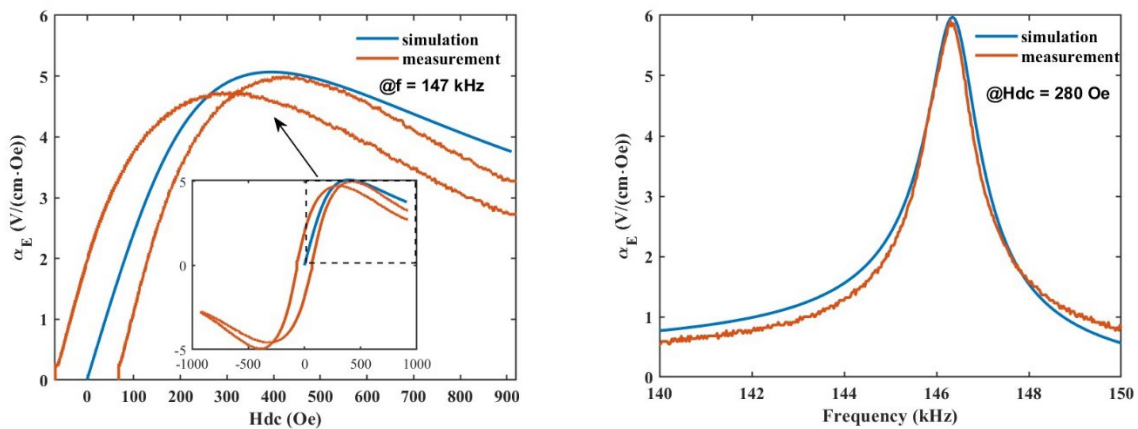


Figure 3.15. Comparison of ME coefficient responses in quasi-static (a) and dynamic (b) regimes of Ni/PZT-5H/Ni.

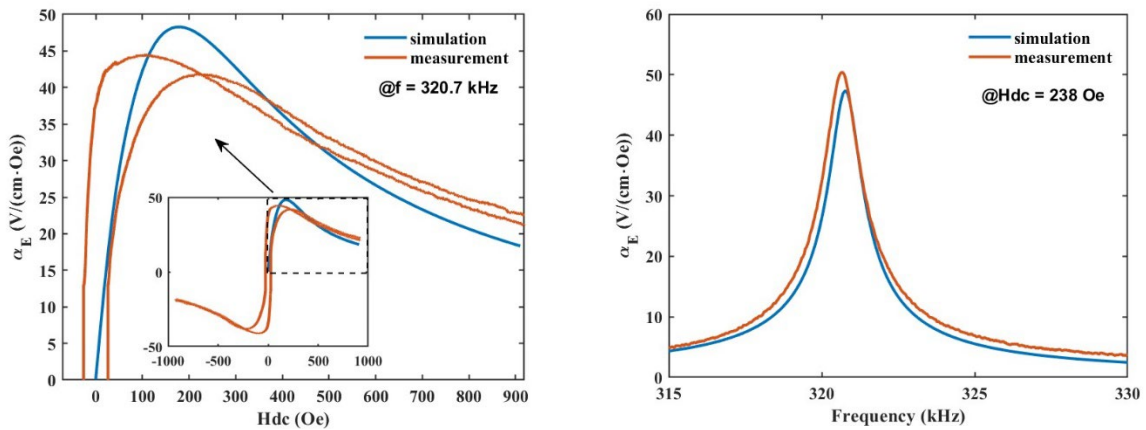


Figure 3.16. Comparison of ME coefficient responses in quasi-static (a) and dynamic (b) regimes of Ni/163° Y-cut LiNbO<sub>3</sub>/Ni

Through our FEM modeling, we are also able to predict the deliverable electric power for these two ME transducer types. As shown in Figure 3.17, at a frequency of 147 kHz for our sample 15, we achieve an optimal deliverable electric power when the external electrical impedance is 9.91 k $\Omega$ , which matches the internal impedance calculated in our FEM model. As shown in Figure 3.18, according to the electrical impedance measurements of sample, the maximum impedance value at its first longitudinal resonance is approximately 1.45 k $\Omega$ , which is significantly lower than the values obtained in our simulations. This indicates that our FEM model overestimates the impedance of this sample. However, the maximum deliverable electric power values between the simulation results and the actual measurements are not significantly different.

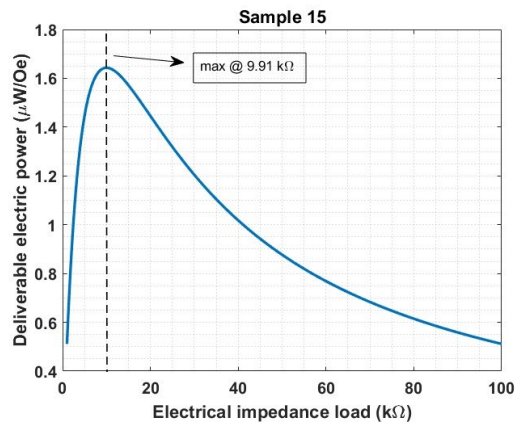


Figure 3.17. Simulation of deliverable electric power for sample 15.

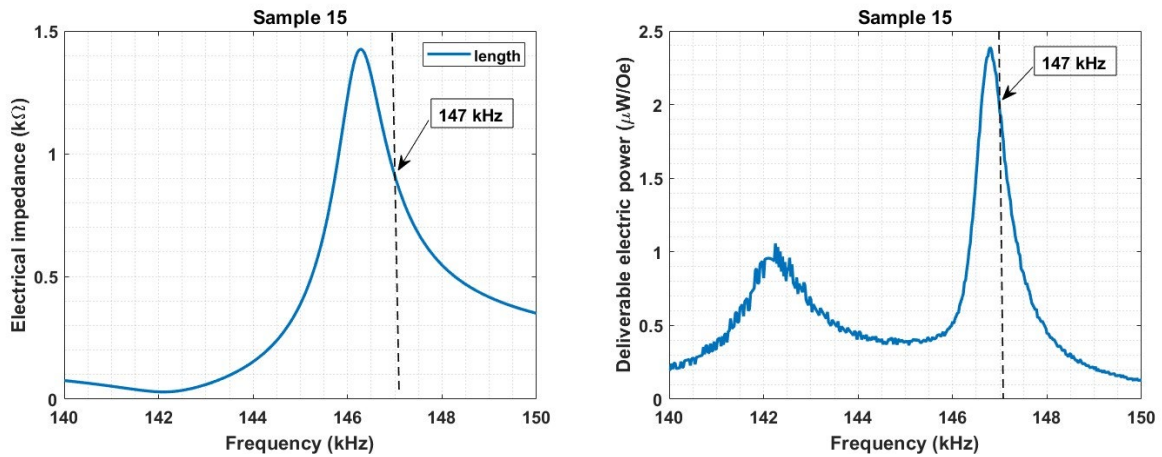


Figure 3.18. (a) Electrical impedance and (b) deliverable electric power estimate by the measurements for sample 15

In Figure 3.19, we see that for sample 6, an optimal deliverable electric power is achieved when the external electrical impedance is  $35\text{k}\Omega$ , which is within the range of electrical impedance measurements shown in Figure 3.20. Our simulations at a frequency of  $320.7\text{ kHz}$  for sample 6 resulted in an internal impedance also equal to  $35\text{ k}\Omega$ . Subsequent measurements of the electrical impedance of sample 6 in figure 8 showed that its impedance at  $320.7\text{ kHz}$  was a quarter of the value obtained in our simulations, explaining why our estimated maximum deliverable electric power for sample 6 is more than ten times smaller than the actual.

Although the electric power values predicted by our FE modeling have some differences from the actual measurements, they are sufficient to provide a rough reference range for material design considerations. It is worth noting that the ME and electrical impedance resonances of each ME transducer are easily influenced by external mechanical losses during the measurement, such as the mechanical fixing method applied during sample assembly, which can cause the ME transducer's ME resonance and electrical impedance resonance to differ from those in our idealized simulations, leading to discrepancies between the final simulation results and the measurements.

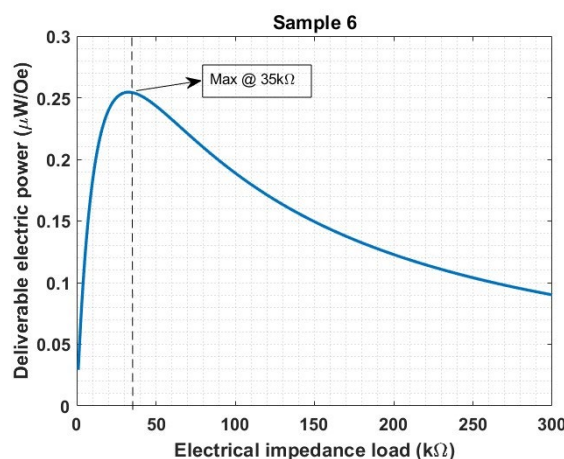


Figure 3.19. Simulation of deliverable electric power for sample 6

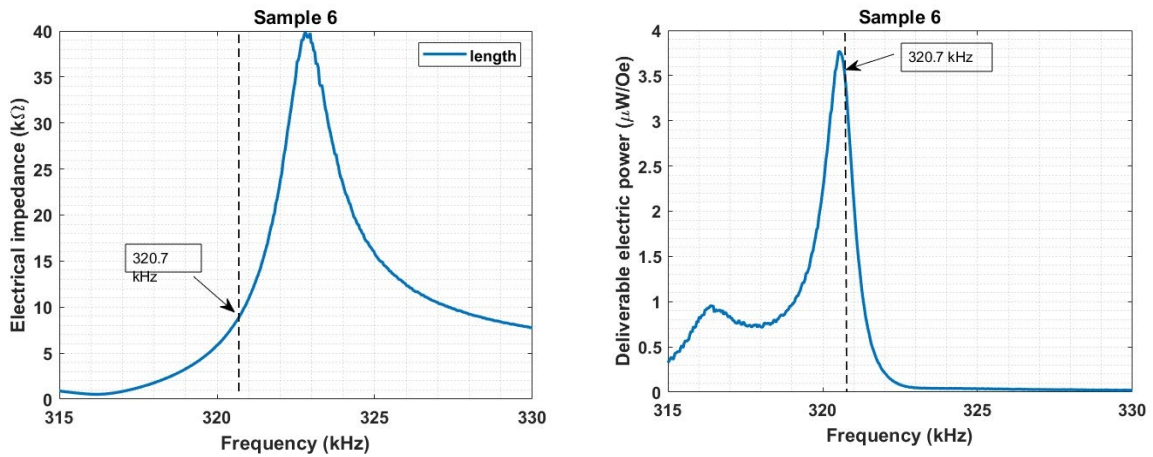


Figure 3.20. (a) Electrical impedance and (b) deliverable electric power estimate by the measurements for sample 6

### 3.6 Conclusion

This chapter focuses on the FE modeling of ME materials, primarily using 2D finite element models. Initially, the chapter introduces the laminate ME composites studied, along with their working conditions. It then explores the quasi-static and dynamic (harmonic) regimes of ME behavior.

Given that the magnetostrictive phase in the studied materials has a thin film structure, we employ 2D FE modeling with shell elements to account for this geometry, effectively reducing computational complexity. In addition, by using a simplified magnetoelastic model to simulate the nonlinear magnetostrictive coupling, we achieve a balance between accuracy and computational efficiency. The validity and robustness of the model were verified through comparisons with experimental data under various quasi-static and dynamic conditions.

In conclusion, the model successfully simulates the direct ME coupling effects in our studied ME composites and serves as a useful tool for future design optimization.

## Conclusion and perspective

The work undertaken in this thesis revolves around the study of the impact of fabrication process of ferromagnetic nickel films on various cuts of  $\text{LiNbO}_3$  and different piezoelectric materials such as PZT-5H using RF sputtering. Our focus has been on the fabrication of ME transducers through this manufacturing technique, which can generate residual stress related to thermal expansion at the interfaces between two different media upon cooling to room temperature after fabrication. This stress alters the in-plane magnetic behavior of the growth Nickel, leading to the desired self-biased ME behavior. This allows for energy transduction using only dynamic magnetic excitation without a static magnetic field bias, achieving remarkable piezomagnetic coupling in the ferromagnetic phase and thus an effective ME response without the need of bias.

In the first chapter, we introduced magnetoelectric (ME) materials and their magnetoelectric effects, and categorized them into two types based on their properties: intrinsic ME materials and extrinsic ME materials. In this thesis work, the property of extrinsic ME materials is exploited for wireless power transmission in medical application. Compared to traditional methods using coils and microwave transmission, the transducer based on ME materials are more suitable for biomedical implantable devices because they are smaller in size and the frequency range of the magnetic field excitation makes it possible to penetrate the human body while complying with exposure regulations, providing sufficient energy for implantable electronic devices. Furthermore, in recent studies, self-biased ME materials have shown remarkable remanent ME response compared to their ME response at optimal magnetic bias. Therefore, these self-biased ME materials are more suitable for biomedical implantable applications, as they can eliminate the need for a permanent magnet to generate a static magnetic bias or a Helmholtz coil, which typically generates several hundred Oe outside the human body. We have also discussed the different types of self-biased ME materials.

In the second chapter, we first provided a brief introduction to all measurement directions and the equipment used. We then examine the first batch of Ni/ $\text{LiNbO}_3$ /Ni samples to observe similarities and differences in ME behavior in the length direction among them, conducting studies on the texture of the ferromagnetic nickel materials grown by XRD. Following this, we investigated their magnetic behaviors. Through continuous setups and validations, we demonstrated that the self-biased ME behavior observed in the Ni/  $\text{LiNbO}_3$ /Ni samples is closely related to negative residual stress in the nickel material. We also attempted to predict theoretical properties of different  $\text{LiNbO}_3$  Y-cuts based on the properties of Z-cut  $\text{LiNbO}_3$ , and tried to validate them through comparison. However, due to the limitations of the RF sputtering technique (the thickness of nickel films grown is between 32-35  $\mu\text{m}$ , causing the nickel film's surface not to exhibit its metallic luster but rather a burnt black appearance), the thickness of nickel is fixed at 10  $\mu\text{m}$ . Due to the brittle nature of  $\text{LiNbO}_3$ , these different  $\text{LiNbO}_3$  Y-cut substrates are set at 500  $\mu\text{m}$ . The small thickness ratio of the ME transducer leads to a very weak self-biased ME response, mostly displaying asymmetric behavior. We also attempted to increase the thickness of the nickel films through electrodeposition. But during our first trials, we were unable to establish the correct conditions for electrodeposition on our ME transducer samples, causing the existing nickel films to detach from the piezoelectric substrate during the process. This technique is currently being optimized, in particular through the work of a Master's student. We later tried enhancing our self-biased behavior through annealing, which showed the greatest ME response at zero  $H_{dc}$ , but this had little effect on the already self-biased ME materials. In the final part of this chapter, using the finite element model from the previous chapter, we successfully simulated the ME behavior of two ME transducer samples with the

same thickness of nickel film but different piezoelectric materials under the ME L-T mode in both quasi-static and dynamic regimes.

The third chapter described our studies on the numerical modeling of a ME transducer using the FEM. In this transducer the ferromagnetic nickel films in thin structure are deposited on rectangular piezoelectric substrates in a sandwich structure. Nickel serves both as magnetostrictive material to respond to external magnetic field excitation, inducing strain and acting on the piezoelectric material, and as electrodes for the ME transducer due to its conductivity. This chapter mainly discussed their operation in the ME L-T mode. By employing constitutive laws and equilibrium equations for magnetostriction and piezoelectricity, we used the FEM to geometrically discretize the problem domain, ultimately creating an FE model representing the ME problems. Since the thickness dimension of our Nickel material in ME composite transducer is much smaller than the plane dimension of piezoelectric material, we used the shell element formulation to consider the magnetostrictive thin structure in the FE model, allowing the calculation to be accurate without significantly increasing computational time or suffering from poor mesh quality at material contact boundaries causing non-convergence in FE calculation. We also explained how to predict nickel properties from a nonlinear magnetoelastic materials model to obtain the piezomagnetic properties of nickel under each static magnetic field  $H_{dc}$  excitation, ultimately simulating the ME transducer containing Nickel in the quasi-static regime with  $H_{dc}$  variations. At the end of this chapter, we explained how to obtain the necessary properties for the corresponding monocrystalline cut by rotating piezoelectric properties tensors of the referenced Z-cut.

For further investigation of Ni/LiNbO<sub>3</sub>/Ni ME transducers, it is firstly necessary to standardize the assembly methods for these transducers. With different assembly methods and at different assembly moments, the mechanical damping effects acting on the samples can be altered.

This results in varied outcomes from the same sample when studied.

Therefore, we conducted repeated measurements on each sample and selected the optimal result to represent the final structure. Given the specification of small dimensions, ferromagnetic nickel and piezoelectric LiNbO<sub>3</sub> substrates are more suitable for encapsulation using wafer level packaging (WLP) commonly used in NEMS devices [88], [89], [90]. Thus, we can consider integrating and fixing the fabricated samples via the same WLP method in the future. This approach maximizes the control over the mechanical damping impact introduced during assembly and facilitates the comparison of performance between different materials. Additionally, due to the previously studied 500  $\mu\text{m}$  ME transducer samples showed weak self-biased responses primarily because of the disproportionate volume ratio between the nickel films and LiNbO<sub>3</sub> substrate, we can thicken the volume of nickel films produced by RF sputtering by employing electrodeposition, and use the annealing process to eliminate internal stresses generated during electrodeposition in the newly formed nickel materials after. This annealing treatment can strengthen the effect of residual stresses caused by thermal expansion between the nickel and the piezoelectric substrate at the contact surface, to strengthen the influence of this stress on the overall nickel material. In this way, we will study the impact of different nickel film thicknesses on self-biased ME performance while keeping the thickness of the piezoelectric substrate unchanged.

## Annex

Properties of PZT-5H piezoelectric material:

- Mass density:  $\rho_m = 7500 \text{ kg/m}^3$
- Stiffness tensor under constant electric field:

$$c^E = \begin{bmatrix} 127.21 & 80.21 & 84.67 & 0 & 0 & 0 \\ 80.21 & 127.21 & 84.67 & 0 & 0 & 0 \\ 84.67 & 84.67 & 117.44 & 0 & 0 & 0 \\ 0 & 0 & 0 & 22.9 & 0 & 0 \\ 0 & 0 & 0 & 0 & 22.9 & 0 \\ 0 & 0 & 0 & 0 & 0 & 23.47 \end{bmatrix} \text{ GPa}$$

- Piezoelectric coupling tensor:

$$e_p = \begin{bmatrix} 0 & 0 & 0 & 0 & 17.03 & 0 \\ 0 & 0 & 0 & 17.03 & 0 & 0 \\ -6.62 & -6.62 & 23.24 & 0 & 0 & 0 \end{bmatrix} \text{ C/m}^2$$

- Relative permittivity tensor under constant strain:

$$\mu_r^S = \begin{bmatrix} 1704.4 & 0 & 0 \\ 0 & 1704.4 & 0 \\ 0 & 0 & 1433.6 \end{bmatrix}$$

## References

- [1] J. P. Joule, "On a new class of magnetic forces," *Ann. Electr. Magn. Chem*, vol. 8, no. 1842, pp. 219–224, 1842.
- [2] E. Villari, "Change of magnetization by tension and by electric current Annal," *Phys. Chem., Lpz*, vol. 128, p. 1865, 1865.
- [3] P. G. Saiz, R. Fernández De Luis, A. Lasheras, M. I. Arriortua, and A. C. Lopes, "Magnetoelastic Resonance Sensors: Principles, Applications, and Perspectives," *ACS Sens.*, vol. 7, no. 5, pp. 1248–1268, May 2022, doi: 10.1021/acssensors.2c00032.
- [4] Y. K. Fetisov and G. Srinivasan, "Nonlinear magnetoelectric effects in layered multiferroic composites," *Journal of Applied Physics*, vol. 135, no. 2, p. 024102, Jan. 2024, doi: 10.1063/5.0183351.
- [5] E. A. Lindgren *et al.*, "Development of Terfenol-D transducer material," *Journal of Applied Physics*, vol. 83, no. 11, pp. 7282–7284, Jun. 1998, doi: 10.1063/1.367618.
- [6] W. Huang, Z. Zhang, P. Guo, X. Feng, and L. Weng, "Measurement and calculation for high frequency magnetic losses of Terfenol-D alloy rod under coupled stress and DC bias fields," *AIP Advances*, vol. 13, no. 11, p. 115013, Nov. 2023, doi: 10.1063/5.0175744.
- [7] J. P. Domann, C. M. Loeffler, B. E. Martin, and G. P. Carman, "High strain-rate magnetoelasticity in Galfenol," *Journal of Applied Physics*, vol. 118, no. 12, p. 123904, Sep. 2015, doi: 10.1063/1.4930891.
- [8] J. K. Lee, H. M. Seung, C. I. Park, J. K. Lee, D. H. Lim, and Y. Y. Kim, "Magnetostrictive patch sensor system for battery-less real-time measurement of torsional vibrations of rotating shafts," *Journal of Sound and Vibration*, vol. 414, pp. 245–258, Feb. 2018, doi: 10.1016/j.jsv.2017.11.023.
- [9] A. G. Olabi and A. Grunwald, "Design and Application of Magnetostrictive 'MS' Materials," p. 30.
- [10] J. Curie and P. Curie, "Sur l'électricité polaire dans les cristaux hémiedries à faces inclinées, CR Séances Acad," *Sci., Paris*, pp. 91–294, 1880.
- [11] G. Lippmann, "Principe de la conservation de l'électricité, ou second principe de la théorie des phénomènes électriques," *J. Phys. Theor. Appl.*, vol. 10, no. 1, pp. 381–394, 1881.
- [12] H. Wei *et al.*, "An overview of lead-free piezoelectric materials and devices," *Journal of Materials Chemistry C*, vol. 6, no. 46, pp. 12446–12467, 2018.
- [13] W. G. Cady, *Piezoelectricity: An introduction to the theory and applications of electromechanical phenomena in crystals*. McGraw-Hill, 1946.
- [14] J. Rödel, W. Jo, K. T. P. Seifert, E. Anton, T. Granzow, and D. Damjanovic, "Perspective on the Development of Lead-free Piezoceramics," *Journal of the American Ceramic Society*, vol. 92, no. 6, pp. 1153–1177, Jun. 2009, doi: 10.1111/j.1551-2916.2009.03061.x.
- [15] X. Gao *et al.*, "Piezoelectric Actuators and Motors: Materials, Designs, and Applications," *Adv Materials Technologies*, vol. 5, no. 1, p. 1900716, Jan. 2020, doi: 10.1002/admt.201900716.
- [16] M. Kim, M. Hoegen, J. Dugundji, and B. L. Wardle, "Modeling and experimental verification of proof mass effects on vibration energy harvester performance," *Smart Materials and Structures*, vol. 19, no. 4, p. 045023, 2010.
- [17] F. Rigo, M. Migliorini, and A. Pozzebon, "Piezoelectric Sensors as Energy Harvesters for Ultra Low-Power IoT Applications," *Sensors*, vol. 24, no. 8, p. 2587, Apr. 2024, doi: 10.3390/s24082587.

- [18] E. Brusa, A. Carrera, and C. Delprete, “A Review of Piezoelectric Energy Harvesting: Materials, Design, and Readout Circuits,” *Actuators*, vol. 12, no. 12, p. 457, Dec. 2023, doi: 10.3390/act12120457.
- [19] N. Sezer and M. Koç, “A comprehensive review on the state-of-the-art of piezoelectric energy harvesting,” *Nano Energy*, vol. 80, p. 105567, Feb. 2021, doi: 10.1016/j.nanoen.2020.105567.
- [20] L. D. Landau, J. S. Bell, M. J. Kearsley, L. P. Pitaevskii, E. M. Lifshitz, and J. B. Sykes, *Electrodynamics of continuous media*, vol. 8. elsevier, 2013. Accessed: May 07, 2024.
- [21] I. E. Dzyaloshinskii, “On the magneto-electrical effects in antiferromagnets,” *Soviet Physics JETP*, vol. 10, pp. 628–629, 1960.
- [22] J. Van Suchtelen, “Product properties: a new application of composite materials,” *Phillips Research Reports*, vol. 27, pp. 28–37, 1972.
- [23] D. R. Patil, A. Kumar, and J. Ryu, “Recent Progress in Devices Based on Magnetoelectric Composite Thin Films,” *Sensors*, vol. 21, no. 23, p. 8012, Nov. 2021, doi: 10.3390/s21238012.
- [24] J. Ma, J. Hu, Z. Li, and C. Nan, “Recent Progress in Multiferroic Magnetoelectric Composites: from Bulk to Thin Films,” *Advanced Materials*, vol. 23, no. 9, pp. 1062–1087, Mar. 2011, doi: 10.1002/adma.201003636.
- [25] X. Liang *et al.*, “A Review of Thin-Film Magnetoelastic Materials for Magnetoelectric Applications,” *Sensors*, vol. 20, no. 5, p. 1532, Mar. 2020, doi: 10.3390/s20051532.
- [26] S. Kopyl, R. Surmenev, M. Surmeneva, Y. Fetisov, and A. Kholkin, “Magnetoelectric effect: principles and applications in biology and medicine— a review,” *Materials Today Bio*, vol. 12, p. 100149, Sep. 2021, doi: 10.1016/j.mtbio.2021.100149.
- [27] C. M. Leung, J. Li, D. Viehland, and X. Zhuang, “A review on applications of magnetoelectric composites: from heterostructural uncooled magnetic sensors, energy harvesters to highly efficient power converters,” *J. Phys. D: Appl. Phys.*, vol. 51, no. 26, p. 263002, Jul. 2018, doi: 10.1088/1361-6463/aac60b.
- [28] N. A. Spaldin and R. Ramesh, “Advances in magnetoelectric multiferroics,” *Nature Mater*, vol. 18, no. 3, pp. 203–212, Mar. 2019, doi: 10.1038/s41563-018-0275-2.
- [29] X. Liang, H. Chen, and N. X. Sun, “Magnetoelectric materials and devices,” *APL Materials*, vol. 9, no. 4, p. 041114, Apr. 2021, doi: 10.1063/5.0044532.
- [30] N. Ortega, A. Kumar, J. F. Scott, and R. S. Katiyar, “Multifunctional magnetoelectric materials for device applications,” *J. Phys.: Condens. Matter*, vol. 27, no. 50, p. 504002, Dec. 2015, doi: 10.1088/0953-8984/27/50/504002.
- [31] Y. Cheng, B. Peng, Z. Hu, Z. Zhou, and M. Liu, “Recent development and status of magnetoelectric materials and devices,” *Physics Letters A*, vol. 382, no. 41, pp. 3018–3025, Oct. 2018, doi: 10.1016/j.physleta.2018.07.014.
- [32] O. Saha, B. D. Truong, and S. Roundy, “A review of wireless power transfer using magnetoelectric structures,” *Smart Mater. Struct.*, vol. 31, no. 11, p. 113001, Nov. 2022, doi: 10.1088/1361-665X/ac9166.
- [33] F. Narita and M. Fox, “A Review on Piezoelectric, Magnetostrictive, and Magnetoelectric Materials and Device Technologies for Energy Harvesting Applications,” *Adv Eng Mater*, vol. 20, no. 5, p. 1700743, May 2018, doi: 10.1002/adem.201700743.
- [34] S. K. Ghosh *et al.*, “Rollable Magnetoelectric Energy Harvester as a Wireless IoT Sensor,” *ACS Sustainable Chem. Eng.*, vol. 8, no. 2, pp. 864–873, Jan. 2020, doi: 10.1021/acssuschemeng.9b05058.
- [35] B. D. Truong and S. Roundy, “Experimentally validated model and power optimization of a magnetoelectric wireless power transfer system in free-free configuration,” *Smart Mater. Struct.*, vol. 29, no. 8, p. 085053, Aug. 2020, doi: 10.1088/1361-665X/ab90a2.

- [36] J. G. Wan, Z. Y. Li, Y. Wang, M. Zeng, G. H. Wang, and J.-M. Liu, "Strong flexural resonant magnetoelectric effect in Terfenol-D/epoxy-Pb(Zr,Ti)O<sub>3</sub> bilayer," *Applied Physics Letters*, vol. 86, no. 20, p. 202504, May 2005, doi: 10.1063/1.1935040.
- [37] T. Garg, L. M. Goyal, T. Garg, and L. M. Goyal, "Magnetoelectric Composites-Based Energy Harvesters," in *Novel Applications of Piezoelectric and Thermoelectric Materials*, IntechOpen, 2023. doi: 10.5772/intechopen.110875.
- [38] Y. Xiao, H.-M. Zhou, X.-W. Ou, and C. Li, "Resonant Magnetoelectric Effect with Strongly Nonlinear Magneto-Elastic Coupling in Magnetoelectric Laminate Composites," 2012.
- [39] Z. Chu, M. PourhosseiniAsl, and S. Dong, "Review of multi-layered magnetoelectric composite materials and devices applications," *J. Phys. D: Appl. Phys.*, vol. 51, no. 24, p. 243001, Jun. 2018, doi: 10.1088/1361-6463/aac29b.
- [40] F. T. Alrashdan, J. C. Chen, A. Singer, B. W. Avants, K. Yang, and J. T. Robinson, "Wearable wireless power systems for 'ME-BIT' magnetoelectric-powered bio implants," *J. Neural Eng.*, vol. 18, no. 4, p. 045011, Aug. 2021, doi: 10.1088/1741-2552/ac1178.
- [41] J. E. Woods *et al.*, "Miniature battery-free epidural cortical stimulators," *Sci. Adv.*, vol. 10, no. 15, p. eadn0858, Apr. 2024, doi: 10.1126/sciadv.adn0858.
- [42] Z. Yu *et al.*, "MagNI: A MagnetoElectrically Powered and Controlled Wireless Neurostimulating Implant," *IEEE Trans. Biomed. Circuits Syst.*, vol. 14, no. 6, pp. 1241–1252, Dec. 2020, doi: 10.1109/TBCAS.2020.3037862.
- [43] Y. Zhou, D. Maurya, Y. Yan, G. Srinivasan, E. Quandt, and S. Priya, "Self-Biased Magnetoelectric Composites: An Overview and Future Perspectives," *Energy Harvesting and Systems*, vol. 3, no. 1, pp. 1–42, Jan. 2016, doi: 10.1515/ehs-2015-0003.
- [44] J. Wu *et al.*, "Synthesis and room temperature four-state memory prototype of Sr<sub>3</sub>Co<sub>2</sub>Fe<sub>24</sub>O<sub>41</sub> multiferroics," *Applied Physics Letters*, vol. 101, no. 12, p. 122903, Sep. 2012, doi: 10.1063/1.4753973.
- [45] "Epitaxial BiFeO<sub>3</sub> Multiferroic Thin Film Heterostructures | Science." Accessed: Oct. 11, 2024. [Online]. Available: <https://www.science.org/doi/10.1126/science.1080615>
- [46] W. C. Liu *et al.*, "Magnetoelectric and dielectric relaxation properties of the high Curie temperature composite Sr<sub>1.9</sub>Ca<sub>0.1</sub>NaNb<sub>5</sub>O<sub>15</sub>-CoFe<sub>2</sub>O<sub>4</sub>," *J. Phys. D: Appl. Phys.*, vol. 41, no. 12, p. 125402, May 2008, doi: 10.1088/0022-3727/41/12/125402.
- [47] A. McDannald, M. Staruch, G. Sreenivasulu, C. Cantoni, G. Srinivasan, and M. Jain, "Magnetoelectric coupling in solution derived 3-0 type PbZr<sub>0.52</sub>Ti<sub>0.48</sub>O<sub>3</sub>:xCoFe<sub>2</sub>O<sub>4</sub> nanocomposite films," *Applied Physics Letters*, vol. 102, no. 12, p. 122905, Mar. 2013, doi: 10.1063/1.4799174.
- [48] Y. Zhou, S. Chul Yang, D. J. Apo, D. Maurya, and S. Priya, "Tunable self-biased magnetoelectric response in homogenous laminates," *Appl. Phys. Lett.*, vol. 101, no. 23, p. 232905, Dec. 2012, doi: 10.1063/1.4769365.
- [49] T. Zhang *et al.*, "A New Magnetoelectric Composite with Enhanced Magnetoelectric Coefficient and Lower Resonance Frequency," *Appl Compos Mater*, vol. 21, no. 4, pp. 579–590, Aug. 2014, doi: 10.1007/s10443-013-9344-5.
- [50] C. Lu *et al.*, "Zero-biased magnetoelectric composite Fe<sub>73.5</sub>Cu<sub>1</sub>Nb<sub>3</sub>Si<sub>13.5</sub>B<sub>9</sub>/Ni/Pb(Zr<sub>1-x</sub>Ti<sub>x</sub>)O<sub>3</sub> for current sensing," *Journal of Alloys and Compounds*, vol. 589, pp. 498–501, Mar. 2014, doi: 10.1016/j.jallcom.2013.12.038.
- [51] "Investigation of magnetostrictive/piezoelectric multilayer composite with a giant zero-biased magnetoelectric effect | Applied Physics A." Accessed: Oct. 11, 2024. [Online]. Available: <https://link.springer.com/article/10.1007/s00339-013-7557-y>
- [52] K. Malleron, A. Gensbittel, H. Talleb, and Z. Ren, "Experimental study of magnetoelectric transducers for power supply of small biomedical devices," *Microelectronics Journal*, p. in press, Feb. 2018, doi: 10.1016/j.mejo.2018.01.013.

- [53] N. Chidambaram, A. Mazzalai, D. Balma, and P. Murali, "Comparison of lead zirconate titanate thin films for microelectromechanical energy harvester with interdigitated and parallel plate electrodes," *IEEE transactions on ultrasonics, ferroelectrics, and frequency control*, vol. 60, no. 8, pp. 1564–1571, 2013.
- [54] N. C. Carville *et al.*, "Biocompatibility of ferroelectric lithium niobate and the influence of polarization charge on osteoblast proliferation and function," *Journal of Biomedical Materials Research Part A*, vol. 103, no. 8, pp. 2540–2548, 2015, doi: 10.1002/jbm.a.35390.
- [55] "ANSI/IEEE Std 176-1987 An American National Standard IEEE Standard on Piezoelectricity," p. 74.
- [56] A. Kawamata, H. Hosaka, and T. Morita, "Non-hysteresis and perfect linear piezoelectric performance of a multilayered lithium niobate actuator," *Sensors and Actuators A: Physical*, vol. 135, no. 2, pp. 782–786, Apr. 2007, doi: 10.1016/j.sna.2006.08.025.
- [57] A. W. Warner, M. Onoe, and G. A. Coquin, "Determination of Elastic and Piezoelectric Constants for Crystals in Class (3 *m*)," *The Journal of the Acoustical Society of America*, vol. 42, no. 6, pp. 1223–1231, Dec. 1967, doi: 10.1121/1.1910709.
- [58] J. I. Roscow, H. Pearce, H. Khanbareh, S. Kar-Narayan, and C. R. Bowen, "Modified energy harvesting figures of merit for stress- and strain-driven piezoelectric systems," *Eur. Phys. J. Spec. Top.*, vol. 228, no. 7, pp. 1537–1554, Aug. 2019, doi: 10.1140/epjst/e2019-800143-7.
- [59] T. Rödiger, A. Schönecker, and G. Gerlach, "A Survey on Piezoelectric Ceramics for Generator Applications," *Journal of the American Ceramic Society*, vol. 93, no. 4, pp. 901–912, Apr. 2010, doi: 10.1111/j.1551-2916.2010.03702.x.
- [60] K. Bi, Y. G. Wang, D. A. Pan, and W. Wu, "Large magnetoelectric effect in negative magnetostrictive/piezoelectric/positive magnetostrictive laminate composites with two resonance frequencies," *Scripta Materialia*, vol. 63, no. 6, pp. 589–592, Sep. 2010, doi: 10.1016/j.scriptamat.2010.06.003.
- [61] "Structural characterization of polycrystalline thin films by X-ray diffraction techniques | Journal of Materials Science: Materials in Electronics." Accessed: Oct. 11, 2024. [Online]. Available: <https://link.springer.com/article/10.1007/s10854-020-04998-w>
- [62] R. Stylianou, M. Tkadletz, N. Schalk, M. Penoy, C. Czettel, and C. Mitterer, "Effects of reference materials on texture coefficients determined for a CVD  $\alpha$ -Al<sub>2</sub>O<sub>3</sub> coating," *Surface and Coatings Technology*, vol. 359, pp. 314–322, Feb. 2019, doi: 10.1016/j.surfcoat.2018.12.095.
- [63] "Back-to-Basics tutorial: X-ray diffraction of thin films | Journal of Electroceramics." Accessed: Oct. 11, 2024.
- [64] M. Huff, "Review Paper: Residual Stresses in Deposited Thin-Film Material Layers for Micro- and Nano-Systems Manufacturing," *Micromachines*, vol. 13, no. 12, p. 2084, Nov. 2022, doi: 10.3390/mi13122084.
- [65] T.-A. Truong *et al.*, "Engineering Stress in Thin Films: An Innovative Pathway Toward 3D Micro and Nanosystems," *Small*, vol. 18, no. 4, p. 2105748, 2022, doi: 10.1002/sml.202105748.
- [66] T. Wu, A. Bur, J. L. Hockel, K. Wong, T.-K. Chung, and G. P. Carman, "Electrical and Mechanical Manipulation of Ferromagnetic Properties in Polycrystalline Nickel Thin Film," *IEEE Magnetics Letters*, vol. 2, pp. 6000104–6000104, 2011, doi: 10.1109/LMAG.2010.2100810.
- [67] S. A. Mathews and J. Prestigiacomo, "Controlling magnetic anisotropy in nickel films on LiNbO<sub>3</sub>," *Journal of Magnetism and Magnetic Materials*, vol. 566, p. 170314, Jan. 2023, doi: 10.1016/j.jmmm.2022.170314.

- [68] S. Finizio *et al.*, “Magnetic Anisotropy Engineering in Thin Film Ni Nanostructures by Magnetoelastic Coupling,” *Phys. Rev. Appl.*, vol. 1, no. 2, p. 021001, Mar. 2014, doi: 10.1103/PhysRevApplied.1.021001.
- [69] R. Adhikari, A. Sarkar, and A. K. Das, “A versatile cantilever beam magnetometer for *ex situ* characterization of magnetic materials,” *Review of Scientific Instruments*, vol. 83, no. 1, p. 013903, Jan. 2012, doi: 10.1063/1.3680108.
- [70] W. Jahjah *et al.*, “Thickness dependence of magnetization reversal and magnetostriction in Fe<sub>81</sub>Ga<sub>19</sub> thin films,” *Phys. Rev. Appl.*, vol. 12, no. 2, p. 024020, Aug. 2019, doi: 10.1103/PhysRevApplied.12.024020.
- [71] O. Saha, E. Andersen, and S. Roundy, “A self-biased magnetolectric wireless power transfer receiver targeting biomedical implants,” *Sensors and Actuators A: Physical*, vol. 360, p. 114558, Oct. 2023, doi: 10.1016/j.sna.2023.114558.
- [72] G. Liu, C. Zhang, and S. Dong, “Magnetolectric effect in magnetostrictive/piezoelectric laminated composite operating in shear-shear mode,” *Journal of Applied Physics*, vol. 116, no. 7, p. 074104, Aug. 2014, doi: 10.1063/1.4892988.
- [73] F. Yang, Y. M. Wen, P. Li, M. Zheng, and L. X. Bian, “Resonant magnetolectric response of magnetostrictive/piezoelectric laminate composite in consideration of losses,” *Sensors and Actuators A: Physical*, vol. 141, no. 1, pp. 129–135, Jan. 2008, doi: 10.1016/j.sna.2007.08.004.
- [74] M. I. Bichurin *et al.*, “Self-Biased Bidomain LiNbO<sub>3</sub>/Ni/Metglas Magnetolectric Current Sensor,” *Sensors*, vol. 20, no. 24, p. 7142, Dec. 2020, doi: 10.3390/s20247142.
- [75] D. A. Pan, S. G. Zhang, A. A. Volinsky, and L. J. Qiao, “Electro-deposition current density effect on Ni/PZT layered magnetolectric composites performance,” *J. Phys. D: Appl. Phys.*, vol. 41, no. 19, p. 195004, Oct. 2008, doi: 10.1088/0022-3727/41/19/195004.
- [76] S. Jen and R. Bobkowski, “Black lithium niobate SAW device fabrication and performance evaluation,” in *2000 IEEE Ultrasonics Symposium. Proceedings. An International Symposium (Cat. No. 00CH37121)*, IEEE, 2000, pp. 269–273. Accessed: May 07, 2024. [Online]. Available: <https://ieeexplore.ieee.org/abstract/document/922554/>
- [77] A. Hrennikoff, “Solution of problems of elasticity by the framework method,” 1941, Accessed: May 07, 2024.
- [78] G. Nader, E. C. N. Silva, and J. C. Adamowski, “Effective Damping Value of Piezoelectric Transducer Determined by Experimental Techniques and Numerical Analysis”.
- [79] R. Szewczyk, “Modelling of the magnetic and magnetostrictive properties of high permeability Mn-Zn ferrites,” *Pramana - J Phys*, vol. 67, no. 6, pp. 1165–1171, Dec. 2006, doi: 10.1007/s12043-006-0031-z.
- [80] M. J. Dapino, R. C. Smith, L. E. Faidley, and A. B. Flatau, “A Coupled Structural-Magnetic Strain and Stress Model for Magnetostrictive Transducers,” *Journal of Intelligent Material Systems and Structures*, vol. 11, no. 2, pp. 135–152, Feb. 2000, doi: 10.1106/MJ6A-FBP9-9M61-0E1F.
- [81] X. Zhang, Z. Tang, F. Lv, and X. Pan, “Excitation of axisymmetric and non-axisymmetric guided waves in elastic hollow cylinders by magnetostrictive transducers,” *J. Zhejiang Univ. Sci. A*, vol. 17, no. 3, pp. 215–229, Feb. 2016, doi: 10.1631/jzus.A1500184.
- [82] J. B. Restorff, M. Wun-Fogle, and A. E. Clark, “Measurement of d<sub>15</sub> in Fe<sub>100-x</sub>Ga<sub>x</sub> (x=12.5,15,18.4,22), Fe<sub>50</sub>Co<sub>50</sub>, and Fe<sub>81</sub>Al<sub>19</sub> highly textured polycrystalline rods,” *Journal of Applied Physics*, vol. 103, no. 7, p. 07B305, Apr. 2008, doi: 10.1063/1.2832667.
- [83] Y. Hsiao, D. B. Gopman, K. Mohanchandra, P. Shirazi, and C. S. Lynch, “Effect of interfacial and edge roughness on magnetolectric control of Co/Ni microdisks on PMN-PT(011),” *Sci Rep*, vol. 12, no. 1, p. 3919, Mar. 2022, doi: 10.1038/s41598-022-06285-6.

- [84] J.-Y. Duquesne, C. Hepburn, P. Rovillain, and M. Marangolo, “Magneto-crystalline and magnetoelastic constants determined by magnetization dynamics under static strain,” *J. Phys.: Condens. Matter*, vol. 30, no. 39, p. 394002, Oct. 2018, doi: 10.1088/1361-648X/aadc2f.
- [85] R. C. Kambale, D.-Y. Jeong, and J. Ryu, “Current Status of Magnetoelectric Composite Thin/Thick Films,” *Advances in Condensed Matter Physics*, vol. 2012, pp. 1–15, 2012, doi: 10.1155/2012/824643.
- [86] M. Černý, J. Pokluda, M. Šob, M. Friák, and P. Šandera, “Ab initio calculations of elastic and magnetic properties of Fe, Co, Ni, and Cr crystals under isotropic deformation,” *Phys. Rev. B*, vol. 67, no. 3, p. 035116, Jan. 2003, doi: 10.1103/PhysRevB.67.035116.
- [87] W. Yue and J. Yi-jian, “Crystal orientation dependence of piezoelectric properties in LiNbO<sub>3</sub> and LiTaO<sub>3</sub>,” *Optical Materials*, vol. 23, no. 1–2, pp. 403–408, Jul. 2003, doi: 10.1016/S0925-3467(02)00328-2.
- [88] C. Kirchhof *et al.*, “Giant magnetoelectric effect in vacuum,” *Applied Physics Letters*, vol. 102, no. 23, p. 232905, Jun. 2013, doi: 10.1063/1.4810750.
- [89] S. Marauska *et al.*, “Highly sensitive wafer-level packaged MEMS magnetic field sensor based on magnetoelectric composites,” *Sensors and Actuators A: Physical*, vol. 189, pp. 321–327, Jan. 2013, doi: 10.1016/j.sna.2012.10.015.
- [90] S. Marauska, M. Claus, T. Lisec, and B. Wagner, “Low temperature transient liquid phase bonding of Au/Sn and Cu/Sn electroplated material systems for MEMS wafer-level packaging,” *Microsyst Technol*, vol. 19, no. 8, pp. 1119–1130, Aug. 2013, doi: 10.1007/s00542-012-1708-5.